Effect of event-by-event reconstruction and low event statistics on the sensitivity of neutrino oscillation parameters at INO-ICAL detector

A THESIS

submitted by

KARAPARAMBIL RAJAN REBIN

for the award of the degree

of

DOCTOR OF PHILOSOPHY

DEPARTMENT OF PHYSICS
INDIAN INSTITUTE OF TECHNOLOGY MADRAS

September 2019

THESIS CERTIFICATE

This is to certify that the thesis titled **Effect of event-by-event reconstruction and low event statistics on the sensitivity of neutrino oscillation parameters at INO-ICAL detector**, submitted by **Karaparambil Rajan Rebin**, to the Indian Institute of Technology, Madras, for the award of the degree of **Doctor of Philosophy**, is a bona fide record of the research work done by him under our supervision. The contents of this thesis, in full or in parts, have not been submitted to any other Institute or University for the award of any degree or diploma.

Place: Chennai
Date: September 13, 2019

Prof. Jim Libby
Research Guide
Professor
Dept. of Physics
IIT-Madras, 600 036

Dedicated to,
My parents

ACKNOWLEDGEMENTS

It is with immense pleasure and gratitude that I thank my supervisor, Prof. Jim Libby, for his excellent guidance and motivation throughout the course of my work. It is his encouragement and support that kept me interested in my research work and helped me to finish my thesis. Working with him was really an encouraging experience for me to pursue my career as a researcher.

My heartfelt thanks to Prof. D. Indumathi, IMSC Chennai, for her invaluable guidance and research inputs that was instrumental in completing the research work. I am very grateful for the time and the patience she took to discuss the research work.

I thank my doctoral committee members, Prof. Suresh Govindarajan, Prof. Sunethra Ramanan and Prof. L. Sriramkumar for their insightful comments and timely advice. It is a pleasure having a supportive committee overseeing my work. I express my special thanks to Prof. Gobinda Majumdar, EHEP, TIFR for providing us the ICAL detector simulation package and also teaching its basics.

I am also very grateful for the excellent computing facilities and support from the P.G. Senapathy centre for computing resource at IITM, Chennai and the computing facility at TIFR, Mumbai, which made the intensive computation required for this analysis possible.

This long journey would have been tedious without my friends, and the fruitful discussions I had with them. I owe my gratitude to the present and past colleagues at IIT Madras, Dr. Jafar Sadiq. E, Dr. Prasanth Krishnan, Dr. Lakshmi S. Mo-

han, Abdul Basith, Aleena Chacko, Krishnakumar Raveendran, Resmi P.K, Niharika Rout and Anita Lavania. I would also like to thank all my teachers, relatives, and well wishers who have encouraged me and my desire to learn.

Last but not the least, I am very grateful to my parents, Mr. K.R. Rajan, and, Ms. Baby Rajan, for being an inspiration and teaching me the values of life. Its your selfless encouragement that keeps me going, and helps me to pursue my dreams. My sister Rissa, has been a friend and a motivator along with my parents. I thank all of them for their continued support and caring.

ABSTRACT

The proposed iron calorimeter detector (ICAL) at India-based Neutrino Observatory (INO), aims to precisely measure the atmospheric oscillation parameters $\sin^2\theta_{23}$ and Δm^2_{32}, and determine the mass-hierarchy (MH) of the neutrinos. We present the reach of the proposed INO-ICAL in measuring these atmospheric-neutrino-oscillation parameters using full event-by-event reconstruction for the first time. We find that the precision of the parameters deteriorates after the realistic consideration of event-by-event reconstruction.

Low event statistics is a common feature among neutrino experiments. Hence, for the first time in INO we study the fluctuations arising from low event statistics and their effect on the parameter sensitivities and mass-hierarchy analysis for a 5-year exposure of the 50 kton ICAL detector. We find a reasonable agreement between the unfluctuated and the average fluctuated precision reach obtained in $\sin^2\theta_{23} - \Delta m^2_{32}$ plane. We also find a mean resolution of $\Delta\chi^2 \sim 2.9$, which rules out the wrong mass hierarchy with a significance of 1.7σ. A 15% probability of identifying wrong MH is also observed as a result of fluctuations in the data.

We apply few event selection criteria to improve the reconstructed sample of muons, but discovered that all reconstructed muon events must be included to get maximum constraints on the oscillation parameters. We also find an improvement in the precision measurements with the addition of hadron information.

CONTENTS

LIST OF TABLES

LIST OF FIGURES

ABBREVIATIONS

INO	India-based Neutrino Observatory
ICAL	Iron Calorimeter
RPC	Resistive Plate Chambers
SM	Standard Model
MH	Mass hierarchy
CC	Charge Current
NC	Neutral Current
PDF	Probability Distribution Function
WS	With Event Selection
WOS	Without Event Selection
WF	With Fluctuations
WOF	Without Fluctuations
WH	With Hadrons
WOH	Without Hadrons
FC	Fully Contained
PC	Partially Contained
CR	Central Region
SR	Side Region
PR	Peripheral Region

CHAPTER 1

Neutrino physics

The Standard Model (SM) a SU(3) × SU(2) × U(1) gauge invariant quantum field theory of elementary particle physics, almost completely describes the behaviour of all known particles and three of the fundamental forces of nature. After the Higgs boson discovery at CERN [1, 2], the SM fully acquired the status of the theory of the elementary particles up to the electroweak energy scale of approximately 300 GeV. The quest for a fundamental theory that can explain all the phenomenon in our universe had led us to the SM, but it is far from complete. For example, the gravitational force, the weakest among all the forces, is excluded and the SM accounts for less than 5% of the mass-energy density in the universe, the rest is dark matter (26%) and dark energy (69%) [3]. Most pertinent to this thesis is that neutrinos are considered massless fermions in the SM, but observations of neutrino oscillations [4–12] have proved that they are massive. The implications of neutrinos being massive, has opened a new window into the physics beyond the Standard Model. Furthermore, there have also been hints of one or more sterile neutrinos that mix with active flavor neutrinos [13–16]. Sterile neutrinos, an extension of the SM, could explain the generation of neutrino masses and mixing, as well as throw light on the observed matter-antimatter asymmetry of the Universe via the leptogenesis mechanism [17, 18]. Sterile neutrinos also present themselves as a perfect candidate for the dark matter searches [19]. Therefore, understanding the neutrinos is key to a better understanding of our universe.

The current chapter presents a brief overview of neutrinos, its source and properties. A detailed description on the neutrino oscillations, and the current status on the oscillation parameters from different experiments around the globe are discussed in the subsequent sections.

1.1 A brief history of neutrinos

In the SM, neutrinos are massless fermions (spin 1/2 particles) that interact only via the weak interaction through the exchange of $W^{\pm}$ or Z^0 bosons. The neutrino was postulated by W. Pauli in 1930 as a neutral massive (of the order of electron mass) particle with spin 1/2 to explain the observed continuous energy spectrum of electrons in the β decay [20]. Subsequently the discovery of the neutron by J. Chadwick [21] enabled E. Fermi to build the first theory of β decay in 1934 [22]. The first method of neutrino detection was proposed by B. Pontecorvo using the radiochemical method [23]. Later in a pioneering reactor neutrino experiment[1] (1953-59) led by F. Reines and C.L. Cowan [24] confirmed the existence of neutrinos.

In 1956 Lee and Yang [25] postulated parity violation in weak interaction and proposed it as a solution to $\theta - \tau$ problem.[2] The first experiments in which a large parity violation in the weak processes was observed were performed by Wu *et al.* [26] in the β decay of ^{60}Co,[3] and Lederman *et al.* [27] in the decay chain of pions (1957). This led to the theory of the two component neutrino [20], which assumed the neutrino to be a massless particle, and predicted the neutrino fields to be either left-handed (helicity -1) or right-handed (helicity $+1$), and *vice-versa* for the antineutrino fields. The experiment by Goldhaber *et al.* [28] measured a negative helicity for the neutrino[4] and confirmed the two neutrino-theory in 1958. Later the structure of weak interaction ($V - A$ type interaction) was generalized from the two neutrino theory by Feynman and Gell-Mann [29] and Sudarshan and Marshak [30].

[1] Antineutrinos from the reactor were detected by observing the process $\bar{\nu} + p \rightarrow e^+ + n$, where the two photons with opposite momentum emitted from $e^+ - e^-$ anhilation are detected in coincidence with a delayed γ-rays from the neutron capture by cadmium.

[2] Two strange particles θ and τ (now known as K^+) have the same mass, charge, decay lifetime and spin (zero) - except that θ decays to two pions ($\theta^+ \rightarrow \pi^+\pi^0$) and τ decays to three pions ($\tau^+ \rightarrow \pi^+\pi^-\pi^+$), states with opposite parity.

[3] Observed an asymmetry in the angular distribution of the electrons coming from the β decay of polarized ^{60}Co nuclei to confirm parity violation.

[4] Helicity of the neutrino was obtained from the measurement of circular polarisation of the γ rays produced in the reaction chain: $e^- + {}^{152}\text{Eu} \rightarrow \nu + {}^{152}\text{Sm}^*$ ($^{152}\text{Sm} + \gamma$). Neutrinos (antineutrinos) were observed to be left-handed (right-handed) with negative (positve) helicity.

The second flavour of neutrino, ν_μ, was discovered by G. Danby *et al.* [31] at Brookhaven neutrino experiment in 1962 and confirmed the existence of the second generation of leptons (ν_μ, μ^-). In the late 1960s, S. Weinberg [32], A. Salam [33], and S. Glashow [34] proposed a SU(2) × U(1) gauge theory which unified the weak and electromagnetic interaction into one electroweak interaction. The electroweak theory predicted the existence of a scalar Higgs (H) boson and massive vector $W^\pm$ and Z^0 bosons, which take part in charged current (CC) and neutral current (NC) interactions, respectively. The discovery of the third charged lepton $\tau^\pm$ at the SPEAR e^+e^- collider at Stanford [35] was incorporated into the electroweak theory along with the τ neutrino (ν_τ) and the third generation of quarks (top and bottom). The first confirmation of the electroweak theory was with the discovery of NC interations at CERN [36] in 1973. The direct observation of intermediate vector bosons $W^\pm$ [37] and Z^0 [38] at the CERN $p\bar{p}$ collider experiment in 1983 and the precise measurements of the decay width of Z^0 at e^+e^- colliders, LEP at CERN and SLC at SLAC [39–42] (1989-92), established that the number of different active neutrinos with mass less than 45 GeV, half the mass of the Z^0, is 2.984 ± 0.008.[5] Finally the third type of neutrino ν_τ was observed by the DONUT collaboration at the Fermilab [43] in 2000, completing the third family of particles.

The electroweak theory of the SM assumes neutrinos to be massless and was successful in explaining the neutrino properties, but recent experiments on neutrino oscillations [4–7, 9–12, 44] have proved that the neutrinos are massive. The SM can be extended to include massive Dirac neutrinos, and as a consequence there must be a right-handed neutrino state, the sterile neutrino, which does not interact with known SM matter. Anomalies observed in few of the neutrino oscillation experiments, LSND and MiniBooNE [13–15], hints the presence of one or more sterile neutrinos,[6] but so far there is no significant evidence. The other possibility is that the neutrinos are Majorana particle [46,47], where the neutrinos and antineutrinos are identical.[7] In beyond the SM theories, Majorana neutrinos can explain the smallness of their mass via the see-saw mechanism, as well as

[5] The Planck result for the effective number of light neutrino families, $N_{\rm eff} = 3.15 \pm 0.23$ [3], also agrees well with the electroweak theory of the SM

[6] LSND result was excluded by 90% CL in a global analysis performed by MINOS, Daya Bay and Bugey-3 [45], but one of the MiniBooNE mode is still allowed.

[7] This would imply the violation of lepton number.

explain the baryon asymmetry seen in the universe.

The neutrino masses are extremely small in comparison to other elementary particles, and measuring it is crucial for both particle physics and cosmology. Cosmological observation gives the current best limit on the effective neutrino mass, *i.e.* the sum of neutrino masses $\Sigma_i m_{\nu_i} < 0.12$ eV (95% C.L.) [48]. The search for the Majorana neutrinos in the neutrinoless-double β decay have the effective neutrino mass[8] limit around $m_{\beta\beta} = 0.12-0.25$ eV [50]. The least model-dependent mass measurement is in β-decay experiments, which results in an effective mass[9] limit $m^2_{\nu_e} < 2$ eV^2 [51]. Experiments on neutrino oscillations have given stringent limits on the mass-square differences, as oscillations are only sensitive to mass-square difference, but it also can measure the hierarchy of neutrino masses (see Sec.1.3).

1.2 Neutrino interactions with matter

Neutrinos interact only through the weak CC and NC interactions via the exchange of massive $W^{\pm}$ and Z^0 vector bosons. Figure 1.1 shows the NC and CC vertex, where the neutrino flavor ν_α, $\alpha = e, \mu, \tau$, exchanges neutral Z^0 and charged $W^{\pm}$ bosons respectively. The CC exchange by the neutrino produce its charged lepton counterpart, while there is no final state charged lepton in NC exchange.

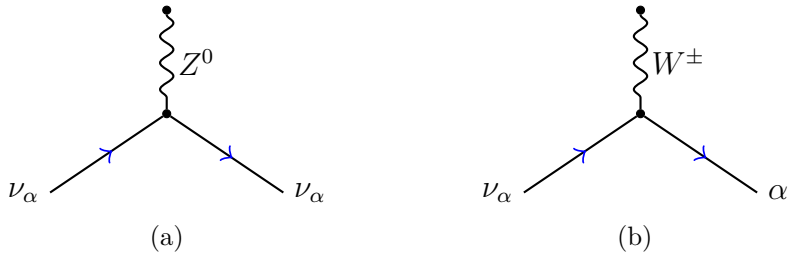

Figure 1.1: Feynman diagrams for the neutrino (a) neutral current (NC) vertex and (b) charge current (CC) vertex. Here $\alpha = e, \mu,$ or τ.

The neutrinos go through various NC and CC interactions across the differing energy scales. As the neutrinos interact very weakly with the matter, its interac-

[8] In double β-decay, the effective mass is a linear combination of neutrino mass states given by $m_{\beta\beta} = |\Sigma_i U^2_{ei} m_{\nu_i}|$, where U_{ei} are the elements of the PMNS mixing matrix [49].

[9] The effective electron neutrino mass in single beta decay is taken as $m^2_{\nu_e} = \Sigma_i |U_{ei}|^2 m^2_{\nu_i}$

tion cross-section is very small,[10] and is proportional to the neutrino energy. The various processes mediated by the neutrinos and their respective energy thresholds are as follows [53]:

(i) Threshold-less and low energy process:

The neutrinos with very low energy, *i.e.* $E_\nu \sim 0 - 1$ MeV, undergo the threshold-less process, which includes coherent scattering and neutrino capture.

(a) **Coherent scattering:** The neutrino interacts coherently with the nucleus (A_N^Z) via NC exchange.[11]

$$\nu_\alpha + \mathrm{A}_N^Z \to \nu_\alpha + \mathrm{A}_N^{*Z}. \tag{1.1}$$

(b) **Neutrino capture:** The nucleus captures the electron neutrino because it is energetically favourable,[12]

$$\nu_e + \mathrm{A}_N^Z \to e^- + \mathrm{A}_{N-1}^{Z+1}. \tag{1.2}$$

Also, Inverse β-decay ($\bar{\nu}_e + p \to e^+ + n$) with energy thresholds between $E_\nu \sim 1 - 10$ MeV and threshold-less neutrino-electron elastic scattering process ($\nu_\alpha + e^- \to \nu_\alpha + e^-$) mediated by NC and CC exchange are few of the low energy process undergone by the neutrino.

(ii) Intermediate and high energy processes:

Neutrinos with higher energy probe the target nucleus at smaller length scales. Their interactions in the energy range $E_\nu \sim 0.1 - 500$ GeV can mainly be classified in to elastic and quasi-elastic (QE) scattering, resonance production (RES) and deep inelastic scattering (DIS).

(a) **Elastic and quasi-elastic scattering:** Neutrinos with energy $E_\nu \lesssim 2$ GeV, scatter off a nucleon via CC and NC exchange liberating a nucleon (or multiple nucleons). The quasi-elastic scattering is mediated by the CC exchange, where the interactions are given by,

$$\text{CC} \qquad \nu_\alpha n \to \alpha^- p, \qquad \bar{\nu}_\alpha p \to \alpha^+ n. \tag{1.3}$$

[10] Roughly of the order of 10^{-49} m^2 to 10^{-42} m^2 [52].

[11] Threshold-less coherent scattering are yet to be detected by the experiments, and are proposed as a possible mechanism to detect relic neutrinos from the early universe.

[12] Neutrino capture is similar to the β-decay, except that it interacts with the nucleus.

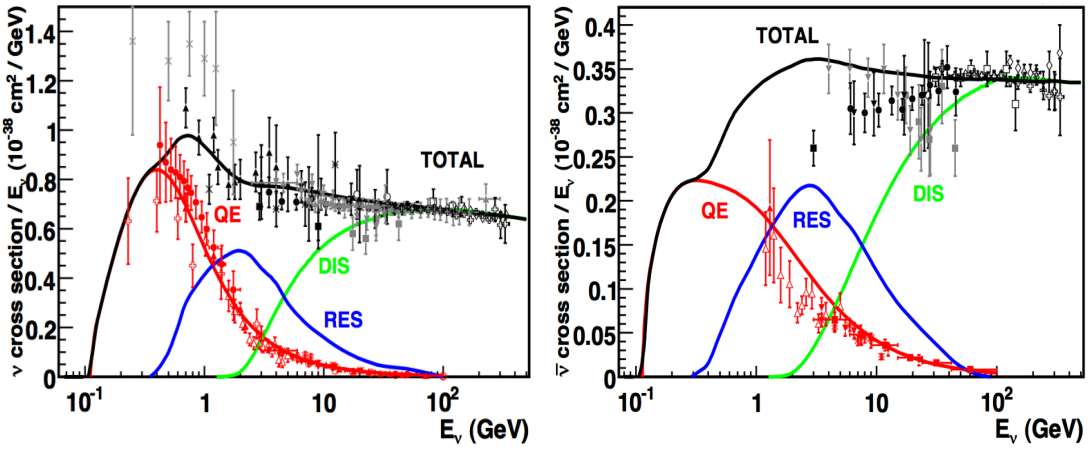

(a) (b)

Figure 1.2: Total CC cross-section per nucleon per neutrino energy as a function of neutrino energy for (a) neutrinos and (b) antineutrinos [53]. The comparison of theoretical and experimental values are also shown.

The elastic scattering is mediated by NC exchange, where the interactions are:

$$\text{NC}\left\{\begin{array}{ll} \nu_\alpha n \to \nu_\alpha n, & \nu_\alpha p \to \nu_\alpha p \\ \bar{\nu}_\alpha n \to \bar{\nu}_\alpha n, & \bar{\nu}_\alpha p \to \bar{\nu}_\alpha p. \end{array}\right. \tag{1.4}$$

The other high energy CC QE process include inverse muon decay, where muon neutrinos with energy above the muon production threshold (~ 11 GeV[13]) can interact with electrons to produce a muon:

$$\nu_\mu + e^- \to \nu_e + \mu^-. \tag{1.5}$$

The cross-section for this particular process is very low compared to other QE process.

(b) **Resonance production:** In an inelastic neutrino and baryon (N) interaction via CC (NC) exchange, mesons are produced from the decay of the baryon resonances (N^*), *i.e.* $\nu_\alpha + N \to \alpha^-(\nu_\alpha) + N^*$ and $N^* \to \pi + N'$. This resonant single pion production is dominant in the neutrino energy range $E_\nu \sim 1 - 2$ GeV. The possible CC (three processes) and NC (four processes) RES reactions are given by,

$$\text{CC}\left\{\begin{array}{ll} \nu_\alpha p \to \alpha^- p\pi^+, & \bar{\nu}_\alpha p \to \alpha^+ p\pi^-, \\ \nu_\alpha n \to \alpha^- p\pi^0, & \bar{\nu}_\alpha p \to \alpha^+ n\pi^0, \\ \nu_\alpha n \to \alpha^- n\pi^+, & \bar{\nu}_\alpha n \to \alpha^+ n\pi^-. \end{array}\right. \tag{1.6}$$

$$\text{NC}\left\{\begin{array}{ll} \nu_\alpha p \to \nu_\alpha p\pi^0, & \bar{\nu}_\alpha p \to \bar{\nu}_\alpha p\pi^0, \\ \nu_\alpha p \to \nu_\alpha n\pi^+, & \bar{\nu}_\alpha n \to \bar{\nu}_\alpha n\pi^0, \\ \nu_\alpha n \to \nu_\alpha n\pi^0, & \bar{\nu}_\alpha n \to \bar{\nu}_\alpha n\pi^0, \\ \nu_\alpha n \to \nu_\alpha p\pi^-, & \bar{\nu}_\alpha n \to \bar{\nu}_\alpha p\pi^-. \end{array}\right. \tag{1.7}$$

[13]The energy threshold is very high, as the energy required $E_\nu \approx m_\mu^2/2m_e$.

Neutrino interaction	Threshold energy	Cross-section (10^{-38} cm^2)
Elastic and quasi-elastic scattering	$\lesssim 2$ GeV	0.55
Resonance production	$\sim 1-2$ GeV	1.02
Deep inelastic scattering	$\gtrsim 2$ GeV	0.05

Table 1.1: Range of threshold energy required for different neutrino interactions and the neutrino cross-section measured at 2 GeV. Refer to the Fig. 1.2 for the variation of cross-section with the neutrino energy.

The baryonic resonance can also produce multiple pions or kaons[14] in the final state as resonant production.

(c) **Deep inelastic scattering:** Neutrinos with energy $E_\nu \gtrsim 2$ GeV, scatter off quarks in the nucleon via the CC and NC interactions producing a lepton and a cascade of hadrons (X). The reaction channels are given by,

$$\begin{array}{lll} \text{CC} & \nu_\alpha N \to \alpha^- X, & \bar{\nu}_\alpha N \to \alpha^+ X, \\ \text{NC} & \nu_\alpha N \to \nu_\alpha X, & \bar{\nu}_\alpha N \to \bar{\nu}_\alpha X. \end{array} \tag{1.8}$$

The neutrino and antineutrino CC cross-sections for the intermediate and high energy processes are illustrated in the Fig. 1.2. Table 1.1 summarizes the cross section and threshold energy of different neutrino interactions.

1.3 Neutrino oscillations

In 1968 the Homestake experiment, performed by Ray Davis and collaborators [54] measured the solar neutrino flux using a radiochemical technique[15] as proposed by B. Pontecorvo [23]. The experiment measured electron neutrinos with an energy threshold of $E_\nu = 0.814$ MeV,[16] but was only able to detect 1/3 of the solar neutrino flux above this threshold predicted theoretically by John N. Bahcall and collaborators [55].[17] This measured discrepancy is explained by neutrino oscillations, where the neutrino is a superposition of all three flavors with a definite mass

[14]The kaon reactions channels have small cross-sections due to the kaon mass and as these channels are not enhanced by any dominant resonance.

[15]They measured the number of Argon (^{37}Ar) atoms produced from chlorine (^{37}Cl) via the inverse β reaction $\nu_e + {}^{37}\text{Cl} \to {}^{37}\text{Ar} + e^-$.

[16]Homestake event rate comes from high energy ^{8}B neutrinos, since the ^{8}B neutrinos from the PP chain reaction have relatively large energy than the other neutrinos produced in the chain reaction (see Fig. 1.8).

[17]This seen anomaly was called the "solar neutrino problem". There was also a deficit in atmospheric neutrino flux measured, which was referred to as the "atmospheric neutrino problem".

and has certain probability, which depends on flight distance and energy of the neutrino, to be identified as a particular flavor.

Neutrino oscillation were proposed by B. Pontecorvo [56] in 1957, where he suggested an oscillation between Majorana neutrino and antineutrino in analogy with the strangeness-oscillation of neutral kaons [57]. Later in 1962, the oscillations between different active neutrino flavors was explained by Z. Maki, M. Nakagawa and S. Sakata [49].

1.3.1 Oscillations in vacuum

The neutrino states produced with leptons in the weak interaction are called weak flavor eigenstates (ν_e, ν_μ, ν_τ). These, along with any sterile neutrinos if present (ν_{s1}, ν_{s2} *etc.*), are linear superpositions of the fundamental mass eigenstates ν_j ($j = 1, 2, 3, ...$) with definite masses (m_j) [52]

$$|\nu_\alpha\rangle = \sum_{j=1}^{n} U^*_{\alpha j} |\nu_j\rangle \,. \tag{1.9}$$

Here $n = 3 + n_s$ (n_s is the number of sterile neutrinos), $U_{\alpha i}$ are the elements of a $n \times n$ unitary matrix. The massive neutrino states $|\nu_j\rangle$ are the eigenstates of the Hamiltonian, *i.e.* $\mathscr{H} |\nu_j\rangle = E_j |\nu_j\rangle$, with energy eigenvalues $E_j = \sqrt{p^2 + m_j^2}$. The time evolution[18] of the mass eigenstates have plane wave solutions given by

$$|\nu_j(t)\rangle = e^{-iE_j t} |\nu_j\rangle \,. \tag{1.10}$$

From Eqs. (1.9) and (1.10), the time evolution of neutrino flavor state ν_α is,

$$\begin{aligned} |\nu_\alpha(t)\rangle &= \sum_j U^*_{\alpha j} e^{-iE_j t} |\nu_j\rangle \\ &= \sum_j U^*_{\alpha j} e^{-iE_j t} \sum_\gamma U_{\gamma j} |\nu_\gamma\rangle \end{aligned} \tag{1.11}$$

Hence the pure flavor state $|\nu_\alpha(t)\rangle$ at $t = 0$, becomes a superposition of different weak flavor eigenstates ($|\nu_\gamma\rangle$) as it evolves in time ($t > 0$). The transition

[18] The mass eigenstates propagate according to the time-dependent Schrodinger equation $i\frac{d}{dt} |\nu_j(t)\rangle = \mathscr{H} |\nu_j(t)\rangle$, with no potentials.

amplitude for detecting a neutrino of flavor ν_β at any time t is given by,

$$\begin{aligned} A\left(\nu_\alpha \to \nu_\beta\right) &= \langle \nu_\beta | \nu_\alpha \rangle \\ &= \sum_j U^*_{\alpha j} U_{\beta j} e^{-iE_j t} \end{aligned} \tag{1.12}$$

The transition probability is, then, given by

$$\begin{aligned} P\left(\nu_\alpha \to \nu_\beta\right) &= \left|A\left(\nu_\alpha \to \nu_\beta\right)\right|^2 \\ &= \sum_j \sum_k U^*_{\alpha j} U_{\beta j} U_{\alpha k} U^*_{\beta k} e^{-i(E_j - E_k)} \end{aligned} \tag{1.13}$$

In the ultra-relativistic case, we have

$$E_j = \sqrt{p^2 + m_j^2} \approx E + \frac{m_j^2}{2E}, \tag{1.14}$$

where $E = p$ is the energy of the neutrino as $m_i \to 0$.[19] Substituting for $t = L$ in Eq. (1.13), where L is the distance travelled by the neutrino[20]

$$P\left(\nu_\alpha \to \nu_\beta\right) = \sum_j \sum_k U^*_{\alpha j} U_{\beta j} U_{\alpha k} U^*_{\beta k} \exp\left(-i \frac{\Delta m^2_{jk} L}{2E}\right), \tag{1.15}$$

where $\Delta m^2_{jk} = m_j^2 - m_k^2$ is the mass-square difference between the mass eigen states. The phase of the transition probability is determined by the mass-square difference, whereas the amplitude is determined by the elements of the unitary matrix. Therefore oscillation experiments are only sensitive to Δm^2_{jk}, and not to m_i. The transition probability can be written in a useful form by separating the real and imaginary parts in Eq. (1.15)

$$\begin{aligned} P\left(\nu_\alpha \to \nu_\beta\right) = \delta_{\alpha\beta} &- 4 \sum_{j>k} \Re\mathfrak{e}\left[U_{\beta j} U^*_{\alpha j} U^*_{\beta k} U_{\alpha k}\right] \sin^2\left(\frac{\Delta m^2_{jk} L}{4E}\right) \\ &+ 2 \sum_{j>k} \Im\mathfrak{m}\left[U_{\beta j} U^*_{\alpha j} U^*_{\beta k} U_{\alpha k}\right] \sin\left(\frac{\Delta m^2_{jk} L}{2E}\right). \end{aligned} \tag{1.16}$$

[19] All the mass eigenstates are assumed to have equal momentum (p).

[20] Ultra relativistic neutrinos travel almost with the speed of light, also assuming $c = \hbar = 1$, $t = L$ is a reasonable approximation.

For anti-neutrinos $U_{\alpha j} \to U^*_{\alpha j}$ [58], thus we have

$$\begin{aligned} P\left(\bar{\nu}_\alpha \to \bar{\nu}_\beta\right) = \delta_{\alpha\beta} - 4\sum_{j>k} \Re\mathfrak{e}\left[U_{\beta j}U^*_{\alpha j}U^*_{\beta k}U_{\alpha k}\right] \sin^2\left(\frac{\Delta m^2_{jk}L}{4E}\right) \\ - 2\sum_{j>k} \Im\mathfrak{m}\left[U_{\beta j}U^*_{\alpha j}U^*_{\beta k}U_{\alpha k}\right] \sin\left(\frac{\Delta m^2_{jk}L}{2E}\right). \end{aligned} \tag{1.17}$$

Accounting for factors of $\hbar$ and c in Eq. (1.16),

$$\frac{\Delta m^2_{jk}L}{4E} \approx 1.27\Delta m^2_{jk}\frac{L}{E}, \tag{1.18}$$

where the units of Δm^2_{jk} is eV^2, L is km, and E is GeV. Hence the oscillations occur when the transition probabilities are non-zero, which requires non-degenerate neutrino masses and non-zero mixing as evident from Eqs. (1.16) and (1.17). The transition probabilities for the channel $\alpha = \beta$ are called survival probabilities, and the quadratic terms in Eqs. (1.16) and (1.17) will have a real form without any imaginary terms. Hence the CP asymmetry, $A^{\text{CP}}_{\alpha\beta} = P\left(\nu_\alpha \to \nu_\alpha\right) - P\left(\bar{\nu}_\alpha \to \bar{\nu}_\alpha\right)$, can be measured only in a transition between different flavors and is given by

$$A^{\text{CP}}_{\alpha\beta} = 4\sum_{j>k} \Im\mathfrak{m}\left[U_{\beta j}U^*_{\alpha j}U^*_{\beta k}U_{\alpha k}\right] \sin\left(\frac{\Delta m^2_{jk}L}{2E}\right). \tag{1.19}$$

Two-flavor vacuum oscillations

In the case of two flavor neutrino oscillations, the mixing is governed by a 2×2 unitary matrix U with a single effective parameter (θ).

$$U = \begin{pmatrix} \cos\theta & \sin\theta \\ -\sin\theta & \cos\theta \end{pmatrix} \tag{1.20}$$

Assuming $\nu_e \to \nu_\mu$ flavor oscillations, the transition and survival probabilities from Eq. (1.15) are given by[21]

$$\begin{aligned} P\left(\nu_e \to \nu_\mu\right) = P_{e\mu} = \sin^2 2\theta \sin^2\left(1.27\Delta m^2 \frac{L}{E}\right), \text{ and} \\ P\left(\nu_e \to \nu_e\right) = P_{ee} = 1 - P\left(\nu_e \to \nu_\mu\right) \end{aligned} \tag{1.21}$$

[21] Where the sum is over four elements with the combinations of $j \ni (1,2)$ and $k \ni (1,2)$.

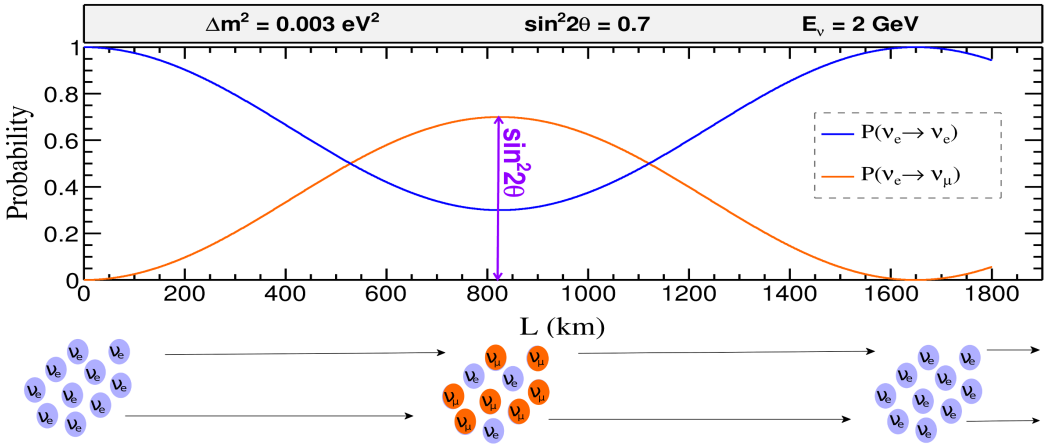

Figure 1.3: Oscillation probability as a function of distance traveled by the neutrino (L), for a given set of parameters $\Delta m^2_{21} = 0.003$ eV^2, $\sin^2 2\theta = 0.7$ and $E_\nu = 2$ GeV.

A plot of the oscillation probabilities as a function of L, is shown in Fig. 1.3, for a particular set of parameters $\Delta m^2_{21} = 0.003$ eV^2, $\sin^2 2\theta = 0.7$ and energy $E_\nu = 2$ GeV. At $L = 0$, the oscillation probability is zero and the survival probability is one. As L increases, the oscillation probability increases and reaches a maximum at $1.27\Delta m^2 L/E = \pi/2$ or $L = 824$ km. Here the amplitude of oscillation is given by the mixing angle, and $\sin^2 2\theta = 0.7$ signifies a maximum oscillation, or maximum mixing, of 70%. As L increases further, the oscillation probability reduces until around $1.27\Delta m^2 L/E = \pi$, to get the initial composition of neutrino flavor.

Note when the neutrino masses are degenerate or zero, *viz.* $\Delta m^2 = 0$, there are no oscillations. Also, large Δm^2 signifies oscillation sensitivity at short baselines (L) and *vice versa*.

Three-flavor vacuum oscillations

In case of three flavor oscillations, the three active neutrinos ν_e, ν_μ and ν_τ evolve in a more complicated, oscillatory manner, as they are linear superpositions of three, rather than two, mass eigenstates. The mixing is governed by a 3×3 unitary matrix, often refered as the Pontecorvo-Maki-Nakagawa-Sakata (PMNS)

matrix [49], and is represented by the following well-known parametrization,

$$U = \begin{pmatrix} c_{12}c_{13} & s_{12}c_{13} & s_{13}e^{-i\delta} \\ -c_{23}s_{12} - s_{23}s_{13}c_{12}e^{i\delta} & c_{23}c_{12} - s_{23}s_{13}s_{12}e^{i\delta} & s_{23}c_{13} \\ s_{23}s_{12} - c_{23}s_{13}c_{12}e^{i\delta} & -s_{23}c_{12} - c_{23}s_{13}s_{12}e^{i\delta} & c_{23}c_{13} \end{pmatrix} \begin{pmatrix} 1 & 0 & 0 \\ 0 & e^{i\frac{\alpha_{21}}{2}} & 0 \\ 0 & 0 & e^{i\frac{\alpha_{31}}{2}} \end{pmatrix}, \tag{1.22}$$

where $s_{ij} = \sin\theta_{ij}, c_{ij} = \cos\theta_{ij}$.[22] The oscillations are governed by two independent mass squared differences ($\Delta m^2_{21}, \Delta m^2_{32}$; $\Delta m^2_{ij} \equiv m^2_i - m^2_j$; $i, j = 1, 2, 3$; $i \neq j$), mixing angles ($\theta_{12}, \theta_{13}, \theta_{23}$) and one ($\delta$) or three ($\delta, \alpha_{21}, \alpha_{31}$) CP violating phases, depending on whether neutrinos are Dirac or Majorana particles [59], respectively.[23]

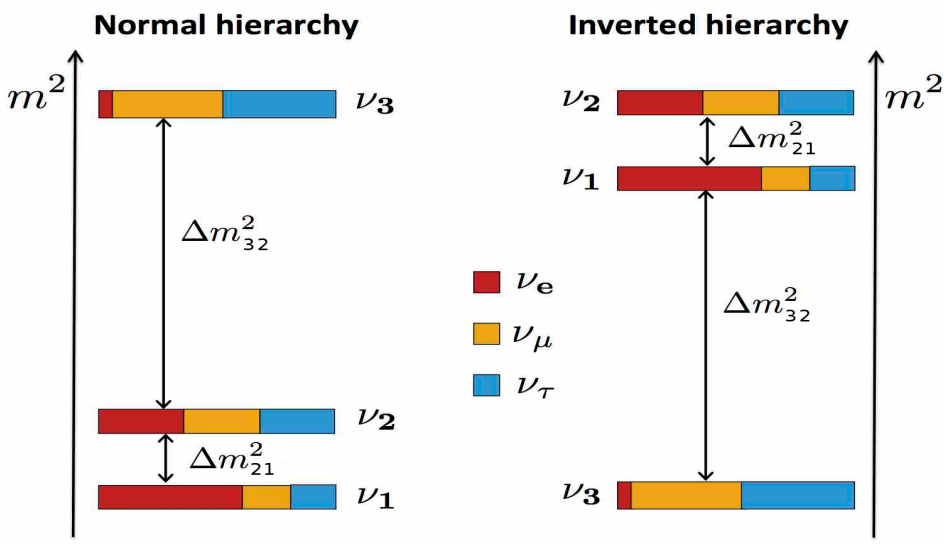

Figure 1.4: Schematic representation of the possible neutrino mass hierarchies [60], normal (NH) and inverted (IH) hierarchy.

The parameter Δm^2_{21} was found to be small and positive from solar and reactor neutrino experiments [61], but the sign of Δm^2_{32} is yet to be determined. Correspondingly, two three-neutrino mass spectra are possible: Normal Hierarchy (NH) ($m_1 < m_2 < m_3$) and Inverted Hierarchy (IH) ($m_3 < m_1 < m_2$), as illustrated in Figure 1.4. Note that the absolute mass scales are not known, but measuring the mass hierarchy will provide the information on the lightest and the heaviest of the active neutrinos.

[22] Given by the limits: angles $\theta_{ij} = [0, \pi/2]$ and $\delta = [0, 2\pi]$.

[23] A 3×3 unitary matrix has $3^2 = 9$ independent parameters, three amplitudes and six phases. The Dirac neutrino fields can be redefined to absorb five of the unitary phase to get three amplitudes ($\theta_{12}, \theta_{13}, \theta_{23}$) and one CP phase ($\delta$), while Majorana type neutrinos will have two additional phases (α_{21}, α_{31}).

Understanding the oscillations is easier under the approximation of one mass-scale dominance,[24] *i.e.* assuming $\Delta m^2_{21} = 0$; this approximation works well for reasonable energies and length scales [62]. Under this approximation, the simplified analytical expressions for three-flavor vacuum oscillations are given by

$$\begin{aligned} P_{\mu\mu} = 1 &- \sin^2\theta_{23}\sin^2 2\theta_{13}\sin^2\left(1.27\frac{\Delta m^2_{31}L}{E}\right) \\ &- \cos^4\theta_{13}\sin^2 2\theta_{23}\sin^2\left(1.27\frac{\Delta m^2_{31}L}{E}\right), \end{aligned} \tag{1.23}$$

$$P_{e\mu} = \sin^2\theta_{23}\sin^2 2\theta_{13}\sin^2\left(1.27\frac{\Delta m^2_{31}L}{E}\right). \tag{1.24}$$

As a consequence of the approximation, these expressions are independent of the phase δ, which means the neutrino vacuum oscillation probability will be equivalent to antineutrino vacuum oscillation probabilities ($P_{\alpha\beta} = \bar{P}_{\alpha\beta}$).

1.3.2 Matter effects on oscillations

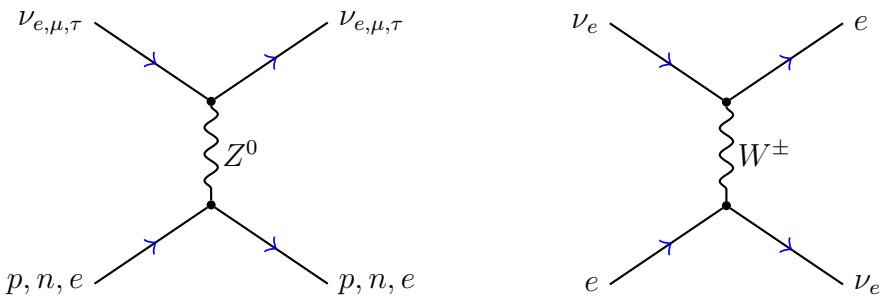

Figure 1.5: Feynman diagrams for the neutrino scattering inside the matter via (a) neutral current (NC) interaction and (b) charge current (CC) interaction.

In matter, neutrino propagation is affected by interactions; they can scatter on the electrons (e^-), protons (p) and neutrons (n) present. The incoherent elastic and the quasi-elastic scattering have a negligible effect on the neutrino propagation [51], where as coherent forward elastic scattering significantly modifies oscillation probabilities [63, 64].[25] Contributions from neutral current (NC) interactions

[24] Since $\Delta m^2_{32} \gg \Delta m^2_{21}$, the oscillations are assumed to be dominated by one mass-scale Δm^2_{32} and the value of $\Delta m^2_{21} \approx 0$. Hence $\Delta m^2_{32} = \Delta m^2_{31}$ in this approximation.

[25] In a coherent scattering, the wave function of the nucleus remains the same before and after the interaction. Hence, the charge, spin, isospin or other quantum numbers will not change, whereas, the incoherent elastic and the quasi-elastic scattering changes the states of the initial particles in the process.

of all three neutrinos flavors (ν_e, ν_μ and ν_τ) with matter particles are the same (Fig. 1.5(a)), hence they do not have any impact on neutrino oscillation probabilities. Electron neutrinos have an additional charge current (CC) interaction (Fig. 1.5(b)),[26] which results in an appearance of additional phase difference in neutrino system through matter potential given by,

$$\begin{aligned} A_{cc} &= \pm 2\sqrt{2} G_F n_e E \\ &= \pm 7.63 \times 10^{-5}\ \rho E, \end{aligned} \tag{1.25}$$

where the sign is positive for ν and negative for $\bar{\nu}$. Here, G_F is the Fermi coupling constant, E is the neutrino energy in GeV, and n_e is the electron number density, which is related to the matter density ρ in gcm^{-3}. The time evolution of the flavor eigenstates in the presence of a matter potential is given by the expression:

$$i\frac{d}{dt}\left[\nu_\alpha\right] = \frac{1}{2E}\left(UM^2U^\dagger + \mathcal{A}\right)\left[\nu_\alpha\right], \tag{1.26}$$

where U is the PMNS mixing matrix given by the eqn (1.22) and

$$\left[\nu_\alpha\right] = \begin{pmatrix} |\nu_e\rangle \\ |\nu_\mu\rangle \\ |\nu_\tau\rangle \end{pmatrix}, M^2 = \begin{pmatrix} 0 & 0 & 0 \\ 0 & \Delta m^2_{21} & 0 \\ 0 & 0 & \Delta m^2_{31} \end{pmatrix}, \mathcal{A} = \begin{pmatrix} A_{cc} & 0 & 0 \\ 0 & 0 & 0 \\ 0 & 0 & 0 \end{pmatrix} \tag{1.27}$$

The resultant Hamiltonian, *i.e.* $\mathscr{H} = \frac{1}{2E}\left(UM^2U^\dagger + \mathcal{A}\right)$, in the flavor basis can be transformed into the mass basis and diagonalized[27] to obtain the correct mass eigenstates in matter, which can then be mapped to the vacuum eigenstates. Therefore, assuming one-mass scale dominant approximation and within the framework of constant density, the effective oscillation parameters $\left[\Delta m^2_{31}\right]^m$ and $\sin 2\theta^m_{13}$ in matter[28] can be expressed as [62]:

$$\left[\Delta m^2_{31}\right]^m = \sqrt{\left(\Delta m^2_{31}\cos 2\theta_{13} - A_{cc}\right)^2 + \left(\Delta m^2_{31}\sin 2\theta_{13}\right)^2}, \tag{1.28}$$

$$\sin 2\theta^m_{13} = \frac{\sin 2\theta_{13}\Delta m^2_{31}}{\sqrt{\left(\Delta m^2_{31}\cos 2\theta_{13} - A_{cc}\right)^2 + \left(\Delta m^2_{31}\sin 2\theta_{13}\right)^2}}. \tag{1.29}$$

[26] As the ordinary matter only contains electrons, protons and neutrons, and are devoid of muons and tau leptons. Only the electron neutrinos can take part in CC scattering.

[27] The Hamiltonian will no longer be diagonal in the mass basis after rotation from the flavor basis, hence the mass eigenstates in a vacuum are not the eigenstates of the Hamiltonian in matter. Therefore the resultant Hamiltonian is diagonalized.

[28] Here, the oscillation parameters with superscript “m" are those prone to matter effects.

Correspondingly the oscillation probabilities in Eqs. (1.23) and (1.24) are modified as follows:

$$\begin{aligned} P^m_{\mu\mu} = 1 &- \sin^2 2\theta_{23} \cos^2 \theta^m_{13} \sin^2 \left(1.27 \frac{\left(\Delta m^2_{31} + A_{cc} + [\Delta m^2_{31}]^m \right) L}{2E} \right) \\ &- \sin^4 \theta_{23} \sin^2 2\theta^m_{13} \sin^2 \left(1.27 \frac{[\Delta m^2_{31}]^m L}{E} \right) \\ &- \sin^2 2\theta_{23} \sin^2 \theta^m_{13} \sin^2 \left(1.27 \frac{\left(\Delta m^2_{31} + A_{cc} - [\Delta m^2_{31}]^m \right) L}{2E} \right), \quad \text{and} \end{aligned} \tag{1.30}$$

$$P^m_{e\mu} = \sin^2 \theta_{23} \sin^2 \theta^m_{13} \sin^2 \left(1.27 \frac{[\Delta m^2_{31}]^m L}{E} \right). \tag{1.31}$$

For the analysis presented in this thesis, the matter effects are applied by numerically evolving the full three flavor neutrino propagation, as described in Eq. (1.26), using the method reported in Ref. [65], which assumes the Preliminary Reference Earth Model (PREM) [66] density profile for the Earth.[29] The following are the consequences of matter effects:

1. The transition and survival probabilities are different in matter and vacuum.
2. The matter effects are not the same for neutrinos and antineutrinos as the value of A_{cc} is positive for a neutrino and negative for an antineutrino, which can be clearly seen from Figure 1.6, even in the absence of CP violation. The CP phase (δ) drops out for one mass scale approximation, but if present, also has the same effect on the oscillation probabilities.
3. When the value of A_{cc} is zero, the matter modified parameters reduce to the vacuum parameters as expected, *i.e.*, $[\Delta m^2_{31}]^m = \Delta m^2_{31}$ and $\sin 2\theta^m_{13} = \sin 2\theta_{13}$.
4. For very dense matter $A_{cc} \to \infty$, therefore $\sin 2\theta^m_{13} \to 0$. Hence there will be no oscillation in dense matter as the amplitude of the mixing tends to zero.
5. Resonance happens when $A_{cc} = \Delta m^2_{31} \cos 2\theta_{13}$, which implies $[\Delta m^2_{31}]^m = \Delta m^2_{31} \sin 2\theta_{13}$ and $\sin 2\theta^m_{13} = 1$. The matter mixing angle $\sin 2\theta^m_{13}$ is maximum regardless of the value of the vacuum mixing angle $\sin 2\theta_{13}$. This is called the MSW resonance [64]. The peaks (around 10^3 in L/E_ν) in ν_e oscillations in Figure 1.6(b) and 1.6(d) are due to the resonance, where the transition probability becomes maximal.

[29] However, the equations from (1.28) to (1.31) are obtained by assuming the approximation of one mass-scale dominance to understand the matter effects better, and are not used in the analysis.

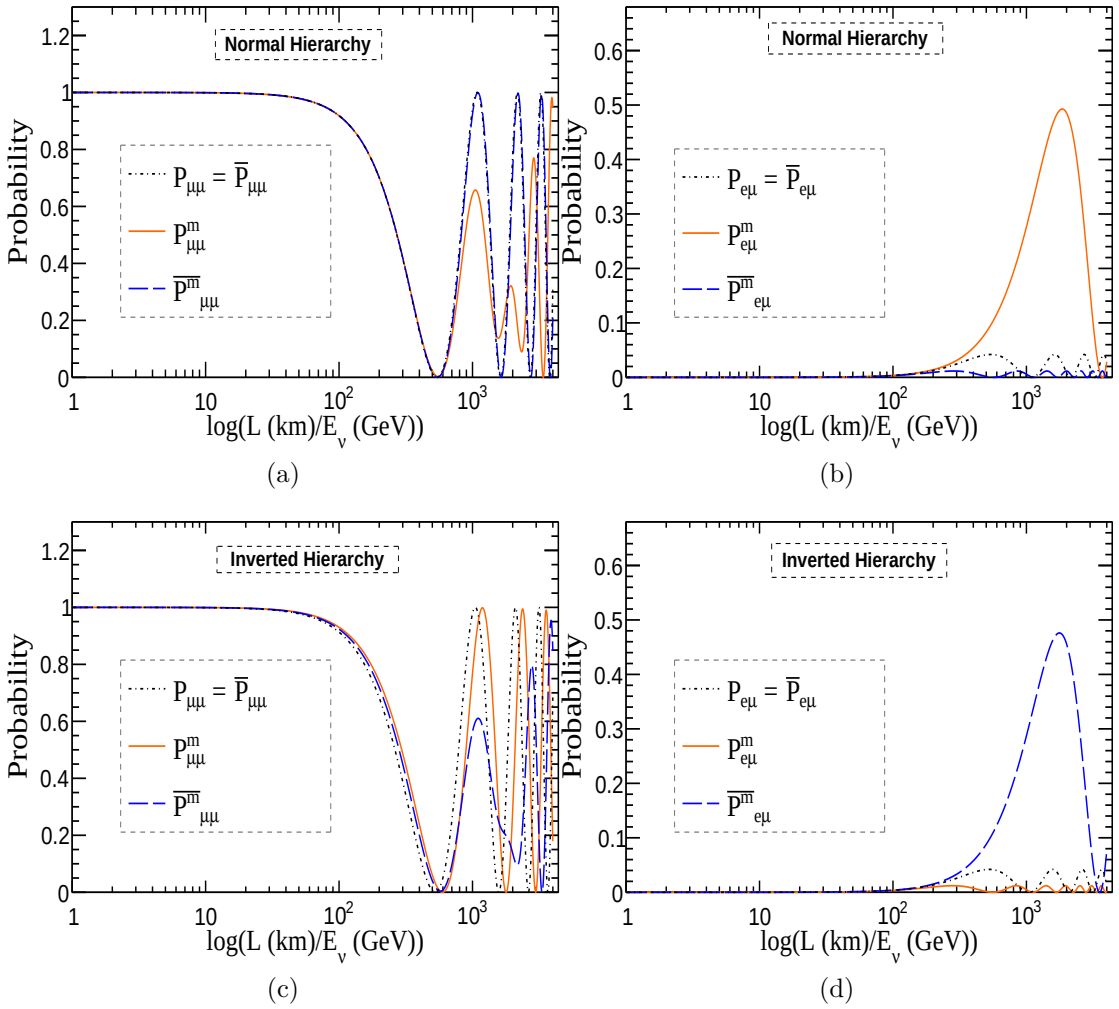

Figure 1.6: Survival and oscillation probabilities as a function of $\log(L/E_\nu)$ are shown for both neutrinos and antineutrinos assuming normal [Fig (a) and (b)] and inverted hierarchy [Fig (c) and (d)]. The probabilities are compared with and without matter effects, showing the difference in the effect of MSW resonance for neutrinos and antineutrinos for the different hierarchies. Here we choose around $E_\nu \approx 5$ GeV, where it satisfies the resonance condition for constant density $\rho = 5.51$ gcm^{-3}. The oscillation parameters are chosen to be $\theta_{13} \cong 8.6°$, $\theta_{12} \cong 33.4°$ $\theta_{23} \cong 45°$ $\Delta m^2_{31} = 0.00232$ eV^2 and $\Delta m^2_{21} = 7.5 \times 10^{-5}$ eV^2.

6. If Δm^2_{31} is positive, *i.e.* normal hierarchy, the resonance will happen in neutrino oscillations (see Figure 1.6(a) and 1.6(b)).

7. If Δm^2_{31} is negative, *i.e.* inverted hierarchy, the resonance will happen in antineutrino oscillations (see Figure 1.6(c) and 1.6(d)).

From items 6 and 7 it is clear that matter effects can distinguish normal and inverted mass hierarchy, provided the resonance is observed separately in neutrino and antineutrinos.

1.4 An overview of neutrino sources and experiments

Knowledge of the neutrino flux is of fundamental importance in designing a neutrino oscillation experiment and in performing data analysis. Most of the fluxes are modeled, and are validated using experimentally observable parameters of the model. The neutrino flux covers wide range of energy, from μeV neutrinos, which are relics from big-bang nucleosynthesis,[30] to EeV cosmogenic neutrinos.[31] Figure 1.7 shows the measured energy spectrum of the solar, supernova, geo, reactor and atmospheric neutrinos, along with the expected rate of neutrinos from cosmological, cosmogenic, supernova background and active Galactic nuclei[32] (AGN). The low energy cosmic neutrino flux is exceedingly difficult to measure directly, but its existence was confirmed by an analysis of the Planck (2013) data [69].

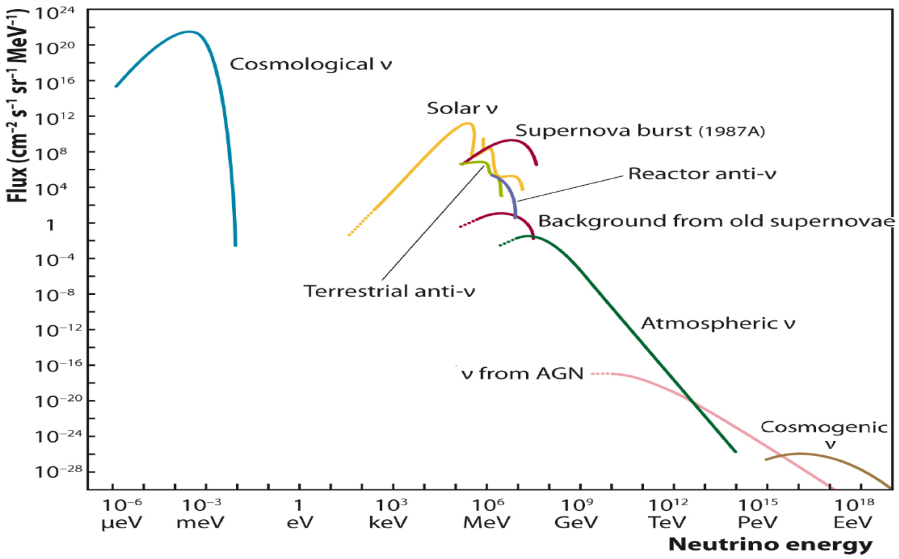

Figure 1.7: Measured and expected rate of natural and reactor neutrinos [70].

The higher end of the spectrum is modeled by neutrinos from γ-ray burst, AGN and cosmogenic origins. These high energy neutrinos are yet to be detected. The

[30] Big-bang nucleosynthesis refers to the production of nuclei in the early phase of the universe, shortly after the big-bang.

[31] Cosmogenic neutrinos are high energy neutrinos, which are produced in the interaction between high energy cosmic rays and background photons (cosmic microwave background - CMB) in the universe [67].

[32] Active galactic nuclei (AGN) are energetic astrophysical source with an actively accreting super massive black hole [68]. The cold matter (gas and dust) forming accretion disks around black holes feed them matter producing massive burst of radiation.

recent observation of PeV scale neutrinos[33] by the IceCube neutrino observatory [71] is consistent with their origin being astrophysical rather than cosmogenic at the 99% confidence level (CL). Detecting the high energy neutrinos in EeV range requires large scale detectors[34] in the future.

Many experiments have detected neutrinos emanating from the Sun [54] and a supernova burst [74–76], registering energies from few keV to few tens of MeV.[35] The atmospheric neutrino flux has the widest range of energies from a few MeV to hundreds of TeV. Atmospheric neutrinos along with reactor, accelerator and solar neutrinos are used extensively in neutrino oscillation studies. Solar and atmospheric neutrinos are among the naturally produced neutrinos used in oscillation experiments, therefore their fluxes, energy spectra, and baselines cannot be controlled. Hence a good understanding of their fluxes is of utmost importance.

1.4.1 Solar neutrinos

The sun is an abundant source of electron neutrinos with energies of the order of 1 MeV. The neutrinos are produced in the thermonuclear reactions known as *pp* (proton-proton) chain, where four protons and two electrons combine to form ^{4}He nucleus along with the emission of two neutrinos and some energy.

$$4p + 2e^- \rightarrow {}^4\text{He} + 2\nu_e + 26.731 \text{ MeV} - E_\nu. \tag{1.32}$$

Figure 1.8 shows the solar neutrino spectrum predicted by the BPS08(GS) standard solar model [77]. The *pp* reactions produce relatively large flux of neutrinos, but with low energies. Larger energies are observed for the neutrinos from ^{3}He p and ^{8}B reactions.

[33] The estimated neutrino energies were $(2.6 \pm 0.3) \times 10^6$ GeV and $(7.7 \pm 2.0) \times 10^5$ GeV.

[34] Radio Askaryan neutrino detectors like ARA [72] or ARIANNA [73] will be important in detecting them in the future.

[35] The neutrinos from supernova explosion (SN1987A) were simultaneously measured by Kamiokande II [74] and Irvine-Michigan-Brookhaven (IMB) [75] with energies 10 to 40 MeV, whereas the Mont Blanc events [76] were detected 4.5 hr before the other detectors detected them, and hence are generally assumed to be statistical fluctuations.

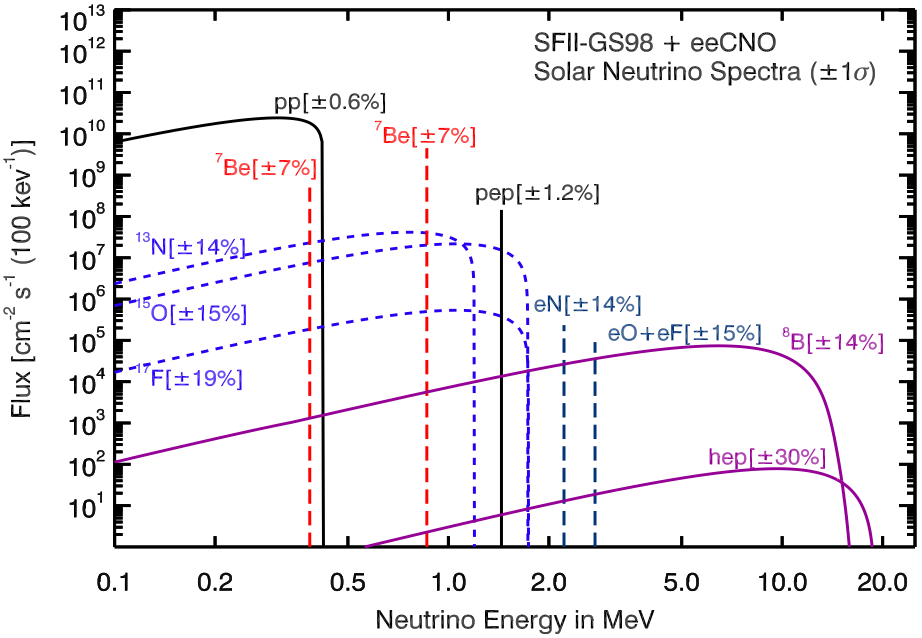

Figure 1.8: Solar neutrino spectrum predicted by the BPS08(GS) standard solar model [77].

Solar neutrino experiments

The first evidence of solar neutrinos came after the measurement of relatively energetic ^{8}B neutrinos by the Homestake experiment in 1968 [54]. The experiment observed the radio-chemical reaction in which chlorine (^{37}Cl) nuclei are converted to argon (^{37}Ar),[36] with the absorption of a neutrino,

$$\nu_e + {}^{37}\mathrm{Cl} \rightarrow {}^{37}\mathrm{Ar} + e^-, \tag{1.33}$$

which has an energy threshold of 0.814 MeV. Gallium based experiments,[37] GALLEX [78, 79] and GNO [80] at Gran Sasso (Italy) and SAGE [81] at Baksan (Russia) were primarily sensitive to neutrinos from the *pp* reaction, due to its lower energy threshold of 0.233 MeV. Borexino [82–86], a liquid scintillator detector at Gran Sasso directly observed the ^{7}Be neutrino flux for the first time [82], and was the first experiment to measure the flux of *pep* [83] solar neutrinos.

[36] The ^{37}Ar nuclei produced in the reaction are radioactive with a half-life of 34.8 days. They were chemically extracted and counted using a proportional counter.

[37] Gallium experiments utilized the reaction $\nu_e + {}^{71}\mathrm{Ga} \rightarrow {}^{71}\mathrm{Ge} + e^-$, where ^{71}Ge atoms decay through electron capture with a half-life of 11.43 days.

Decay	Branching ratio (%)
$\pi^{\pm} \to \mu^{\pm} + \nu_{\mu}(\bar{\nu}_{\mu})$	99.9877
$\pi^{\pm} \to e^{\pm} + \nu_{e}(\bar{\nu}_{e})$	0.0123
$K^{\pm} \to \mu^{\pm} + \nu_{\mu}(\bar{\nu}_{\mu})$	63.55
$K^{\pm} \to \pi^{0} + \mu^{\pm} + \nu_{\mu}(\bar{\nu}_{\mu})$	3.353
$K^{\pm} \to \pi^{0} + e^{\pm} + \nu_{e}(\bar{\nu}_{e})$	5.07
$K_{L} \to \pi^{\pm} + \mu^{\mp} + \bar{\nu}_{\mu}(\nu_{\mu})$	27.04
$K_{L} \to \pi^{\pm} + e^{\mp} + \bar{\nu}_{e}(\nu_{e})$	40.55
$\mu^{\pm} \to e^{\pm} + \bar{\nu}_{\mu}(\nu_{\mu}) + \nu_{e}(\bar{\nu}_{e})$	100

Table 1.2: Atmospheric neutrino producing decay modes of the secondary cosmic ray particles and its branching ratios [51].

Water Cherenkov detectors, Kamiokande [87,88] and Super-Kamiokande [89–92] using H_2O, and SNO [93–96] using heavy water (D_2O), measured the ^{8}B neutrino flux, which was instrumental in establishing neutrino oscillations. The Super-kamiokande experiment observed the elastic scattering (ES) of neutrinos, *i.e.* $\nu_{\alpha} + e^{-} \to \nu_{\alpha} + e^{-}$, and measured a flux less than half of that predicted by the solar standard model [90]. The measured flux $\Phi_{\rm ES}^{\rm SK} = (2.35 \pm 0.02 \pm 0.08) \times 10^{-6}$ cm^{-2}s^{-1}, was consistent with the observation made by the Homestake experiment.[38]

The SNO experiment observed CC [$\nu_e + d \to e^{-} + p + p$], NC [$\nu_{\alpha} + d \to \nu_{\alpha} + p + n$] and elastic scattering [$\nu_{\alpha} + e^{-} \to \nu_{\alpha} + e^{-}$] of the neutrinos, and measured a relative excess of NC events over the CC events [95]. Note that the NC reactions are equally sensitive to all active neutrino flavors, while CC reactions are only sensitive to ν_e. The relative flux measured is $\Phi_{\rm CC}^{\rm SNO}/\Phi_{\rm NC}^{\rm SNO} = 0.340 \pm 0.023^{+0.029}_{-0.031}$ [95], which demonstrated that about two out of three ν_e oscillate to ν_{μ} or ν_{τ}. Hence, the result solved the solar neutrino problem and proved neutrino oscillation hypothesis.

1.4.2 Atmospheric neutrinos

Atmospheric neutrinos are the decay products of the secondary cosmic ray particles produced in the interaction of a primary cosmic ray, which are predominantly

[38]Note that Super-Kamiokande experiment is sensitive to all active neutrinos ($\nu_e, \nu_{\mu}, \nu_{\tau}$), however ν_e sensitivity is larger than ν_{μ} and ν_{τ} sensitivity since $\sigma(\nu_{\mu,\tau}e) \approx 0.16\sigma(\nu_e e)$.

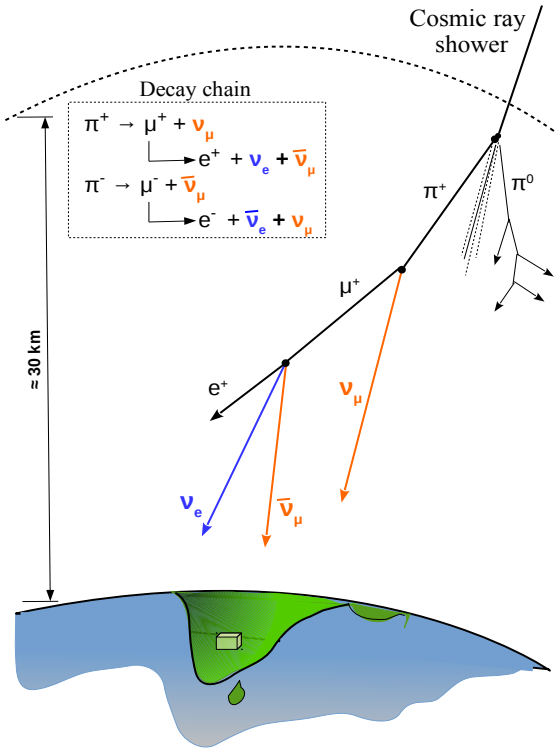

Figure 1.9: Schematic of decay modes producing atmospheric neutrinos.

protons, with the nuclei in the Earth atmosphere in interactions like

$$p + \mathrm{A}_n \rightarrow \pi^{\pm} + X \ , \tag{1.34}$$

where A_n represents the nuclei in earths atmosphere (mainly nitrogen, oxygen and carbon), and X represents a collection of other hadrons and nuclei. The primary cosmic ray particles are highly energetic particles emerging from galactic and extragalactic sources. The main components of the primary cosmic ray flux are protons (79%), alpha particles (15%), and heavy nuclei (4%) [52].

The secondary particles produced are mainly pions ($\pi^{\pm}$), but primary cosmic rays of higher energy also lead to secondary kaons ($K^{\pm}$). The decay channels of the secondary and tertiary particles with their respective branching fractions are given in the Table 1.2. Note that only the neutrino flavors $\nu_e(\bar{\nu}_e)$ and $\nu_\mu(\bar{\nu}_\mu)$ are produced in the atmosphere (see Fig. 1.9). Production of ν_τ requires the decay of heavier mesons (like $D_s \rightarrow \tau\nu_\tau$),[39] but their contribution is very small with the ν_τ flux is estimated to be about 10^{-6} times lower than ν_μ or ν_e [97].

[39]The branching fraction of $D_s \rightarrow \tau\nu_\tau$ is just 5.5% [51] and the ν_τ contribution from the decay of other heavier mesons is negligible compared to the D_s contribution [97].

The energy spectrum of the atmospheric neutrino flux follows an approximate single power function, $\propto E_\nu^{-\gamma}$, above a few GeV. The spectral index γ is estimated to be around 3.0 and 3.5 for ν_μ and ν_e respectively.[40] Figure 1.10(a) shows the energy spectrum of neutrino flavors $\nu_e(\bar{\nu}_e)$ and $\nu_\mu(\bar{\nu}_\mu)$ calculated from different models (Honda [98], Bartol [99] and Fluka [100]).

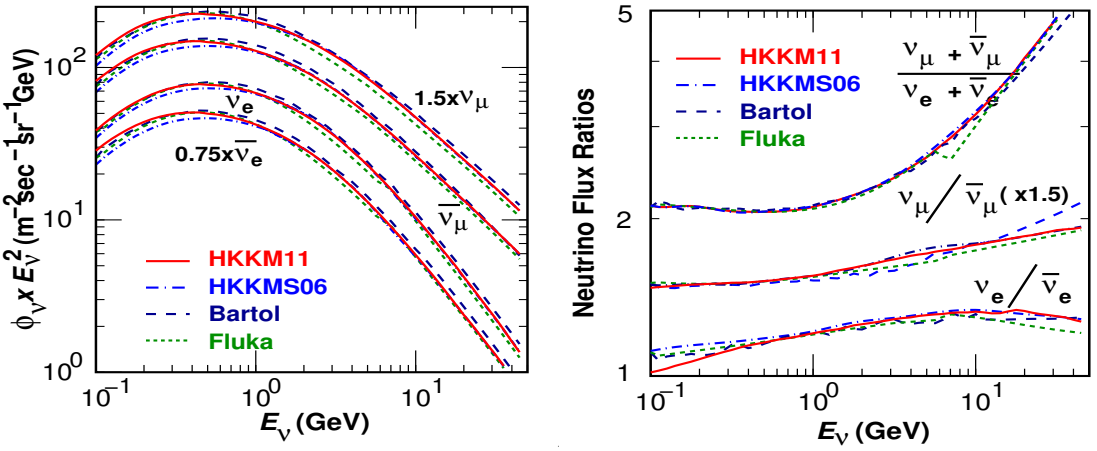

(a) (b)

Figure 1.10: Different model calculations of (a) the direction integrated fluxes and (b) flux ratios, as a function of neutrino energy for different neutrino species. The figures are reproduced from Honda et al. [98].

In the subsequent decay of secondary and tertiary particles, the flux of neutrino flavors $\Phi[\nu_\mu + \bar{\nu}_\mu]$ and $\Phi[\nu_e + \bar{\nu}_e]$ are produced approximately in a 2:1 ratio. Figure 1.10(b) shows the $\Phi[\nu_\mu + \bar{\nu}_\mu]/\Phi[\nu_e + \bar{\nu}_e]$ ratio as a function of neutrino energy E_ν. The ratio increases with the increase in energy, as the high energy tertiary muons reach the Earth without decaying in to electrons. Historically, many experiments[41] on atmospheric neutrinos have measured this ratio in search for neutrino oscillations.

The flavor ratio cannot be measured directly, as the neutrinos are not observed directly. Instead, the charged lepton counterparts produced in the CC interaction are detected. Hence the experiments measure the ratio-of-ratios,

$$R_{\mu/e} \equiv \frac{(N_\mu/N_e)_{\text{data}}}{(N_\mu/N_e)_{\text{expected}}}, \tag{1.35}$$

[40]The systematic uncertainty is estimated to be 5% , which mainly arises from the spectral index of the primary cosmic ray. The detailed systematic calculations are described later.

[41]Initially the experiments were built in search of nucleon (proton) decay where the atmospheric neutrinos were the background, but later the study of atmospheric neutrinos took the center stage.

where, N_μ and N_e are the number of μ and e candidates; any deviation of $R_{\mu/e}$ from unity is evidence of oscillations.

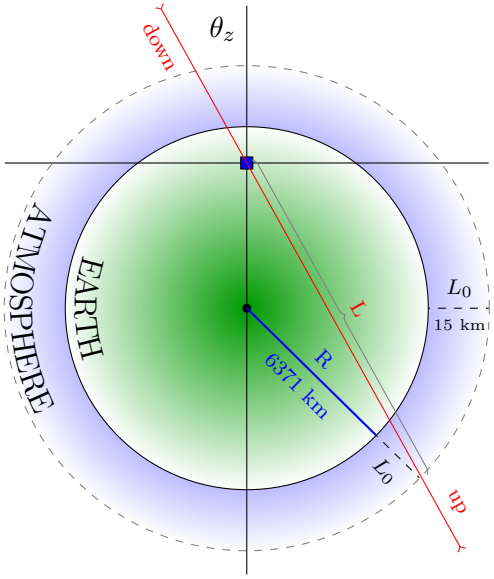

Figure 1.11: Schematic showing the direction of a neutrino (up or down going) and the L associated with the zenith angle θ_z.

The atmospheric neutrinos are a unique source in that they cover a wide range of E_ν and L. Hence they are sensitive to neutrino oscillations over a wide range of Δm^2. Figure 1.11 shows the schematic of the relationship between the direction of a neutrino (up or down going) and L associated with a particular zenith angle (θ_z).[42]

The primary cosmic rays arrive almost isotropically around the globe, hence the neutrino flux is quite symmetric about the up and down directions, *i.e.*, Φ_ν will be equal in θ_z and the $\pi - \theta_z$ directions. However at low energies, $E_\nu < 3$ GeV [101], the up-down symmetry is affected by the geomagnetic effects.[43] At higher energies the flux is essentially symmetric in zenith angle, and any asymmetry observed will be a model-independent proof of neutrino oscillations. The up-down asymmetry is usually expressed as

$$A_\alpha^{UD} = \left(\frac{U - D}{U + D}\right)_\alpha , \tag{1.36}$$

where, U and D are the up-going and the down-going neutino fluxes measured for a particular neutrino flavor α. Here any deviation of A_α^{UD} from zero signifies

[42]The distance traveled by the neutrino is given by $L = \sqrt{(R + L_0)^2 - (R \sin\theta_z)^2} \pm R\cos\theta_z$, but by convention $0 \leq \theta_z \leq \pi/2$ are up-going, and $\pi/2 < \theta_z \leq \pi$ are down-going in the analysis presented in this thesis. Hence $L = \sqrt{(R + L_0)^2 - (R \sin\theta_z)^2} + R\cos\theta_z$ is chosen.

[43]The low energy charged particle (mainly muons) gets deflected by the Lorentz force of the Earth's magnetic field and is prevented from reaching the Earth's surface.

the oscillation of neutrino flavor ν_α into other flavors. A negative value for A_α^{UD} signifies oscillation in up-going events and a positive value signifies oscillation in down-going events.

Atmospheric neutrino oscillation experiments

The first experimental observation of atmospheric neutrinos was from the deep underground laboratories at Kolar Gold Field in India [102] and East Rand Proprietary Gold Field in South Africa [103] in 1965. The first indication of atmospheric neutrino anomaly was presented by the water Čerenkov detector at Kamiokande in 1988 [104], where only $(59 \pm 7)\%$ of the predicted muon flux was detected. Later, Kamiokande also measured $R_{\mu/e}$ to be $0.60^{+0.07}_{-0.06} \pm 0.05$[44] for events with visible energy $E_{\text{vis}} < 1.33$ GeV (sub-GeV) [105] and $0.57^{+0.08}_{-0.07} \pm 0.07$ for $E_{\text{vis}} > 1.33$ GeV (multi-GeV) [106].[45] The IMB (Irvine-Michigan-Brookhaven) experiment, housing a water Čerenkov detector, measured $R_{\mu/e} = 0.54 \pm 0.05 \pm 0.11$ for $E_{\text{vis}} < 1.5$ GeV [109, 110], in agreement with the anomaly observed in Kamiokande data.

In 1998, Super-Kamiokande (SK) experiment discovered the atmospheric neutrino oscillations [111], by measuring the up-down asymmetry $A_\mu^{UD} = -0.296 \pm 0.048 \pm 0.01$ for ν_μ candidates and $A_e^{UD} = -0.036 \pm 0.067 \pm 0.02$ for ν_e candidates. The asymmetry in ν_e events was consistent with zero, while ν_μ like events observed a negative asymmetry. The up-going ν_μ travel larger distances than the down-going ν_μ, and thus having a greater probability to oscillate into another flavor giving a negative value for asymmetry. The measurements from SK favored $\nu_\mu \to \nu_\tau$ channel over the $\nu_e \leftrightarrows \nu_\mu$ channel, and gave model-independent evidence for neutrino oscillations.

Later other experiments, such as Soudan 2 [112], an underground iron tracking calorimeter, and MACRO [113], a multipurpose scintillator detector, obtained results consistent with neutrino oscillations.[46] The high energy neutrino telescopes, ANTARES [114] and IceCube-DeepCore [115], have also observed the neutrino

[44] Here, and elsewhere in this thesis, if two uncertainties are quoted the first is statistical and the second is systematic.

[45] Meanwhile the NUSEX [107] and Frejus [108] experiments did not find any indications of the atmospheric neutrino anomaly in their data.

[46] Soudan 2 and MACRO detectors are completely different from water Čerenkov detectors used by SK, Kamiokande and IMB, hence an independent confirmation.

oscillation in the atmospheric neutrinos. These results have also been confirmed in accelerator and reactor experiments that will be described in Sec. 1.4.3.

1.4.3 Reactor and accelerator neutrinos

The sensitivity of oscillation experiments depends on many factors, such as the neutrino energy and flux, the distance traveled by the neutrino (baseline), the size and efficiency of the detector, and the backgrounds involved. In the case of solar and atmospheric neutrino experiments, the neutrino energy, flux and baseline are fixed, whereas in reactor and accelerator neutrino experiments all the above mentioned factors can be varied. Hence they can probe the oscillation sensitivity in regions of very low and high Δm^2 by changing the energy and baseline. Generally the reactor and accelerator experiments are classified according to the baseline *i.e.,* short baseline (SBL) experiments covering a few meters, and long baseline (LBL) experiments covering distances up to several hundred kilometers.

Reactor neutrinos and oscillation experiments

Nuclear fission of heavy isotopes (^{235}U, ^{238}U, ^{239}Pu and ^{241}Pu) in the reactors produce pure electron antineutrinos ($\bar{\nu}_e$) flux. On average, each fission reaction produces 200 MeV of energy along with six electron antineutrinos, and for each GW of thermal power, approximately 2×10^{20} electron neutrinos are produced per second [52]. The energies of the neutrinos emitted are mostly around $2 - 3$ MeV, extending up to approximately 8 MeV.

Short baseline reactor experiments like IIL [116], Bugey [117] and Savannah River [118] were unable to observe the disappearance of $\bar{\nu}_e$ due to their short baselines ($\approx 10 - 100$ m). CHOOZ [119, 120] and Palo Verde [121, 122] with baselines ≈ 1 km, were sensitive to $\Delta m^2 \approx 3 \times 10^{-3}$ eV$^2 \approx \Delta m^2_{31}$, but found no evidence of $\bar{\nu}_e$ disappearance and could only constrain the value of θ_{13} and Δm^2_{31}.

Tha KamLAND [6,123,124] reactor neutrino experiment, with an average baseline of about 180 km, is sensitive to Δm^2 in the range measured by solar neutrino experiments. They observed the disappearance of $\bar{\nu}_e$ and further constrained the solar oscillation parameters θ_{12} and Δm^2_{12}.

In 2012, three reactor neutrino experiments Double Chooz [9], Daya Bay [12], and RENO [11] observed $\bar{\nu}_e$ disappearance and measured a non-zero value of θ_{13}. Daya Bay reported a 5.2σ evidence while RENO gave a significance of 4.9σ in measuring non-zero θ_{13}.

Accelerator neutrinos and oscillation experiments

High energy proton beams are focused on to a heavy nuclear target to produce beams of charged pions and kaons, which eventually decay to produce accelerator neutrinos. The direction of the accelerator neutrinos can be modulated by focusing the parent charged particles using a magnetic field, and a pure neutrino beam with ν_μ and $\bar{\nu}_\mu$ is produced at the end by using concrete dumps to block other particles left over in the decay. Accelerator experiments can select either a ν_μ or $\bar{\nu}_\mu$ beam by using a positive or negative charged pion/kaon beam, respectively.

Short baseline accelerator experiments did not find any evidence of neutrino oscillations, except LSND [13], where they observed $\bar{\nu}_\mu$ to $\bar{\nu}_e$ oscillations at a baseline of 30 m. The LSND observed an excess of $87.9 \pm 22.4 \pm 6.0$ $\bar{\nu}_e$ events consistent with oscillations in the Δm^2 range of $0.2 - 10$ eV^2, and is best regarded as an anomaly by other experiments. The MiniBooNE accelerator experiment with a baseline of 541 m [14, 15] investigated the LSND result and obtained an excess of 78.4 ± 28.5 $\bar{\nu}_e$ events, consistent with oscillations in the Δm^2 range of $0.01 - 1$ eV^2 overlapping with the LSND result.

The sensitivity obtained by LSND and MiniBooNE at higher Δm^2 is interpreted as a possible sterile neutrino contribution. In a recent search for the sterile neutrinos [45], combining the data from MINOS [125], Daya Bay [126] and Bugey-3 [117], have excluded the LSND (at 90% CL) and MiniBooNe $\bar{\nu}_\mu \leftrightarrows \bar{\nu}_e$ ($> 3\sigma$) result. They excluded the sterile neutrino mixing phase space allowed by the LSND and MiniBooNE experiments for $\Delta m^2_{41} < 0.8$ eV^2 at a 95% C.L.

The K2K long-baseline accelerator experiment [7] (baseline $\approx$ 250 km) is the first of its kind with a near (300 m) and far detectors. K2K observed the disappearance of ν_μ, and also confirmed the exclusions of CHOOZ and Palo Verde experiments by investigating $\nu_\mu \to \nu_e$ transitions.

The long-baseline accelerator experiments can measure the value of θ_{13}, within an uncertainty related to the unknown in CP-violating phase δ, by observing $\nu_\mu \to \nu_e$ transitions. MINOS [127–129], a long-baseline (735 km) oscillation experiment, and T2K [8, 130, 131], an off-axis long baseline (295 km) oscillation experiment,[47] have observed ν_e appearance and have given constrains on θ_{13}. Another off-axis long-baseline (810 km) experiment, NOνA [132, 133], has observed the appearance of ν_e. OPERA [134, 135] a long baseline (730 km) oscillation experiment has observed the appearance of ν_τ in a high energy ($\langle E_\nu \rangle = 17$ GeV) ν_μ beam from CERN (CNGS).[48]

1.5 Current status of oscillation parameters

The solar neutrino oscillation parameters θ_{12} and Δm^2_{21} have been measured by many solar neutrino experiments and reactor neutrinos experiments like KamLAND. The mass-square difference Δm^2_{21} is small and positive of the order 10^{-5} eV^2. The latest oscillation analysis of solar and KamLAND data [136] gives $\Delta m^2_{21} = (7.37^{+0.17}_{-0.16}) \times 10^{-5}$ eV^2 and $\sin^2\theta_{12} = 0.297^{+0.017}_{-0.016}$. Existing data from SK (Super-Kamiokande) [137], T2K [138], MINOS [139] and NOνA [140] experiments give constraints on atmospheric neutrino oscillation parameters $|\Delta m^2_{32}|$ and θ_{23}. The ν_μ and $\bar{\nu}_\mu$ disappearance in T2K, and the NOνA neutrino disappearance data prefer close to maximal mixing in θ_{23}, whereas the disappearence in MINOS neutrino data and the NOνA anti-neutrino data disfavours the maximal mixing [141]. The neutrino appearance results in T2K and NOνA favour the second octant of θ_{23}. The reactor experiments have measured a non-zero value of θ_{13}, and this prior knowledge of θ_{13} is also exploited by planned accelerator experiments to measure δ. The neutrino and anti-neutrino appearance data in T2K favours $\delta \sim 3\pi/2$ and disfavours $\delta \sim \pi/2$ for both NH and IH. The NOνA neutrino appearance data aligns with the T2K result, but the anti-neutrino appearance data are better described by $\delta \sim \pi/2$. A combined results from T2K, NOνA and MINOS favours NH, where the IH is disfavoured at $\Delta\chi^2 \approx 2$ [141]. A summary of the present

[47] An off-axis can be used to generate a narrow-band neutrino spectrum, as the neutrino energy will be nearly independent of the parent meson energy at angles away from on-axis (away from initial meson direction).

[48] The high energy neutrinos allows the production of τ-leptons, which has a production threshold of ≈ 3.5 GeV

information on these parameters can be found in Table 1.3.

Parameter		best-fit value $\pm 1\sigma$	3σ range
$\sin^2\theta_{23}$	(NH)	$0.582^{+0.015}_{-0.019}$	$0.428 \to 0.624$
	(IH)	$0.582^{+0.015}_{-0.018}$	$0.433 \to 0.623$
$\sin^2\theta_{13}$	(NH)	$0.0224^{+0.0006}_{-0.0006}$	$0.0204 \to 0.0243$
	(IH)	$0.0226^{+0.0006}_{-0.0006}$	$0.0206 \to 0.0246$
$\sin^2\theta_{12}$		$0.310^{+0.013}_{-0.012}$	$0.275 \to 0.350$
Δm^2_{21} $[10^{-5}$ eV$^2]$		$7.39^{+0.21}_{-0.20}$	$6.79 \to 8.01$
Δm^2_{3l} $[10^{-3}$ eV$^2]$	(NH)	$+2.525^{+0.033}_{-0.031}$	$+2.431 \to +2.622$
	(IH)	$-2.512^{+0.034}_{-0.031}$	$-2.606 \to -2.413$
δ [deg]	(NH)	217^{+40}_{-28}	$135 \to 366$
	(IH)	280^{+25}_{-28}	$196 \to 351$

Table 1.3: Current best-fit values of neutrino oscillation parameters and their 3σ allowed ranges assuming normal (NH) and inverted (IH) neutrino mass hierarchies. The values are taken from Ref. [141]. Note that $\Delta m^2_{3l} \equiv m^2_{31} > 0$ for NH and $\Delta m^2_{3l} \equiv m^2_{32} < 0$ for IH.

1.6 Future progress

After the discovery of neutrino oscillations, the neutrino oscillation experiments have come a long way in explaining the neutrino masses and mixing. The hierarchy of neutrino masses, the octant of θ_{23}, and the CP symmetry in the lepton sector are few of the questions yet to be answered by the oscillation experiments. The nature of the neutrino (Dirac or Majorana), the smallness and the absolute scale of the neutrino mass, the existence of sterile and cosmogenic neutrinos, the direct observations of big-bang neutrinos are further frontiers in neutrino physics.

Understanding the neutrino type, whether Dirac or Majorana, will throw light on the mechanism by which it acquires mass and can also explain the smallness of the neutrino mass. The search for neutrino-less double-β decay ($0\nu\beta\beta$) will help in understanding the nature of the neutrinos [51].

Extensive research of the atmospheric and the accelerator sector is planned to identify the mass-hierarchy of the neutrinos. MINOS+, DUNE [142], Hyper-Kamiokande [143], PINGU [144], ORCA [145] and ICAL at the INO [101] are the future experiments in atmospheric sector. Most of these detectors but for MINOS+ and ICAL are unable to measure the charge of the final-state lepton and hence to discriminate a neutrino from an antineutrino; such a distinction is required to identify the mass hierarchy. ICAL at INO [101], can distinguish the charge of the final state lepton to observe the matter resonance separately for atmospheric neutrinos and antineutrinos, thus having sensitivity to the mass-hierarchy. The analysis presented in this thesis determines the reach of INO in measuring the atmospheric neutrino oscillation parameters and mass-hierarchy. A brief description of the ICAL detector is given in the next chapter.

CHAPTER 2

ICAL at INO

The India-based Neutrino Observatory (INO) [101, 146, 147] is a proposed multi-institutional project to build an underground laboratory to conduct high-energy physics, astrophysics and nuclear physics experiments. The main aim of the project is to study the properties of the neutrinos emerging from various natural and laboratory sources. One of the immediate aims is to observe neutrino oscillations in atmospheric neutrinos and deduce the neutrino mass-hierarchy by exploiting matter effects. A brief description of the proposed Iron Calorimeter (ICAL) detector at INO, and its main structural components, which enable it to detect and distinguish a neutrino from an antineutrino, is presented in this chapter.

2.1 Location of INO

The proposed INO site is in south India, close to Pottipuram village in Theni district of Tamilnadu.[1] The observatory will be set up at the coordinates 9°57′47.65″N and 77°16′22.55″E [147], beneath the Bodi West Hills (Fig. 2.1(a)). The natural vertical rock cover, in excess of 1.2 km from the hill overhead, reduces the experimental background due to cosmic ray muons. Figure 2.1(b) shows the comparison of background muons predicted at INO with the other underground experiments around the globe.

The INO will accommodate the ICAL detector, which will observe atmospheric neutrino oscillations, the details of which are explained in the next section. However, INO will also house other experiments like neutrino-less double-β decay, dark matter searches and low energy neutrino spectroscopy ($E_\nu < 1$ MeV); the details

[1] The site was chosen considering many factors: seismic stability, rock mechanics and stability, land availability, accessibility, and environmental conditions.

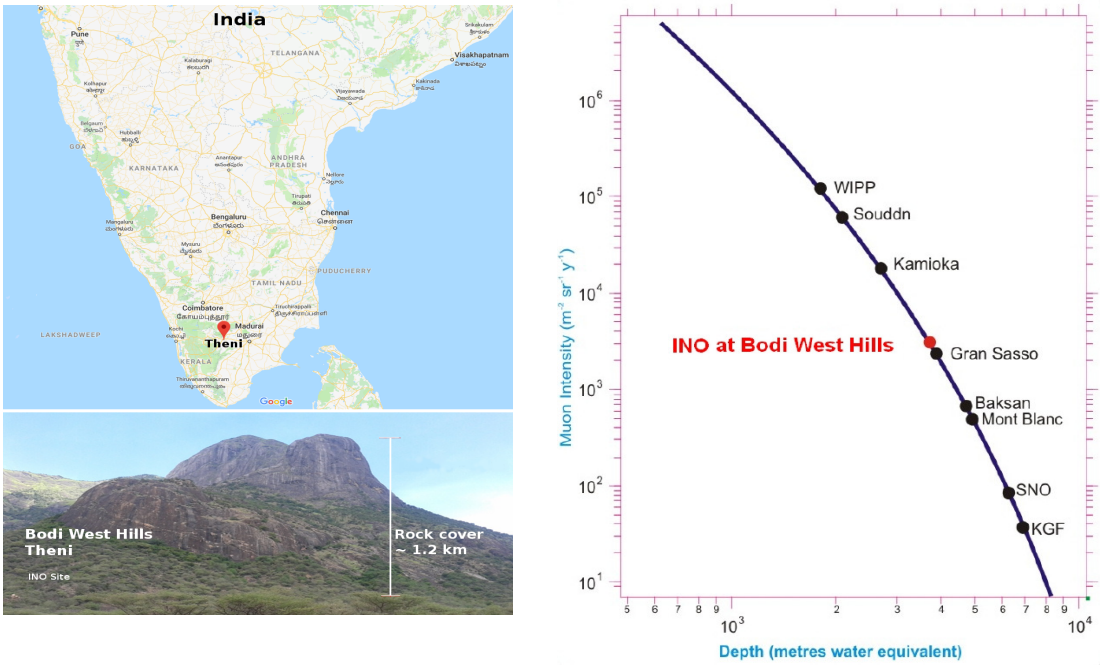

(a) (b)

Figure 2.1: (a) The site proposed for INO - the Bodi hills, Theni. (b) Cosmic muon background as a function of depth [147].

of these experiments are discussed elsewhere [146].

2.2 The ICAL detector

The detection of neutrinos depends on many factors, such as the flux (Φ_ν), cross-section (σ_ν), detector size (number of target nuclei n_d) and the exposure time (t) of the detector. The number of neutrino events detected is directly proportional to these factors, *i.e.* $N \sim \Phi_\nu \sigma_\nu n_d t$. For the atmospheric neutrino detection, the neutrino flux (Refer section 1.3.2) cannot be controlled by the experiment. Also, the neutrino interaction cross-section is very low as they interact very weakly with the matter. Hence to observe a statistically significant number of events in a shorter time scale, the ICAL detector is proposed to be large, with 50 kton of iron as the target material [147].

In the ICAL, the atmospheric neutrinos interact with the iron nuclei and undergo CC and NC interactions. Here the neutrinos of interest are of intermediate and high energy, with $E_\nu \sim 0.4 - 500$ GeV. Hence the relevant interactions in the ICAL are QE and RES at intermediate energies ($E_\nu \lesssim 2$ GeV) and DIS at higher

energies ($E_\nu \gtrsim 2$ GeV), which have a cross-section of the order 10^{-42} m^2 (as given in Sec 1.2). In the detector, the neutrinos are never observed directly, but the final state charged leptons and hadrons produced in the reaction are measured to gauge the neutrino properties.

The ICAL is designed to have very good muon detection efficiency of greater than 85% for muons with a momentum greater than 2 GeV (and an incident zenith angle $\cos\theta_z \geq 0.4$), combined with excellent angular resolution of less than 1° [101]. The ICAL will employ Resistive Plate Chambers (RPCs), a gaseous detector, as the active detectors elements [148] to detect the charged particles passing through them (see section 2.2.3). The most important property of the ICAL will be its ability to discriminate the muon charge using the magnetic field (see Sec. 2.2.2), where it can distinguish between ν and $\bar{\nu}$ events by observing the charge on final state muons.

2.2.1 The ICAL detector geometry

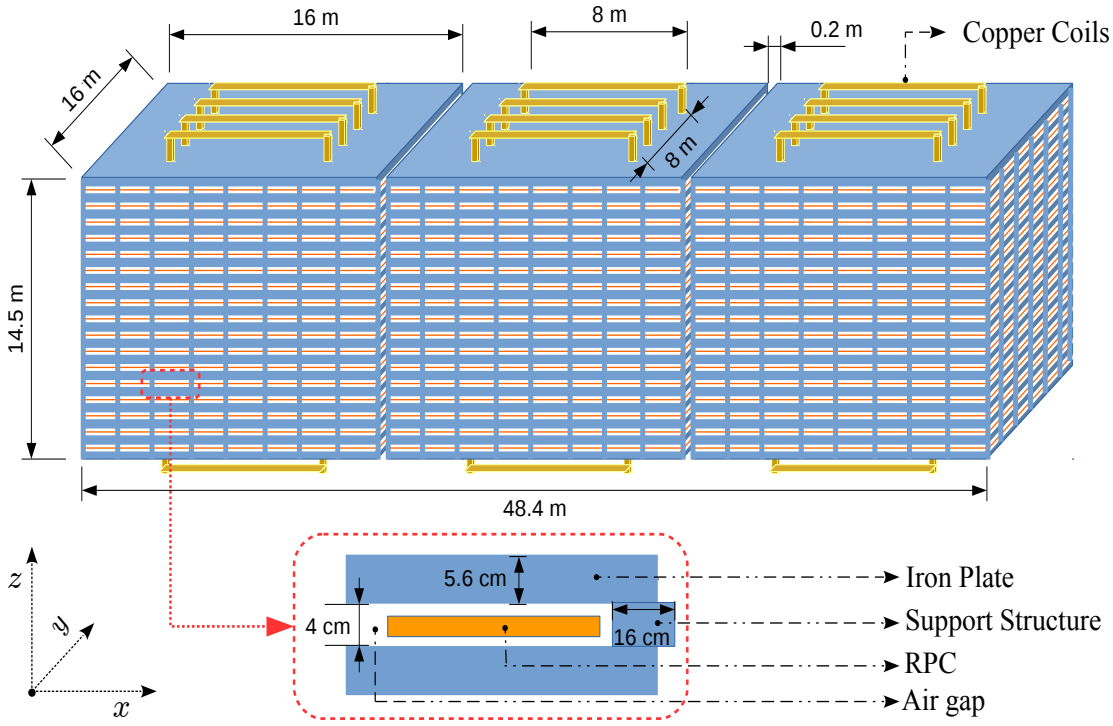

Figure 2.2: Schematic of ICAL detector.

The ICAL detector has a modular structure, consisting of three identical modules each of size 16 m (length in x) ×16 m (breadth in y) ×14.5 m (height in z) separated by 20 cm, as shown in Fig. 2.2. Each module will consist of 151 layers

of 5.6 cm thick iron plates interleaved with 4 cm air gap to deploy the RPCs. The area of each module is 16 m × 16 m, where 32 iron plates of area 2 m × 4 m are deployed in each layer. The iron plates are supported at 2 m intervals in x and y directions by steel support structures of width 16 cm, and the RPCs of size 1.84 m × 1.84 m × 2.5 cm are placed as a grid within the air gaps created by the iron layers and the support structures.

The combined mass of 50 kton, and size of 48.4 m × 16 m × 14.5 m in x, y and z direction, provides the target nuclei to achieve a significant number of neutrino interactions in a reasonable time. The neutrino interactions are expected to be dominant in the iron layers, which contributes to 98% of the mass of the detector [101]. The iron layer will also serve to hold the solenoidal magnetic field [149].

2.2.2 The ICAL solenoidal magnet

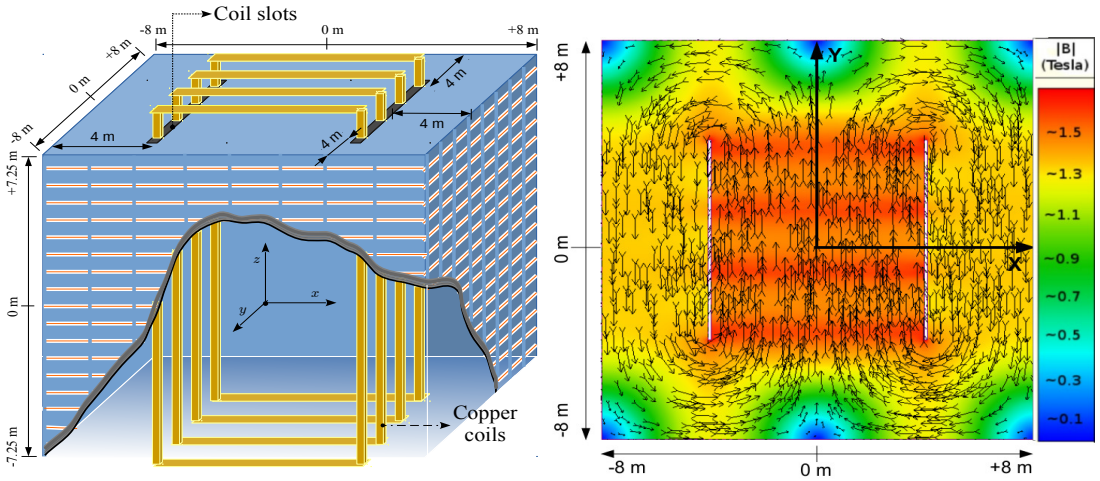

(a) (b)

Figure 2.3: (a) The schematic of the central module of the ICAL showing the solenoidal copper coils and the coil slots. (b) Magnetic field map in the central plate ($z = 0$) of the central module [150]. The magnitude (in T) and direction of the magnetic field is shown using the length and direction of arrows respectively. The magnetic field strength is also shown using the color-code. Note that ICAL has three identical modules, but only the central module is represented here.

The schematic of the central module is shown in the Fig. 2.3(a). The coordinate system is such that the origin ($x = 0$, $y = 0$ and $z = 0$) is at the center of the central module, and the same is used in rest of this thesis.[2] Vertical slots,

[2]Considering all three modules, the ICAL detector will have an extent of ±24.2 m, ±8 m and ±7.25 m in the directions of x, y and z respectively.

extending till $y = \pm 4$ m, are cut at $x = x_0 \pm 4$ m (where x_0 is the center of each module) to accommodate four current carrying copper coils.[3] A current of ~ 5 kA per coil will be supplied to produce a magnetic field upto 1.5 T [149]. Figure 2.3(b) shows the magnitude and direction of the magnetic field produced in the central iron plate ($z = 0$) of the central module. The variation of magnetic field strength in different regions of the detector is discussed in chapter IV

A magnetized detector can change the trajectory of the charged particle, and can measure the charge and momentum of the particle from the direction and curvature of the trajectory that it creates in the detector. The magnetized ICAL detector can measure the charge and momentum of the final state lepton in the neutrino interaction, and can distinguish between the neutrino and an antineutrino interaction. This important feature of the ICAL detector can contribute to unraveling the MH of neutrinos by observing the earth-matter effects in neutrino oscillations for neutrinos and antineutrinos separately.

2.2.3 The Resistive Plate Chambers

The Resistive Plate Chambers are parallel plate gaseous detectors used to detect charged particles based on the principle of gas ionization. The first RPCs were developed by R. Santonico and R. Cardarelli in 1981 [152] as an alternative to discharge spark counters. The excellent detection efficiency, timing resolution (~ 1 ns), spatial resolutions and low cost are the main features of the RPCs.[4]

A schematic diagram of the top and cross-sectional view of the RPC is shown in the Figure 2.5. The RPC consists of two high resistive electrodes (resistivity $\sim 10^{10}-10^{12}$ Ωcm), preferably glass or bakelite, separated by a small gap to confine the mixture of ionizing gas. The ICAL will employ 1.84 m $\times$ 1.84 m RPCs, with glass electrodes of 3 mm thickness separated by a 2 mm gas gap [101]. Cylindrical button spacers made of polycarbonate material (bulk resistivity $> 10^{13}$ Ωcm) are used to maintain a uniform gas gap.[5] A continuous flow of a uniform mixture of

[3]Each coil will be made up of few turns (five for ICAL prototype detector [151]) of electrolytic copper conducting tubing having a central bore for flowing low conductive water to reduce heat.

[4]Recent developments in multi-gap RPCs [153] have achieved less than 100 ps timing resolutions at more than 90% detector efficiency.

[5]The button spacers with a diameter of 10 mm and a width of 2 mm are usually glued between the electrodes to maintain a constant air gap.

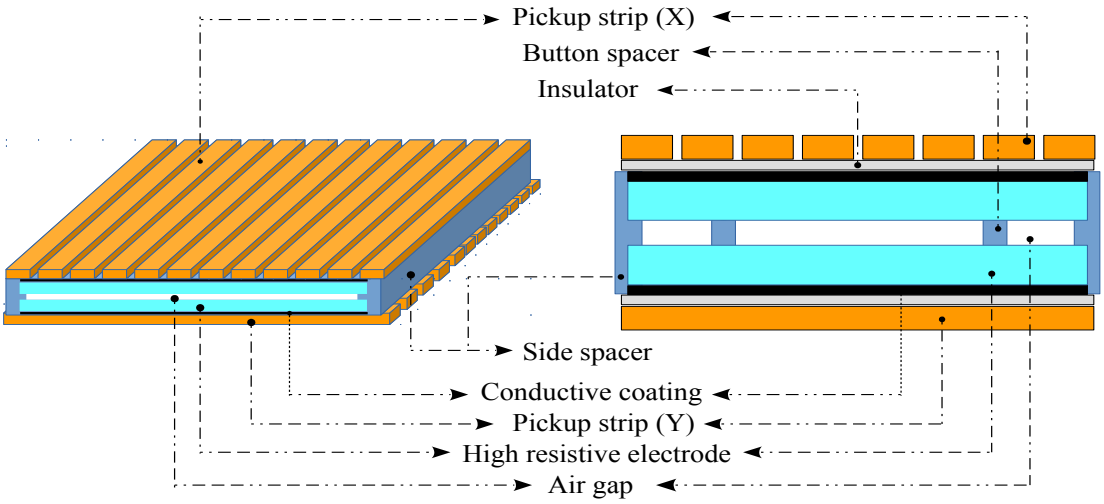

Figure 2.4: Schematic showing the top view (left) and the cross sectional view (right) of the RPC.

Freon (95.2%), Isobutane (4.5%) and SF_6 (0.3%) is maintained through a special inlet and outlet nozzles. The side spacers are glued along the edges to conceal the gas. The outer surface of the two electrodes have a conductive graphite coating, and a high voltage is applied across them to maintain a uniform and constant electric field ($\sim$ 5 kV/mm) in the gas gap. The signal generated by the charged particle passing through the RPC, is picked up by the copper strips (150 μm thick and 2.8 cm wide) placed orthogonally on the external surfaces. Insulating mylar sheets are placed above the graphite coating to detach the copper strips from the conducting surface [154].

Working principle of RPC

The charged particle passing through an RPC ionizes the gas between the electrodes, creating a free electron ion pair.[6] The applied electric field across the RPC accelerates these primary electrons and ions towards the oppositely charged electrodes, where a signal is induced on the copper strips via charge multiplication process inside the gas gap. The multiplication process occurs when the primary electrons from the ionization acquires sufficient energy from the accelerating electric field to further ionize the gas, producing secondary particles, and then secondary producing tertiary particles and so on. The amount of charge multiplication depends up on two factors − the ionization probability per unit

[6]The process of ionization ($A + x \rightarrow A^+ + x + e^-$; where a charged particle x ionizing an atom A) has a typical cross-section of $\sigma \simeq 10^{-20}$ m^2 [155].

path length α,[7] and the probability of the electron capture by the gas per unit path length β. Hence the total number of electrons created via the multiplication process for a path length x is given by [155]

$$n = n_0 \exp[(\alpha - \beta)x], \tag{2.1}$$

where n_0 is the original number of electrons. We define $M = n/n_0$ as the charge multiplication factor.

The value of the multiplication factor M determines the gain of the detector and its mode of operation. When $M > 10^8$ or $(\alpha - \beta)x > 20$, the RPCs begins to operate in streamer mode, where the gas gap breakdown due to discharge and a conductive channel is formed between the electrodes. In the ICAL, the RPCs are designed to operate in avalanche mode[8] [148, 154], where the electrons undergo multiplication and propagation corresponding to a Townsend avalanche with a multiplication factor less than 10^8. This can be achieved by reducing electric field inside the RPC gas gap, or by using suitable gas mixtures [156] where the parameters α and β in Eq. (2.1) depend on the characteristics of the gas.

A gas mixture of Freon (R134a or $C_2H_2F_4$), Isobutane (C_4H_{10}) and Sulphur hexafluoride (SF_6) is used in the ICAL RPCs. The Freon acts as a target for primary ionization and also helps to trap the unbound but energetic secondary electrons produced in the avalanche. The electronegative gas (SF_6) also helps to absorbs the excess electrons from the gas volume before they can initiate a new avalanche, whereas the Isobutane, an organic gas, helps to quench[9] the UV photons produced in the recombination process [154]. A schematic diagram of avalanche production in the RPC is shown in Fig. 2.5, where the primary electron and ion from the ionization drift to opposite electrodes forming an avalanche.[10]

High resistive electrodes prevent the avalanche from spreading throughout the gas volume, and hence the electric field drops down in the small area where the

[7] $\alpha = 1/\lambda$ is the first Townsend coefficient, where λ is the mean free path of the electron.

[8] The streamer modes have higher gain, but lead to a reduced life time for the electrodes. Hence avalanche mode is chosen in ICAL, which has a relatively low signal output.

[9] The gas molecules absorbs the photons and then dissapiates this energy via non-radiative process like dissociation or super-elastic collision.

[10] Since the electrons are more mobile than the heavy positive ions, the avalanche takes the form of liquid drop with electrons at the spherical head [155].

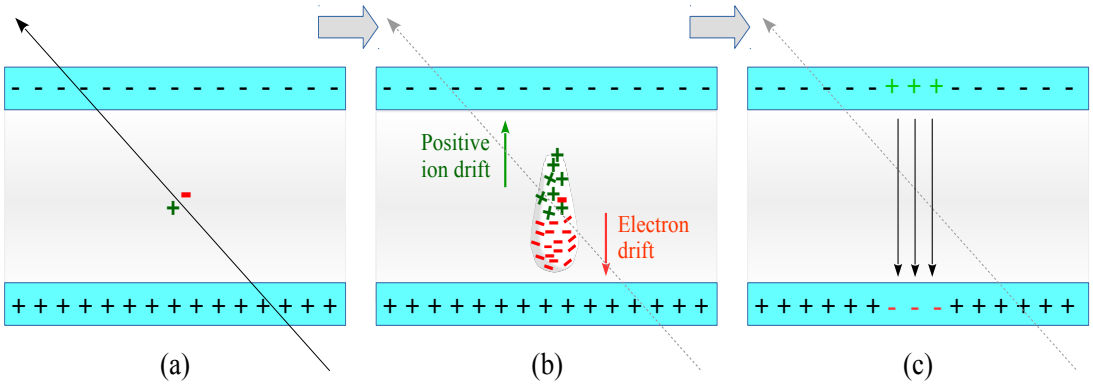

Figure 2.5: Schematic of the charge multiplication via avalanche formation in the RPC. (a) shows the primary ionization, (b) shows the avalanche development and (c) shows the localized change in electric field in the region giving signal.

avalanche reach the electrode. The charge Q_0 deposited in the electrode decays exponentially with time, and the charge Q at any time t is given by

$$Q = Q_0 \exp(-t/\tau) \tag{2.2}$$

where $\tau = \rho\varepsilon_0\varepsilon_r$ is the relaxation time, which depends on the volume resistivity ρ and the dielectric constant ε_r of the material. For glass electrodes, $\rho \sim 10^{12}$ Ωcm, hence the relaxation time τ is ~ 2 s. During this time the electric field is effectively switched off near the area of discharge and the detector stays inactive in the region. The localized drop in field is detected by the copper strips mounted orthogonally on the RPC, providing the position of the particle in $x - y$ plane. Together with the layer number of the triggered RPC, the position of the particle is measured. Finally, the constant high voltage applied across the electrodes, replenishes the drop in electric field after the relaxation time of the detector.

RPCs can be used both as a trigger[11] or as a timing device, based on their application in an experiment. Timing RPCs have time resolutions down to 50 ps [154], and are used in Time of Flight (TOF) measurements. The timing is measured from the spread in RPCs temporal response to a charged particle passing through its gas volume, and is crucial in identifying the directionality of incoming particle. In ICAL, it serves to differentiate up and down going neutrinos, which is essential to observe the oscillations.

[11] As a trigger criterion, a signal in the RPC classifies an event as true or interesting, whereby limiting random coincidences from background hits.

2.2.4 Electronic readouts

The typical signals produced by the RPCs operating in avalanche mode have an amplitude of 2.5 mV across a 50 Ω load with a rise time of about 1 ns [157]. Hence the RPC signal needs a high speed and a low noise pre-amplification before further processing via the data acquisition system (DAQ). The DAQ system includes front- and back-end electronics connected to a computer interface. The front-end electronics converts the amplified analog signal of the RPC to a logical signal via low threshold discriminator circuits.

A dedicated trigger system based on the event topology, generates a global trigger, which is latched along with the back-end electronics. The trigger criteria for the ICAL detector is given by $M \times N/P$, where M is the multiplicity given by the number of strips on one RPC plane that has fired, and N is the number of layers having such M-fold multiplicity among a group of P consecutive layers [158]. The DAQ records strip hit profile, timing, pulse profile *etc.* of an event, only if the specific trigger signal is generated to initiate the DAQ.

2.3 Physics goals of INO-ICAL

The main physics goals of INO-ICAL are as follows [101]:

- To reconfirm the neutrino oscillations in atmospheric neutrinos by observing the first oscillation minimum in $\nu_\mu \to \nu_\tau$ channel,
- Observe the effect of matter on ν_μ and $\bar{\nu}_\mu$ oscillations separately, and determine the MH by measuring the sign of Δm^2_{32}, independent of the CP phase δ.[12]
- Precise measurement of atmospheric oscillation parameters θ_{23} and Δm^2_{32}.
- To determine the true octant of θ_{23}, and its deviation from maximal mixing [101].
- Observation of high energy cosmic muons [160].
- Test for the violation of charge conjugation - parity - time (CPT) or Lorentz symmetry in the neutrino sector [161].

[12]The ICAL is insensitive to CP phase δ [159], as muon events in ICAL are dominated by $P_{\mu\mu}$ where δ appears as a sub-dominant term. Also the uncertainty in the measurement of large range of neutrino path lengths and energy, completely dilutes the dependence on δ.

- Search for the neutrino decay [162], existence of sterile neutrinos, and any non-standard interactions (NSI) [163] effecting neutrino oscillations.
- Indirect dark matter searches [164].

The analysis presented in this thesis mainly concentrates on the first four goals, and the detailed description of other goals are described elsewhere [101, 160–164].

2.4 Summary

The ICAL is primarily designed to observe the atmospheric neutrino oscillations, where the cosmic ray muons form a considerable background. Hence, the ICAL is proposed to be built underneath a rock cover of $\sim$ 1.2 km to remove those backgrounds. The heavy ($\sim$ 50 kton) modular structure of ICAL, mainly iron and glass, will provide enough target material to obtain a statistically significant number of neutrino events in a reasonable time frame.

The ICAL is most sensitive to muons, where it can observe the CC atmospheric muon neutrino and antineutrino interactions. The fast response time of RPC also allows the distinction of upward and downward going events, which is crucial in observing the oscillations. One of the main aims of the ICAL is to measure the MH of the neutrinos by exploiting the matter effects separately in neutrinos and antineutrinos. To allow the distinction between neutrino and antineutrino events, ICAL detector is magnetized to up to $\sim$ 1.5 T so that it detects the charge of the final state lepton to differentiate the event type.

Observing the oscillations and achieving the physics goals of the ICAL depends on the capability of the ICAL to reconstruct various particles in the final states of the neutrino interaction. It is crucial to understand and estimate the capability of the ICAL in measuring them, and how it affects the sensitivity of ICAL in measuring the neutrino oscillation parameters. Hence, a simulation of ICAL detector is performed and is discussed in the following chapters.

CHAPTER 3

Simulation and reconstruction framework

Simulated data are used to estimate the performance of the ICAL and its ability to achieve its physics goals. NUANCE [165] neutrino event generator, along with the atmospheric neutrino flux [98] at the Kamioka site, is used to generate neutrino interactions. A GEANT4 [166] based simulation tool-kit developed by the INO collaboration is used to propagate the secondary particles within a virtual model of the ICAL detector. The output from the GEANT4 simulation is digitized and then reconstructed using track-fitting algorithms to get the direction, energy and momentum of the final-state particles. The flow chart in Fig. 3.1 shows the simulation frame-work implemented and the details of the processes are described in the following sections of this chapter.

3.1 NUANCE

NUANCE is a FORTRAN based software program [165] for generating neutrino interactions. The main interactions modeled in NUANCE include QE scattering, RES production, DIS, coherent nuclear processes,[1] neutrino electron scattering and inverse muon decay (as described in Sec. 1.2). These interactions can be modeled within a target volume that has a user-specified geometry[2] and target materials of known density, nuclear Fermi momenta and binding energy.

A simple ICAL geometry, containing mainly iron and glass components of the detector, with support structures and copper coils are given as the input to

[1] Generally in coherent reactions, the neutrinos scatter of an entire nucleus rather than its individual constituents, with negligible transfer of energy to the target.

[2] The user can specify a simple detector geometry with one or more volume (sphere, cylinder or box), which can be nested accordingly to form a full scale detector.

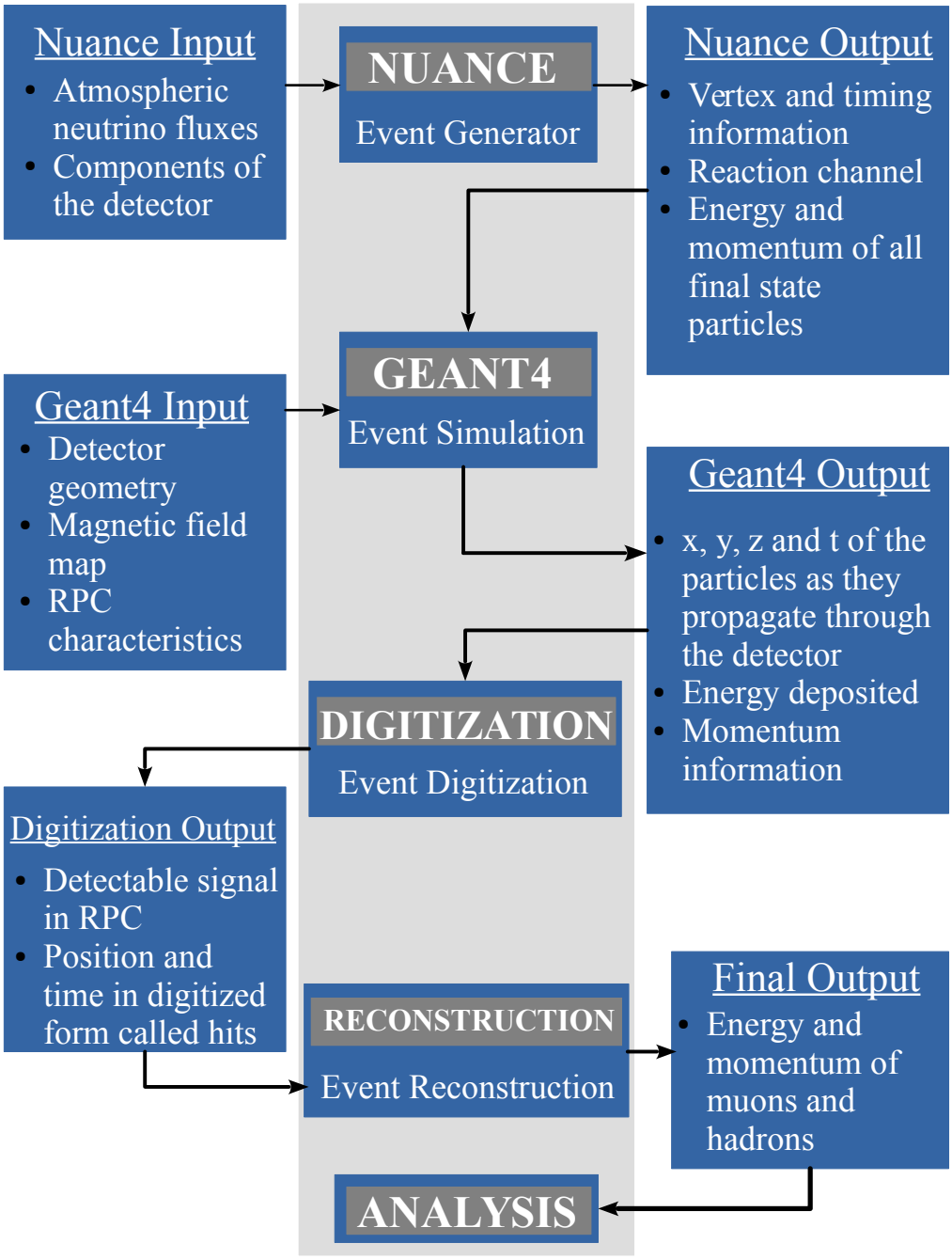

Figure 3.1: Flow chart showing the hierarchy of the simulation frame-work as implemented in the ICAL simulation package.

NUANCE along with the atmospheric neutrino flux [98]. The NUANCE program models the neutrino interactions with the atoms in iron and glass media to generate the secondary particles, where the cross-section and rates of all possible CC and NC interactions are summed over to obtain the total cross-section and event rates. Finally from the calculated event rates, NUANCE generates the neutrino events for the user specified time interval corresponding to the proposed data-taking

period.

NUANCE also has an option to apply neutrino oscillations across varied oscillation parameters. The effect of earth matter on neutrino oscillations is calculated by assuming 25 concentric shells of variable earth matter density, but for the present study we have used NUANCE only to generate neutrino events and oscillations are applied separately.

3.2 GEANT4

GEANT4 [166] is a `C++` toolkit to simulate the passage of particles through matter. The simulation aspects include implementing the geometry of the system, assigning the materials involved, identifying the fundamental particles of interest, generating the primary particles of the event, tracking the particles through the materials and any external electromagnetic field, applying the different physics process governing the particle interactions[3] and investigating the detector response, generating the event data, storing and visualizing the events and associated tracks.

Geometry and material of the system: GEANT4 toolkit provides the classes to create complex geometries with a large number of components and materials.[4] The interleaved structure of the ICAL, with iron and glass RPCs, are modeled using the GEANT4 classes, along with the support structures and the coils for the electromagnetic field. It also provides an option to define the RPCs as the sensitive part of the detector, which records the information needed to simulate the detector response and outputs.

Primary particles: GEANT4 can derive primary particles of the event from internal or external sources. The output from the NUANCE (external source) containing the energy, vertex and timing information of all the primary particles is given as the input to GEANT4. The basic properties of the particle, like the mass, charge and lifetime, are assigned using particle definitions listed in GEANT4. It

[3]GEANT4 covers physics of particle interactions over a wide range of energy and are widely used in many applications of space science, high-energy and nuclear physics and medical imaging.

[4]The GEANT4 class `G4VUserDetectorConstruction` is used to define the geometry and the material composition of the detector, where the user has to define the exact structure and the materials used in the detector.

also computes the physical characteristics, like radiation and interaction lengths, excitation energy loss and Bethe-Bloch coefficients.

Particle transport, interaction and response: In GEANT4 the particles are transported in the virtual detector volume step-by-step, until the particle comes to rest or leaves the detector. All physics processes associated with the particle can contribute to what happens to it during a step. GEANT4 has physics list classes associated with different physics processes,[5] which are applied at different stages of tracking *i.e.*, at rest, along step and post step. The physics processes such as continuous energy loss, multiple scattering, bremsstrahlung, and Čherenkov radiation are applied along the step, whereas the secondary particle production by a decay or interaction is invoked at the end of the step, via the post-step process [166].

The particles are tracked until it has zero kinetic energy, and no tracking cuts are involved which might lead to improper stoppage of the particles. However to reduce the infrared divergences in electromagnetic processes,[6] a production cut is applied, where no more secondary particles are produced, if the primary particle no longer has enough energy to produce secondaries which travel at least 1 mm (production threshold distance).

3.3 Digitization

During the process of digitization, the energy deposited due to the energy loss of the particle in the sensitive parts of the detector is converted to a detectable signal. A charged particle passing through the RPCs generate a signal by ionizing the gas, and the avalanche signal is detected by the mutually orthogonal copper strips (in x and y directions). The exact location of the signal can only be obtained within the spatial resolution of the RPCs given by $w/\sqrt{12}$, where w is the strip width. In ICAL simulations, the strip width has been taken as 2 cm,[7] which corresponds

[5]The classes `G4eIonisation`, `G4eBremsstrahlung` (for electrons), `G4hIonisation`, `G4hLowEnergyIonisation` (for hadrons), and `G4MuEnergyLoss, G4MuBremsstrahlung`, `G4MuPairProduction` (for muons) cover the electromagnetic physics list. The class `G4HadronicProcess` serves as the base-class for all hadronic processes.

[6]Infrared divergences involve the production of large number of photons and electrons with very low energy, and hence increasing the computation time

[7]Strip width is subjected to change when the actual detector is setup (default width is 2.8 cm).

to a 0.57 cm uncertainty in the position.

The anticipated timing resolution of the RPC's time-to-digital converters (TDCs) is $\sim$ 1 ns, along with the mutually independent design of the orthogonal pickup strips, allow the independent timing measurements in x and y strips. Hence the measured data will be composed of two sets: $X[z] = \{(x_1, t_1), (x_2, t_2), ..., (x_n, t_n)\}$ and $Y[z] = \{(y_1, t'_1), (y_2, t'_2), ..., (y_n, t'_n)\}$ refered to as hits, where z is the layer number, and t and t' are the timing measured independently by x and y strips respectively [167]. The digitization involves the translation of these global coordinates into the information on the X^{th} x strip and the Y^{th} y strip at the Z^{th} plane. The ICAL only stores the hit level information from each RPC strip, whereas the analogue level information on the pulse height/shape or energy/charge is not retained.

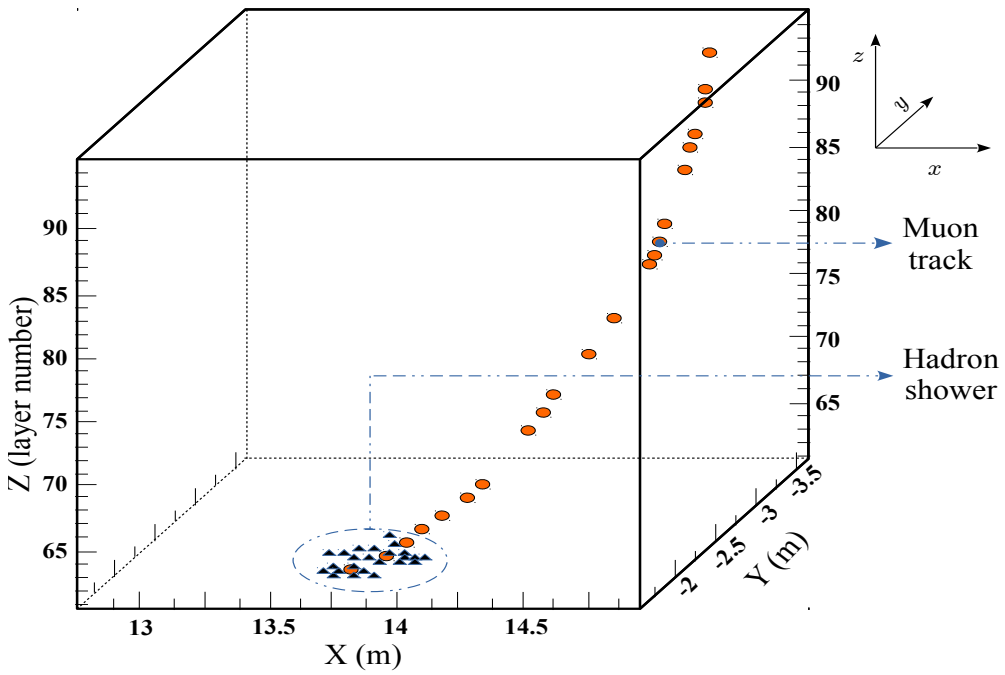

Figure 3.2: Schematic showing the hit pattern generated by muons and hadrons.

The majority of the analysis discussed in this thesis uses CC ν_μ events only, where the information on the incident neutrino is obtained from the information on final state $\mu^\pm$ and the hadrons. The $\mu^\pm$ being a minimum ionizing charged particle, leaves one or two hits per layer on average, forming a well-defined track, whereas the hadrons form several hits per layer forming a shower of hits. Figure 3.2 shows the schematic of a typical hit pattern generated by a single CC ν_μ event, within a certain part of the detector.

3.4 Reconstruction

The energy, direction and charge of the muons is obtained by reconstructing the muon trajectory, where the direction and curvature of the trajectory gives the charge and momentum of the muon respectively. The energy of the hadrons is obtained by calibrating the number of hits that are not associated with the muon track. In rare cases (less than 1% of times), the hadrons leave a well-defined track which may be misidentified as muon. Hence in those cases the longest track is identified as the muon.

The process of reconstruction involves identifying and fitting the particle trajectory in order to measure the properties of the particle. As the digitized hits obtained from the muon and hadron are identical, proper identification and separation of the hits is essential to obtain a better estimate of the muon energies using a fitter, and hadron energies via hit-calibration. Hence in the ICAL, the reconstruction is performed in two steps [167], (i) the track finder, and (b) the track fitter, which are described in the following sections.

3.4.1 The track finder

The track-finder algorithm essentially separates the muon hits from the hadrons, and attempts to find the muon trajectories by investigating hit pattern and progressively traversing the muon hits along all possible directions. The track finder algorithm used in ICAL is based on Ref. [168], which is being used in the MINOS experiment. The general procedure of track finding used in ICAL simulation is as follows [167]:

Forming INOhit and clusters

The output from the digitization process which includes the hits from x and y strips, are used in the track finding algorithm. Most of the events have an interaction vertex within the iron layer, and there is no way to identify the vertex just from the hit pattern. Hence the track finding algorithm does not start from the vertex or rear-end of the track, but processes the whole set of measurements. It

starts by combining the hit information from x and y strips, where the $X[z]$ and $Y[z]$ measurements from the same z plane, and same RPC, with a less than 5 ns time difference are paired to get a meaningful order (x, y, z, t) called the INOhit.[8]

The separation of muon and hadron hits is done based on the number of hits in each layer. Hits in a layer, with more than six hits, are assumed to come from hadrons, as muons only produce an average of one or two hits per layer. Hence the rest of the hits are separately identified as the muon hits, which are further used in the remaining track finder and fitter algorithms. The second step is to form the clusters in each layer, by combining adjacent INOhits which are close to each other (within a separation of three strip widths) to form a single object. These clusters are further processed to identify the one or more possible tracks in an event.

Forming triplets, track-lets and tracks

The clusters in three successive layers are joined to form the triplets, where the slopes of the line segments joining the successive clusters are checked for all possible combinations, and the one with less than 15° difference in slopes of constituent small line segments (joining two clusters) is accepted to form the triplets. These triplets are further joined together to form a chain of triplets called track segments or track-lets, where the angular separation between the triplets is required to be less than 15°. Finally, the tracks are formed by joining a few of the track segments together. In a few cases, where the track finder gives multiple tracks, the longest track is identified as the muon track.

The direction of the particle trajectory (up-ward or down-ward going) is obtained by measuring the sign on dT/dz, where $T(z)$ are the measured timing data of the clusters along the z direction. Once the direction of the track is obtained, the start of the track and the production vertex is also identified.

[8]Here the time t of the INOhit is the average of the time of x and y hits.

3.4.2 The track fitter

The seed track obtained from the track finder is fit using the track fitter based on a Kalman filter algorithm [150,169], where the observables of the track are estimated via the method of least-square minimization. The track in space is regarded as a dynamical system,[9] where a state vector $\bar{X}$ with five parameters describes the track at each point of its trajectory. In the ICAL the state vector is a function of z, and is given by

$$\bar{X}_i = [x, y, dx/dz, dy/dz, q/p]\,, \tag{3.1}$$

where i is the layer number in z direction, x and y are hit points, q/p is the ratio of charge and momentum of the muon, dx/dz and dy/dz are slopes in the z direction respectively. The initial state near the vertex is calculated from the seed track and is given as the input to initialize the Kalman filter.

The Kalman filter

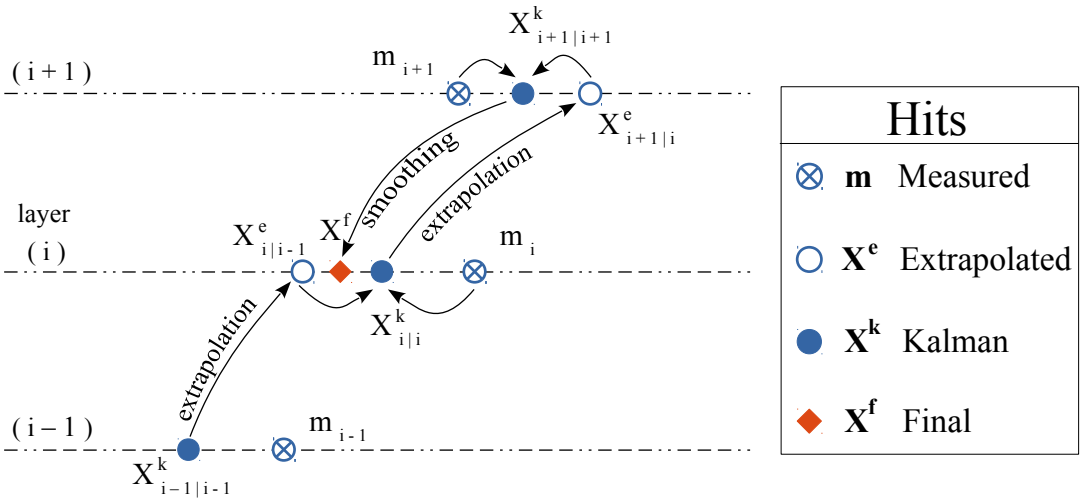

Figure 3.3: Extrapolation, Kalman filtering and smoothing at the i-th layer of the detector.

The Kalman filter [169] is a recursive optimal estimator, which combines the prior knowledge, model predictions and noisy measurements to determine the state of a given dynamical system. The parameters of the state vector $\bar{X}$ are not discrete values, but are distributions with separate mean and variances. The Kalman filter algorithm for track fitting involves three stages, (i) extrapolation, (ii) filtering and

[9] The trajectory of the track is considered as a function of space rather than time.

(iii) smoothing, where it propagates the mean and variance of the state vector all along the particle trajectory to obtain the best estimate of the state. Figure 3.3 shows the estimates obtained from each stage on the i^{th} layer of the detector.

To understand the Kalman filter, lets assume the initial estimate of the mean and variance in the layer $[i-1]$ to be $\bar{X}_{i-1|i-1}$ and $P_{i-1|i-1}$ respectively, where $n|d$ denotes the estimate at n-th layer from d measurements made. The measurements made by the detector in the layer $[i]$ is given by the vector,

$$m_i = h_i \bar{X}_{i|i} + v_i, \tag{3.2}$$

where h_i is the transformation matrix that maps the state vector in to the measurement domain, and v_i is the measurement noise with covariance R_i. To minimize the noise and to estimate an optimal state, the Kalman filter proceeds as follows:

Extrapolation:

Using the previous $[i-1]$ measurements, the Kalman filter predicts (extrapolates) the mean and variances in the next layer $[i]$ using the equations,

$$\bar{X}_{i|i-1} = F_{i-1} \bar{X}_{i-1|i-1} \tag{3.3}$$

$$P_{i|i-1} = F_{i-1} P_{i-1|i-1} F_{i-1}^T + Q_{i-1}, \tag{3.4}$$

where F is the transportation matrix, which propagates the mean and variances to other layers, and it contains the information on local magnetic field which is required to predict the particle motion. The process noise, such as energy loss fluctuations and multiple Coulomb scattering, are included in the noise matrix Q.[10]

Filtering:

The filtering is the process where an optimal state vector is obtained from the predicted and the measured value, by minimizing the incremental χ^2,

[10]The detailed calculations used in ICAL can be found in Ref. [167].

$$\begin{aligned}\Delta\chi^2 = &\left(\bar{X}_{i|i} - \bar{X}_{i|i-1}\right)\left[P_{i|i-1}\right]^{-1}\left(\bar{X}_{i|i} - \bar{X}_{i|i-1}\right)^T \\ &+ \left(z_i - h_i\bar{X}_{i|i}\right)\left[R_i\right]^{-1}\left(z_i - h_i\bar{X}_{i|i}\right)^T,\end{aligned} \tag{3.5}$$

with respect to $\bar{X}_{i|i}$, to obtain the filtered state vector and the covariance matrix as follows:

$$\bar{X}_{i|i} = \bar{X}_{i|i-1} + K_i\left(z_i - H_i\bar{X}_{i|i-1}\right), \tag{3.6}$$

$$P_{i|i} = P_{i|i-1} - K_iH_iP_{i|i-1}, \tag{3.7}$$

where H_i is the projector matrix given by $H_i = \frac{\partial h_i}{\partial X_{i|i-1}}$, and K_i is the Kalman gain matrix given by,

$$K_i = P_{i|i-1}H_i^T\left[H_iP_{i|i-1}H_i^T + R_i\right]^{-1}. \tag{3.8}$$

This process is continued until the end of the track is reached to obtain the fitted track.

Smoothing:

Smoothing involves applying backward filter to re-evaluate the previously estimated state vectors $\bar{X}_i$ using all measurements made in n layers . The smoothed state vector and the covariance matrix at the i-th layer ($i < n$) is given by,

$$\bar{X}_{i|n} = \bar{X}_{i|i} + A_i\left(\bar{X}_{i+1|n} - \bar{X}_{i+1|i}\right), \tag{3.9}$$

$$P_{i|n} = P_{i|i} + A_i\left(P_{i+1|n} - P_{i+1|i}\right)A_i^T, \tag{3.10}$$

where A_i is the smoother gain matrix given by,

$$A_i = P_{i|i}F_i^T\left(P_{i+1|i}\right)^{-1}. \tag{3.11}$$

Finally, the interaction vertex is obtained by extrapolating the track at its beginning by half a layer of iron, as the interactions are supposed to happen in the iron layers. The momentum and charge of the muon is obtained from the best

fit values of q/p near the vertex. Similarly, the direction θ and ϕ of the muon is obtained from the best fit values of the parameters dx/dz and dy/dz. Identifying the charge of the muon differentiates the interaction being that of a neutrino from an antineutrino.

The energy of the hadronic shower can be obtained from the calibration of the hadron hits, which are separated from those associated to a muon during the reconstruction [170]. Hence, the incident neutrino energy can be reconstructed from the combined information on muon and hadron energies. Since hadrons have very poor energy resolution in the ICAL [170], as they have a small number of hits and pass through very few layers, the muon and hadron energies are used separately in the oscillation analysis.

3.5 Summary

The ICAL simulation framework includes the generation of neutrino events, transportation of the secondary particles within a virtual detector and its reconstruction. NUANCE a neutrino event generator, along with the Honda neutrino flux, is used to generate the neutrino interactions within the ICAL detector. The secondary particles generated by the NUANCE are transported in a virtual ICAL detector simulated using a GEANT4 based `C++` code developed by the INO collaboration. The GEANT4 toolkit also applies the necessary physics processes that take place during the propagation of the secondary particles within the detector medium.

The signal induced by the events in the sensitive part of the detector (RPCs) are digitalized to form the position (x, z) or (y, z) and time t, referred to as hits. A CC ν_μ interaction produces a hadron shower along with a muon, which leaves a track in the detector. The muon tracks identified by the track-finding algorithm is fit using a Kalman filter based track algorithm to estimate the muon energy, direction and charge. The sensitivity of ICAL to observe the oscillation, depends on the reconstruction efficiencies and resolutions that are obtained. Hence the factors affecting the reconstruction efficiency and resolutions are studied, and the ways to improve them are discussed in the following chapter.

CHAPTER 4

Simulation response and event selection

The response of the ICAL in reconstructing the energy, direction and charge of the secondary particle produced in the interaction, determines its effective reach in measuring the neutrino oscillation parameters and the related physics goals. The ICAL is mainly sensitive to CC muon neutrinos, where the charge of the muon is measured to differentiate the ν_μ and $\bar{\nu}_\mu$ events. Hence the extent of the sensitivity of the ICAL in measuring the MH depends on the charge identification and reconstruction efficiency of the muon. The following sections briefly discuss the simulated response of the ICAL, where the muon resolution and efficiencies are obtained by generating a CC muon neutrino data set for an exposure of 50 kton $\times$ 100 years. The subsequent sections describe the event-selection process, which improves the reconstructed resolutions and efficiencies by removing the badly reconstructed events.

4.1 Quality of the reconstruction

The CC muon-neutrino data is generated with neutrino energies ranging from 0.4 to 500 GeV. The secondary muon produced loses energy as it traverses the iron layers, and requires a minimum of $\sim$ 200 MeV to pass through three layers, for a track to be reconstructed from the RPC hits. Hence in the following sections, the resolutions and efficiencies are studied for muons with energies greater than 200 MeV.[1]

[1]Note that all particles including hadrons are used in the simulation, but only muon reconstruction efficiencies and resolutions are studied in this chapter.

4.1.1 Reconstruction efficiency

The reconstruction of muons is affected by the non-uniform magnetic field, incident energy and direction, and dead spaces such as coil slots and support structures. Figure 4.1 compares the generator level muon information, refered to as true, with the reconstructed muon data, where Fig. 4.1a and Fig. 4.1b represents the zenith angle (θ_z) and energy (E_μ) distribution of the muons, respectively. The distributions are averaged over the azimuthal angle ϕ.

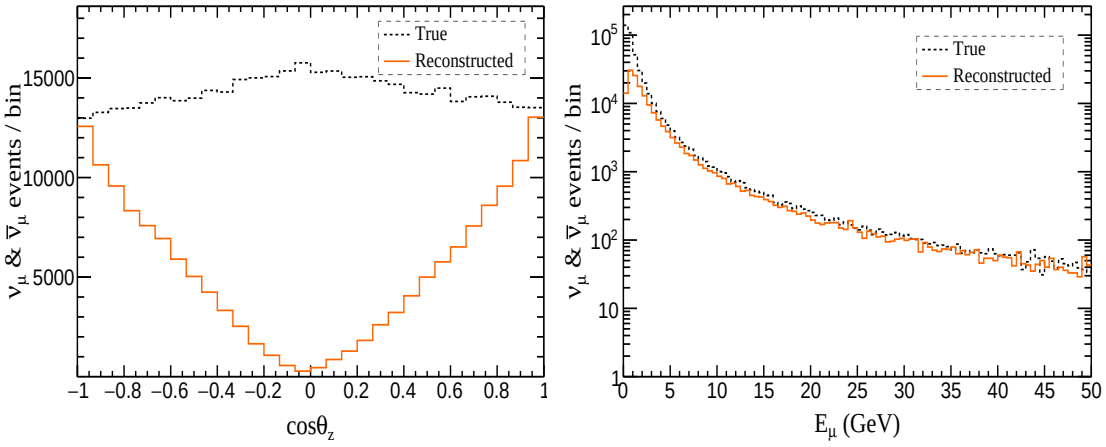

(a) (b)

Figure 4.1: Comparison of the true (dashed black) and reconstructed (solid orange) values of (a) the muon zenith angle, and (b) the energy of the muon, for a 50 kton × 100 years exposure of the ICAL detector.

The dip at $\cos\theta_z = 0$ in the reconstructed distribution of muon zenith angle (see Fig. 4.1a), shows the inability of the detector to reconstruct the horizontal events as they pass through very few layers. Note that $\cos\theta_z = +1$ and $\cos\theta_z = -1$ signify the up-going and down-going directions, respectively.[2]

The reconstruction efficiency (ϵ_{rec}) is calculated from

$$\epsilon_{\text{rec}} = \frac{N_{\text{rec}}}{N_{\text{tot}}}, \tag{4.1}$$

with binomial uncertainty $\delta\epsilon_{\text{rec}} = \sqrt{\epsilon_{\text{rec}}(1-\epsilon_{\text{rec}})/N_{\text{total}}}$, where N_{tot} and N_{rec} are the number of events generated and reconstructed, respectively. The reconstruction efficiency as a function of true muon energy (E_μ^{true}) is shown in Fig. 4.2, where

[2]The zenith angle distribution is largely symmetrical with respect to $\cos\theta_z = 0$, and the mild asymmetry is due to geomagnetic effects.

the variation of efficiency is shown for different bins of the muon zenith angle.

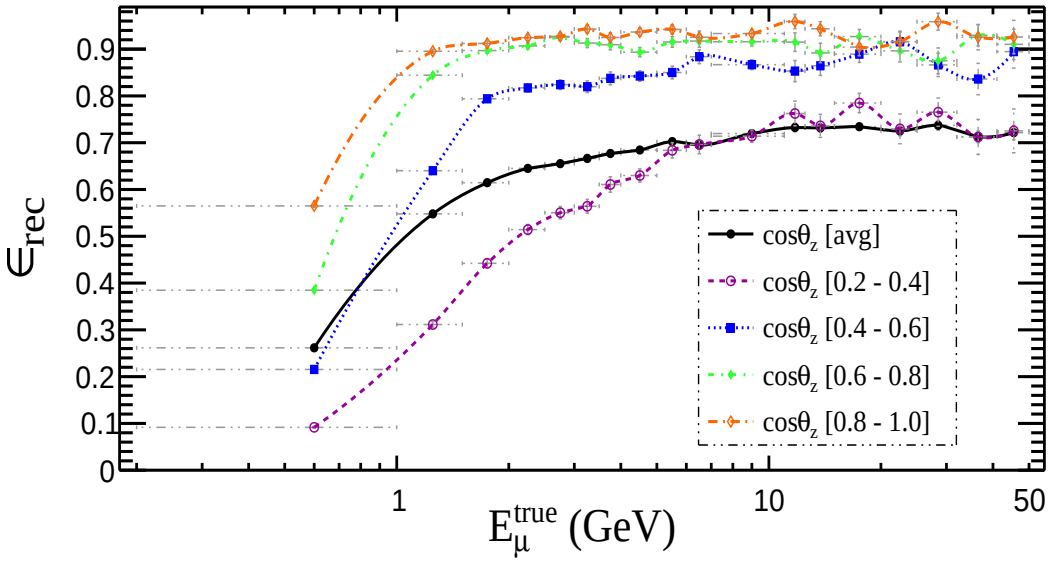

Figure 4.2: Reconstruction efficiency as a function of true muon energy (ϕ averaged) in various zenith angle bins for an exposure of 50 kton $\times$ 100 years. Note the efficiencies in different zenith angle bins: $\cos\theta_z$[0.2 - 0.4] (open circle magenta), $\cos\theta_z$[0.4 - 0.6] (solid square blue), $\cos\theta_z$[0.6 - 0.8] (solid diamond green), $\cos\theta_z$[0.8 - 1.0] (open diamond orange), and $\cos\theta_z$ averaged (solid circle black).

The reconstruction efficiency increases with increasing energy at all incident angles and almost saturates above $E_\mu^{\text{true}} = 2$ GeV. This is due to the fact that the high-energy muons traverse more layers giving a larger number of hits, which results in a well defined track. Hence the reconstruction efficiency increases for more energetic muons because they are relatively easy to reconstruct compared to those with low energy.[3] Also as the zenith angle increases ($\theta_z[0° \rightarrow 90°]$, *i.e.* $\cos\theta_z[1 \rightarrow 0]$), the muons pass through fewer layers giving less hits. Hence the efficiency drops with the increase in the zenith angle (see Fig. 4.2).[4]

4.2 Relative charge identification efficiency

Muon charge identification is crucial in MH determination at ICAL, where it is used to differentiate a neutrino from an antineutrino event,[5] which allows ν_μ and $\bar{\nu}_\mu$ events to be binned separately to observe the matter resonance in neutrino

[3]Low energy muons pass through very few layers leaving a small trail of the helical track with a smaller radius of curvature. Hence they are difficult to reconstruct.

[4]The reconstruction efficiency for the events in the horizontal bins $\cos\theta_z$[0 - 0.2], is significantly worse and is not shown in the Figure 4.2.

[5]In the CC muon-neutrino interaction, μ^+ (μ^-) is a byproduct of $\bar{\nu}_\mu$ (ν_μ) interaction.

oscillations.

The relative charge identification (CID) efficiency (ϵ_{cid}) is the fraction of events identified with correct muon charge among the total reconstructed events, given by the expression

$$\epsilon_{\text{cid}} = \frac{N_{\text{cid}}}{N_{\text{rec}}}, \tag{4.2}$$

with binomial uncertainty $\delta\epsilon_{\text{cid}} = \sqrt{\epsilon_{\text{cid}}(1-\epsilon_{\text{cid}})/N_{\text{rec}}}$, where N_{rec} is the number of events reconstructed and N_{cid} is the number of events with correct CID. Figure 4.3 shows the relative CID efficiency as a function of true muon energy for different bins in muon zenith angle.

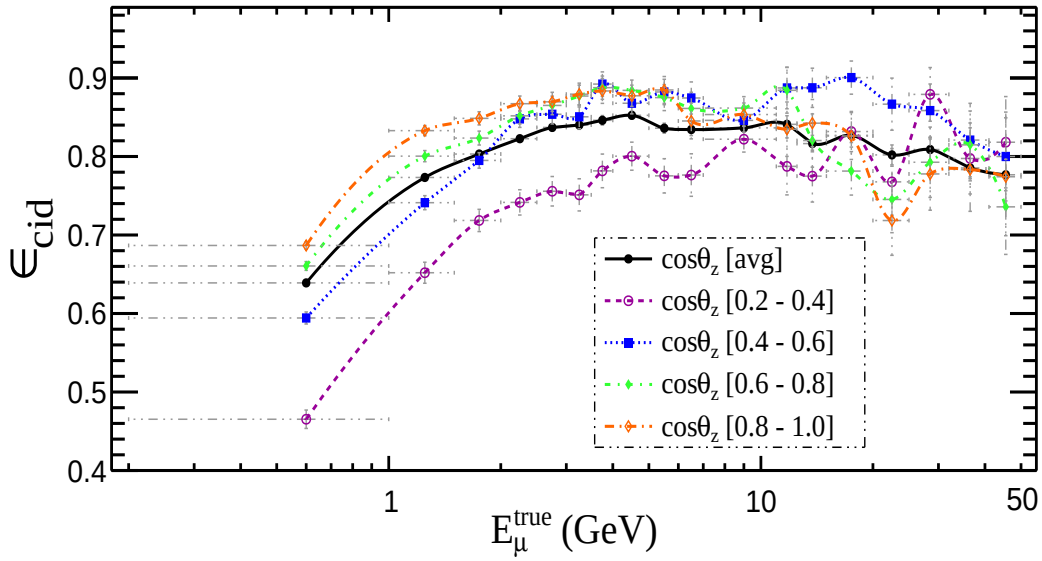

Figure 4.3: Charge identification efficiency as a function of true muon energy (ϕ averaged) in various zenith angle bins for an exposure of 50 kton $\times$ 100 years. Note the efficiencies in different zenith angle bins: $\cos\theta_z$[0.2 - 0.4] (open circle magenta), $\cos\theta_z$[0.4 - 0.6] (solid square blue), $\cos\theta_z$[0.6 - 0.8] (solid diamond green), $\cos\theta_z$[0.8 - 1.0] (open diamond orange), and $\cos\theta_z$ averaged (solid circle black).

The CID is obtained from the direction of the curvature of the muon trajectory in the magnetic field. At low energies, the smaller curvature of the track are harder to reconstruct due to multiple scattering and shorter trajectories, whereas at higher energies the muon passes through many layers forming a long track with a large radius of curvature. Hence the relative CID efficiency increases with increase in muon energy, as the reconstruction of the direction of the trajectory tends to be easier with increased track length and the number of hits. However, for E_μ^{true} greater than 10 GeV there is a small decrease in ϵ_{CID} due to the tracks becoming straighter, which means that the sign of the curvature becomes less

straightforward to determine. Also as a muon passes through less layers with increasing muon zenith angle ($\theta_z[0° \rightarrow 90°]$, *i.e.* $\cos\theta_z[1 \rightarrow 0]$), the CID efficiency decreases with increasing θ_z (see Fig. 4.3).

4.2.1 Muon energy resolution

The muon energy resolution is a measure of the quality of muon energy reconstruction. Figure 4.4 shows the residual distribution of muon energy, *i.e.* the difference in reconstructed (E_μ^{reco}) and true muon energy (E_μ^{true}), in different bins of the true muon energy.[6] The resolutions are obtained from the root mean square (RMS) values, where about 90% of the reconstructed events are considered in each energy bin.

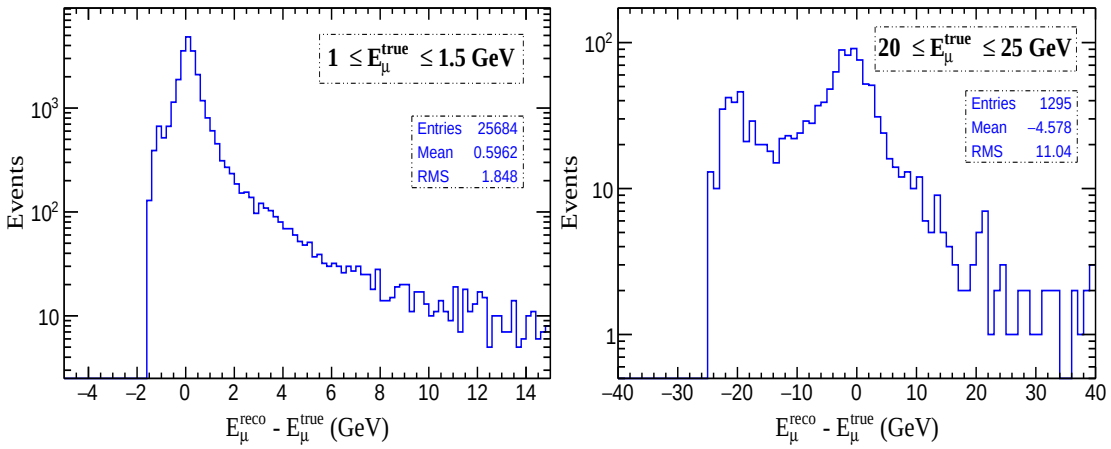

(a) (b)

Figure 4.4: Difference in reconstructed (E_μ^{reco}) and true (E_μ^{true}) energy of the muon for the (a) low-energy bin of [1 to 1.5] GeV in E_μ^{true} and (b) high-energy bin of [20 to 25] GeV in E_μ^{true}.

The low-energy distribution (see Fig. 4.4a) peaks at zero as expected, but with an asymmetrical positive tail, where few events are mis-reconstructed with high energies. The residual energy distribution at high energies show an additional peak (at $\Delta E_\mu = -20$ GeV in Fig. 4.4b), other than the expected peak at zero. This is due to the presence of partially contained (PC) events, where the $\mu^\pm$ leaves the detector volume and the part of the track within the detector are reconstructed with low energies [171]. Muons with low energies are fully contained within the

[6] The y-axis in Fig. 4.4 is plotted using a vertical logarithmic scale to clearly differentiate the number of events in the tail of the distribution.

detector, hence no additional peaks are observed in the low-energy bins.

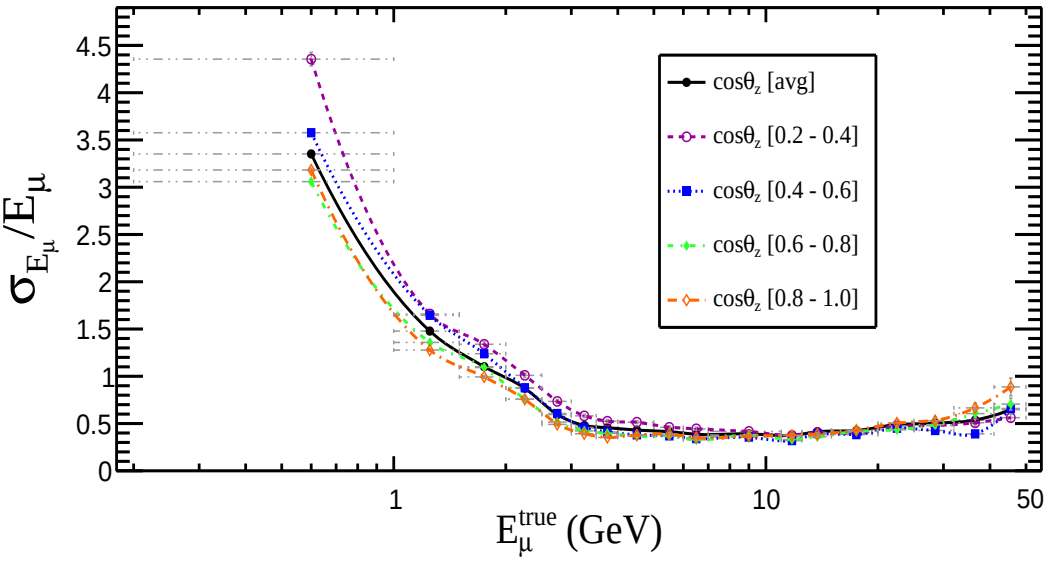

Figure 4.5: Muon-energy resolution as a function of true muon energy (ϕ averaged) in various zenith angle bins for an exposure of 50 kton $\times$ 100 years. Note the efficiencies in different zenith angle bins : $\cos\theta_z$[0.2 - 0.4] (open circle magenta), $\cos\theta_z$[0.4 - 0.6] (solid square blue), $\cos\theta_z$[0.6 - 0.8] (solid diamond green), $\cos\theta_z$[0.8 - 1.0] (open diamond orange), and $\cos\theta_z$ averaged (solid circle black).

The muon-energy resolution as a function of the true muon energy in different zenith-angle bins is shown in Fig. 4.5, where the energy resolution R_E (and the uncertainty δR_E) is defined as

$$R_E = \frac{\sigma_{E_\mu}}{E_\mu} = \frac{\text{RMS}}{E_\mu}$$
$$\delta R_E = \frac{\delta\text{RMS}}{E_\mu}. \tag{4.3}$$

The muon energy resolution improves with increase in the energy, as the number of hits and the number of layers traversed by the muon increases. However at high energies the muons have enough momentum to exit the detector, where they form straight line trajectories with large radii of curvature. Hence the energy resolution improves initially (till 10 GeV) and then it gets relatively worse ($\sim 60\%$) in the high-energy region (20 to 50 GeV).

4.2.2 Muon zenith-angle resolution

The muon angular resolutions are calculated in terms of $\cos\theta_z$. Figure 4.6 shows the residual $\cos\theta_z$, *i.e.* the difference in the cosine of the reconstructed ($\cos\theta_{\text{reco}}$)

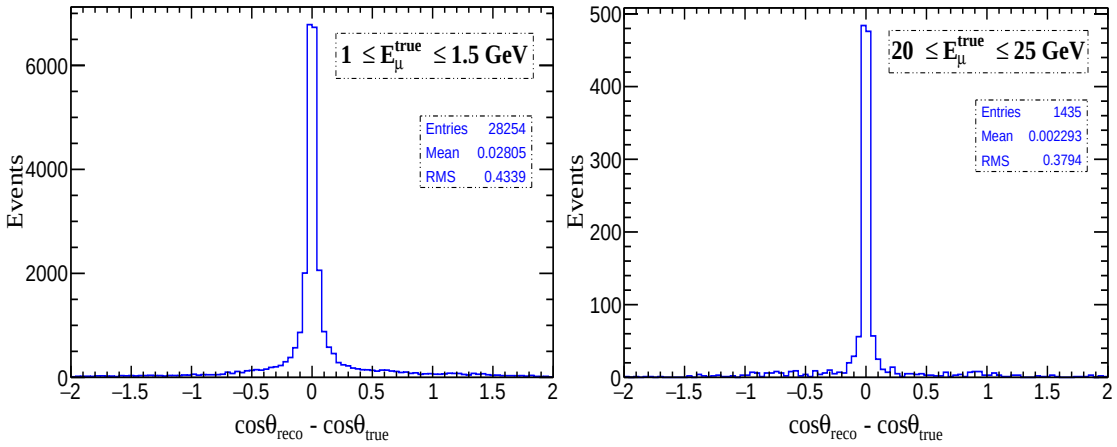

(a) (b)

Figure 4.6: The difference in cosine of the reconstructed ($\cos\theta_{\text{reco}}$) and true ($\cos\theta_{\text{true}}$) zenith angle of the muon for (a) low energy bin of [1 to 1.5] GeV in E_μ^{true} and (b) high energy bin of [20 to 25] GeV in E_μ^{true}.

and true ($\cos\theta_{\text{true}}$) values of the muon zenith angle, in different bins of the true muon energy.[7] The angular resolutions (and the error in resolutions) is estimated using the RMS values (and the error in RMS) calculated in each energy bin, where all the events that are reconstructed are considered. Figure 4.7 shows the muon angular resolution as a function of true muon energy in different $\cos\theta_z$ bins.

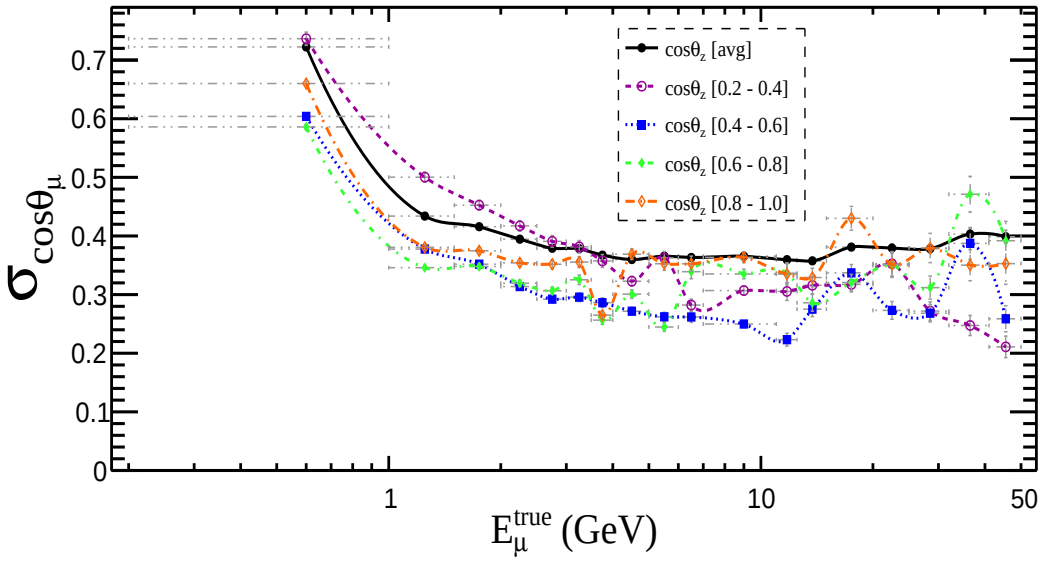

Figure 4.7: Muon angular resolution as a function of true muon energy (ϕ averaged) in various zenith-angle bins for an exposure of 50 kton $\times$ 100 years. Note the efficiencies in different zenith-angle bins: $\cos\theta_z$[0.2 - 0.4] (open circle magenta), $\cos\theta_z$[0.4 - 0.6] (solid square blue), $\cos\theta_z$[0.6 - 0.8] (solid diamond green), $\cos\theta_z$[0.8 - 1.0] (open diamond orange), and $\cos\theta_z$ averaged (solid circle black).

[7] Figures 4.6a and 4.6b show the residual zenith angle distribution of muons in low (1 to 1.5 GeV) and high (20 to 25 GeV) energy bins respectively.

The muon angular resolution improves with increasing muon energy. The muons passing trough the body diagonal ($\cos\theta_z[0.4 - 0.8]$) of the ICAL detector are less likely to encounter or pass through a large part of the dead spaces in the detector like the support structures. Hence they show better angular resolution than the vertical and horizontal muons (see Fig. 4.7).

4.3 Event selection

The reconstruction of muons is limited by the geometrical design of ICAL, where it is affected by the non-uniform magnetic field and dead spaces such as coil slots and support structures. The horizontal muons can only pass through very few layers due to the geometrical constrains, and hence they give very few hits which results in poor reconstruction. Also the muons crossing a support structure might be reconstructed as two separate tracks with different energy and direction. Similarly, the partially contained muons are not well reconstructed, as only a part of the track is observed within the detector. Hence to remove these poorly reconstructed events to obtain a sample of better reconstructed data, certain event-selection criterion are applied as in Ref. [171, 172]; the criteria vary depending on the magnitude of the magnetic field in the regions of the ICAL detector. The details are explained in the following sub-sections.

4.3.1 Definition of the regions

The ICAL detector employs a magnetic field up to 1.5 T,[8] where the strength and the direction of the magnetic field determines the quality of reconstruction. The magnetic field breaks the azimuthal symmetry of the detector, whereby the muons with the same zenith angle and energy have a different response in the detector for different azimuthal angles [171, 172]. Hence the different selection criteria are applied on the basis of the magnetic field strength in the region where the events lie.

Depending on the magnitude of the magnetic field, the entire ICAL is divided

[8]Due to the edge effects of the solenoidal magnet, the magnetic field is non-uniform and rapidly varying in different regions of the detector.

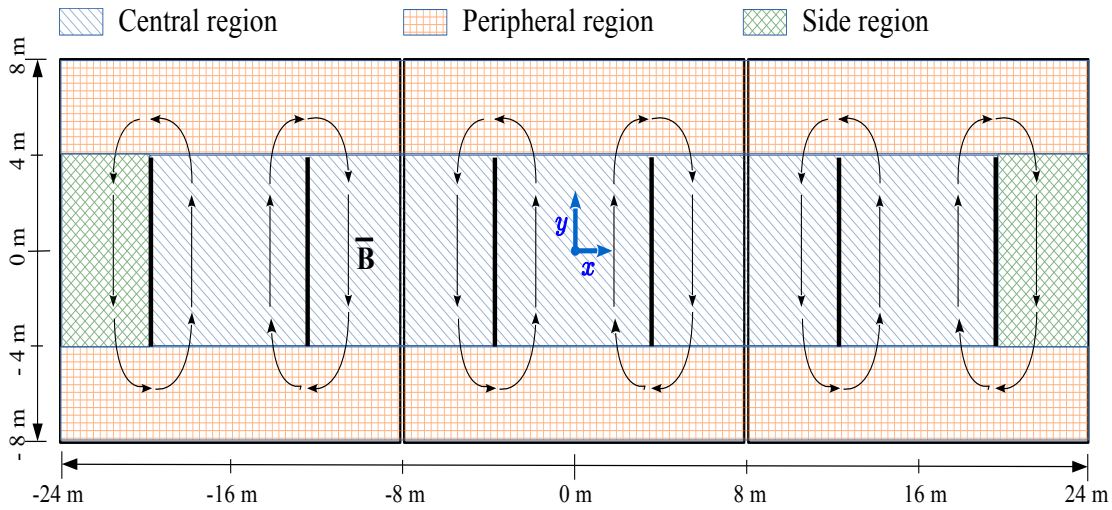

Figure 4.8: Cross-sectional view of ICAL (all three modules) in the x - y plane, showing the division of regions on the basis of the magnetic field strength. The arrows indicate the direction of the solenoidal magnetic field in those regions.

into three regions central, side and peripheral, as shown in the cross-sectional (x - y plane) view of the ICAL in Fig 4.8.[9] Considering three modules of size 16 m $\times$ 16 m $\times$ 14.4 m each and choosing an origin at the centre of the central module, the ICAL will have conventionally 24 m, 8 m and 7.2 m on either side of the origin in x, y and z directions respectively (see Fig. 4.8). The variation of the magnetic field strength in each of the regions is shown in Fig. 4.9. The position, size and the magnetic properties of the separate regions are as follows:

Central region (CR)

The region $|x| \leq 20$ m and $|y| \leq 4$ m, with z unconstrained is defined to be the central region (shown as blue striped region in Fig. 4.8). Here the magnetic field is highest and reaches up to 1.5 T in magnitude. It is also fairly uniform with $\approx 12\%$ coefficient of variation[10] (see Fig. 4.9), despite the fact that the direction of the magnetic field would flip along y in the regions $|x| < 4$ m, 4 m $\leq |x| <$ 12 m and 12 m $\leq |x| <$ 20 m as denoted by the direction of arrows in Fig. 4.8.[11]

[9] Note that the separation of regions is only based on the strength, rather than the direction of the magnetic field.

[10] Coefficient of variation is defined as the ratio of standard deviation σ to the mean.

[11] The magnetic field lines are in one direction within the coils and in opposite directions outside the coils (smaller in magnitude by 13%) for a single module, but with all three modules aligned the magnitude of the magnetic field will be continuous for $|x| \leq 20$ m (ignoring the 20 cm gap between the modules).

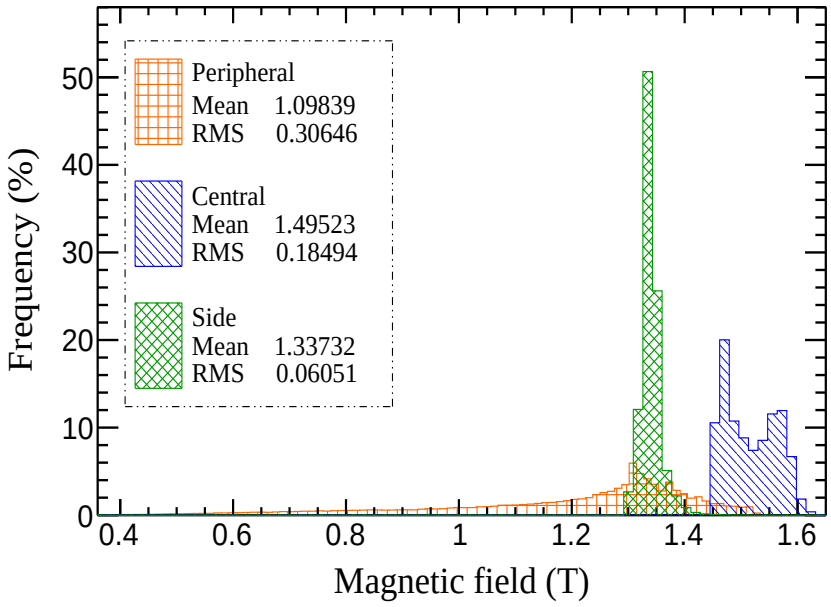

Figure 4.9: The variation of magnetic field strength in the central, side and peripheral regions of the ICAL in the x - y plane, where each point corresponds to the magnetic field measurement made in steps of $\Delta x = \Delta y = 0.05$ m.

Peripheral region (PR)

The region $|y| > 4$ m with z unconstrained is defined to be the peripheral region, where it has maximally varying magnetic field in both magnitude and direction due to the fringe field arising from the solenoidal ICAL magnet. The magnetic field in this region reaches a maximum around 1 T with $\approx$ 28% coefficient of variation (see Fig. 4.9).

Side region (SR)

The region $|x| > 20$ m and $|y| \leq 4$ m, with z unconstrained is defined to be the side region, where the magnetic field is smaller by $\approx$ 13% and opposite in direction to the adjacent central region. The side region has a uniform magnetic field of 1.3 T, with less than 5% coefficient of variation (see Fig. 4.9). The properties of the regions are summarized in the Table 4.1.

The central region is the largest among the three regions, where the events generated within the central region are either fully contained or will leave a long enough track within the detector. The side region is the smallest, and has better uniform magnetic field among the three regions. The events generated in the side

Region	Position (m)		Magnetic field	
	x	y	Strength (T)	Variation coefficient
Central	$\|x\| \leq 20$	$\|y\| \leq 4$	1.5	12%
Peripheral	unconstrained	$\|y\| > 4$	1.0	28%
Side	$\|x\| > 20$	$\|y\| \leq 4$	1.3	13%

Table 4.1: The position of different regions, and strength of magnetic field within each region. The z axis of each region is unconstrained and hence not specified.

and peripheral regions are more likely to leave the detector, as they are near the edge of the detector.

4.3.2 Selection criterion

Appropriate event selection criteria are applied in each of the regions to achieve a sample of reconstructed events that are well reconstructed, which are then used in the oscillation analysis. Most of the event selection criterion are applied in all the regions (common selection) and a few are region specific as described below:

χ^2 selection (CS)

The χ^2 selection is applied across all the regions, where the events with $\chi^2/\text{ndf} < 10$ are selected. The χ^2 is the chi-square of the fit for the track obtained from the Kalman filter, and ndf is the number of degrees of freedom. Here $\text{ndf} = 2N_{\text{hits}} - 5$, where the Kalman filter fits five parameters to form the track and N_{hits} are the number of hits associated with the track, with each hit having two degrees of freedom as they are either in (x, z) or (y, z) coordinates.[12]

Horizontal event selection (HS)

The horizontal events ($\cos\theta_z$[0 - 0.35])[13] pass through very few layers, where the reconstruction efficiency is $\sim$ 18% (38% less than the rest of the events combined). The energy and angular resolutions for the horizontal events are 60% and 16% worse in comparison to the other events.[14] Hence, to remove the poorly re-

[12]For more details on the Kalman filter refer Sec. 3.4.2.
[13]$\cos\theta_z = 0$ to 0.35 is a loose selection for horizontal events which is used in the analysis.
[14]The values are obtained for the events averaged over the muon energy and azimuthal angle.

constructed horizontal events, a selection criterion of $|\cos\theta_z| \geq 0.35$ is applied in all the regions.

z-vertex selection (ZS)

A cut on the z-position of the event vertex ($z_{\rm v}$) is applied in all the regions to limit the events with track leaving from top and bottom of the detector. The up-going events with vertices lying below $z = 6$ m and the down-going events with vertices lying above $z = -6$ m are selected, as they would have enough layers to form a track.

$N_{\rm hits}$ selection (NS)

The $N_{\rm hits}$ selection is a region-specific selection, which is mainly applied to remove the badly-reconstructed events from the partially-contained (PC) events. All the events with the interaction vertices in the central region, and with $N_{\rm hits} > 0$, are selected as they either have a reasonable track length or are contained within the detector to reconstruct the direction and momentum. The rest of the events within the peripheral and side regions are classified into partially-contained (PC) and fully-contained (FC) events according to the end position of the track. If the track end lies within $|x| \leq 23$ m and $|y| \leq 7.5$ m and $z \leq 7$ m, then the event is classified as FC and is selected. The remaining events are classified as PC, and a selection criterion of $N_{\rm hits} > 15$ is applied on all such PC events.

Other selections (OS)

Other selections include placing criteria on track observables such as the reconstructed energy, azimuthal and zenith angle, which are made based on the analysis requirement and the general trend of poor reconstruction that can be observed in certain values of reconstructed variables. The analysis presented in this thesis is based only on the CC neutrinos with energies less than 50 GeV, hence a selection criterion $E_\mu^{\rm rec} \leq 50$ GeV is applied. Also an additional selection of $E_\mu^{\rm rec} \geq 0.2$ GeV is applied, as the successful reconstruction of muon track requires the muon to traverse a minimum of three layers.[15]

[15]The 95% of the data sample corresponds to muon events within 0.2 to 50 GeV.

Almost 9% and 11% of the reconstructed events were observed to be wrongly reconstructed at $|\cos\theta_z^{\rm rec}| \geq 0.9999$ and $|\phi_{\rm rec}| \leq 0.07$ rad respectively. Hence a selection criteria of $|\cos\theta_z^{\rm rec}| \leq 0.9999$ and $|\phi_{\rm rec}| \geq 0.07$ rad are also applied. Table 4.2 lists the selection criteria used in this analysis.

Item	Criterion	Region	Events
CS	$\chi^2/\text{ndf} < 10$	all	all
HS	$\lvert\cos\theta_z\rvert \geq 0.35$	all	all
ZS	$z_{\rm v} < 6$ m	all	up going
	$z_{\rm v} > -6$ m	all	down going
NS	$N_{\rm hits} > 0$	CR	all
		PR	FC
		SR	FC
	$N_{\rm hits} > 15$	PR	PC
		SR	PC
OS	$E_\mu^{\rm rec} \geq 0.2$ GeV $E_\mu^{\rm rec} \leq 50$ GeV $\lvert\cos\theta_z^{\rm rec}\rvert < 0.9999$ $\lvert\phi_{\rm rec}\rvert \geq 0.07$ rad	all	all

Nomenclature
CS - χ^2 selection
HS - Horizontal selection
ZS - Z vertex selection
NS - Nhits selection
OS - Other selection
CR - Central region
PR - Peripheral region
SR - Side region
FC - Fully contained
PC - Partially contained

Table 4.2: List of different selection criteria applied in different regions, with the right column defining the acronyms used.

4.4 Effect of selection criterion

The event selection removes most of the events that are badly reconstructed, hence the number of reconstructed events drops from 41% to 22%. The statistical impact of event selection is discussed in the next section, while its effect on the quality of reconstruction is discussed here.

Figure 4.10 compares the reconstructed muon information with (WS) and without (WOS) event selection, where Figs. 4.10a and 4.10b show the zenith angle (θ_z) and energy (E_μ) distribution of muons respectively (averaged over azimuthal angle ϕ).

The reconstruction efficiency and resolution increases with event selection. Figure 4.11 shows the effect of event selection on the residual distribution of muon energy (Figs. 4.11a and 4.11b) and zenith angle (Figs. 4.11c and 4.11d) in various bins of true muon energy.

The tails of residual distributions decreases considerably after event selection,

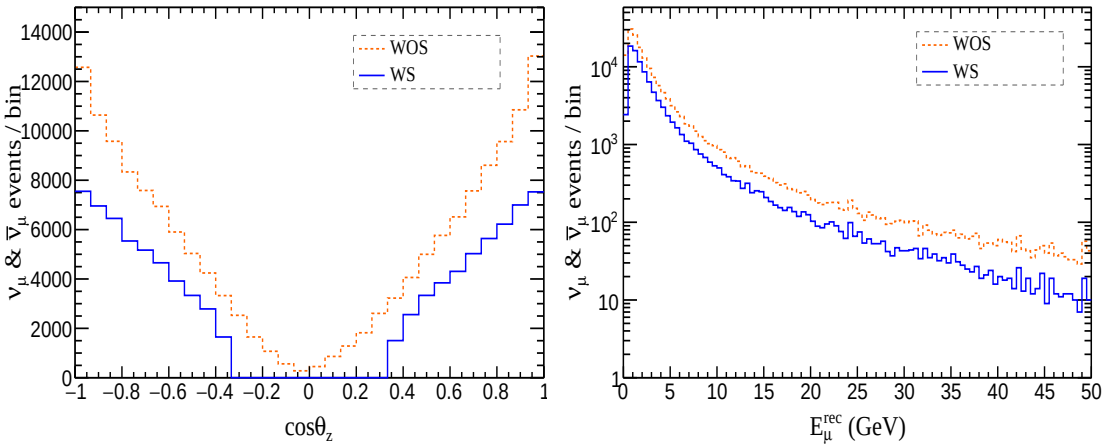

(a) (b)

Figure 4.10: With (WS) and without (WOS) selection comparison of (a) muon zenith angle and (b) the energy of the muon, for a 50 kton × 100 years exposure of the ICAL detector.

which is evident from the reduction of the RMS values in Fig. 4.11. Hence the fraction of low energy events that were reconstructed at high energy is reduced via the event selection (see Figs. 4.11a and 4.11b). Also note the reduction of the additional peak in the residual distribution of muon energy (see 4.11b), which resulted from the wrong reconstruction of highly energetic partially-contained events as events with low energy. Hence the event selection is also able to reduce the mis-reconstructed events among the partially-contained events. Figure 4.12 shows the improvement in the efficiencies and resolutions of the reconstructed events after event selection.

The resolution improves considerably at low and high energies with the event selection applied. An overall improvement of 23% and 19% is observed in energy and zenith angle resolution of muons (averaged over muon energy, zenith and azimuthal angles) after the event selection. The CID efficiency shows $\sim$ 6% to 10% improvement at all muon energies, after the event selection. The reconstruction efficiency decreases as expected, and an overall 42% reduction is noted (averaged over muon energy, zenith and azimuthal angles).

4.5 Statistical effect of selection

The event selection removes about 47% of the events that are reconstructed. The fraction of the number of reconstructed events in central, peripheral and side

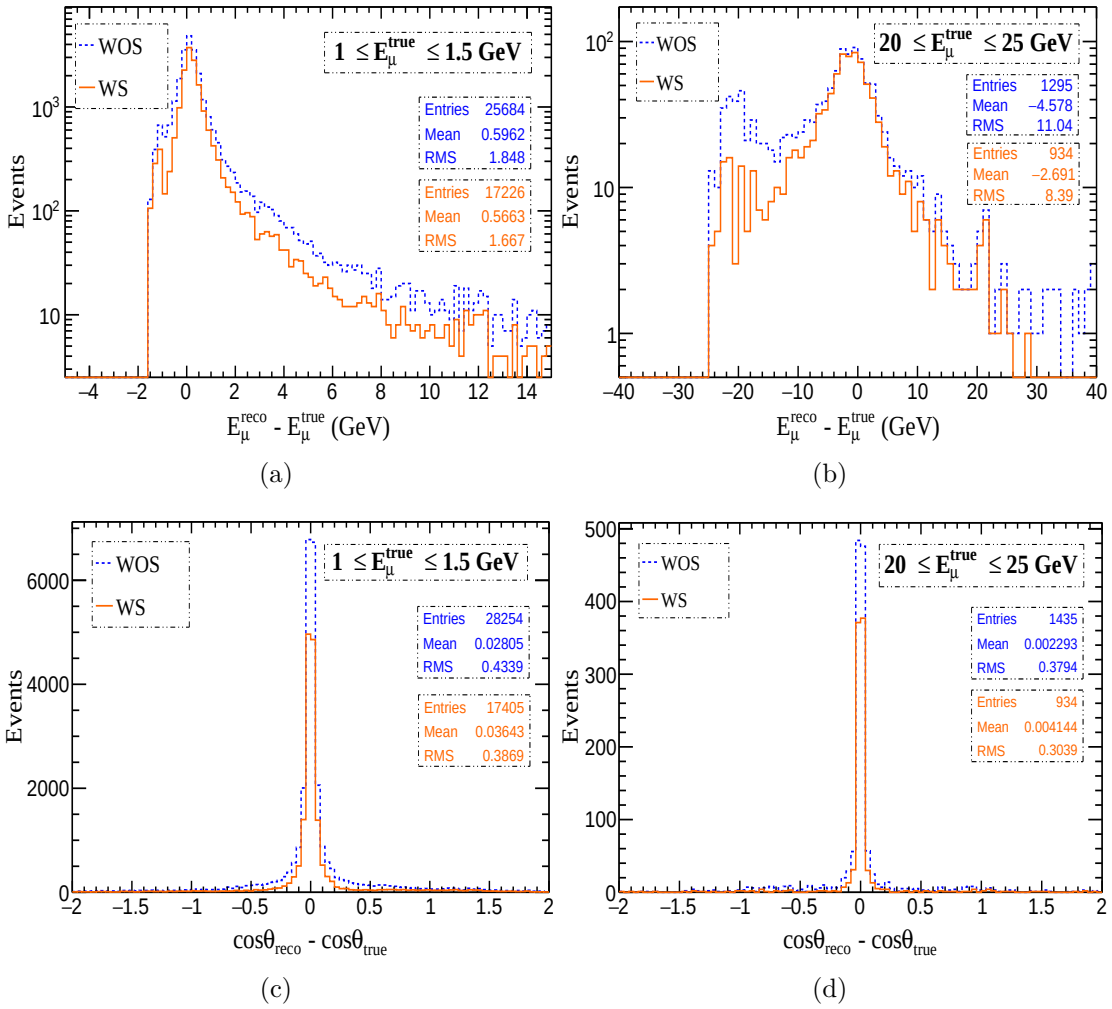

Figure 4.11: Difference in reconstructed and true values of (a) muon energy in the low energy bin $1 \leq E_\mu^{\text{true}} \leq 1.5$ GeV, (b) muon energy in the high energy bin $20 \leq E_\mu^{\text{true}} \leq 25$ GeV, (c) cosine of muon zenith angle in the low energy bin $1 \leq E_\mu^{\text{true}} \leq 1.5$ GeV and (d) cosine of muon zenith angle in the high energy bin $20 \leq E_\mu^{\text{true}} \leq 25$ GeV, is compared with (WS) (solid, orange) and without (WOS) (dashed, blue) selection.

regions, that satisfy the different event selection criteria, is shown in Table 4.3 for different bins in true muon energy.[16] On average, the χ^2 selection (CS) removes $\sim 25\%$ of the reconstructed events, whereas the horizontal event selection (HS), z-vertex selection (ZS), N_{hits} selection (NS) and other selections (OS) remove 6%, 4.6%, 15% and 3.6%, respectively.[17]

The event selection is able to improve the CID efficiencies and resolutions, but a lot of good events are also lost in the process. Note that the N_{hits} selection performs

[16]The number of events in different energy bins are averaged over the zenith and azimuthal angles of the muon.

[17]Note that these percentages are hierarchical, where the event selection criteria CS, HS, ZS, NS and OS are applied in the given order.

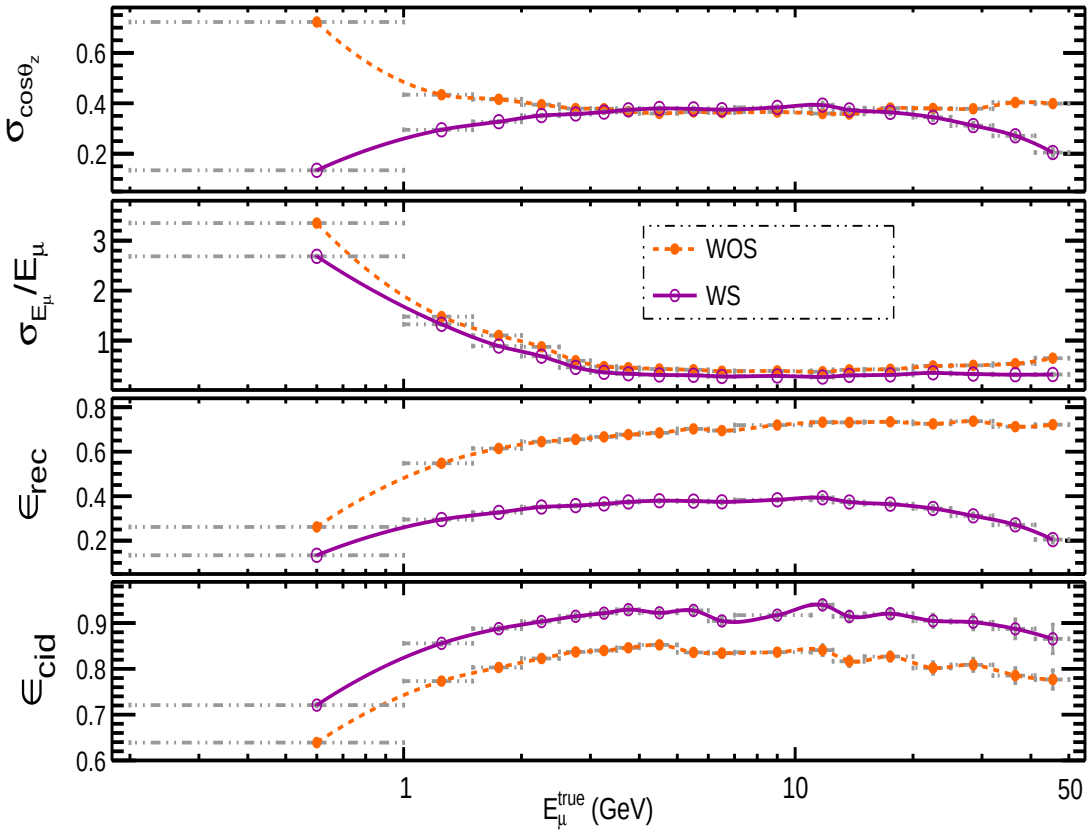

Figure 4.12: Comparison of muon zenith angle resolution (top panel), energy resolution (below top panel), reconstruction efficiency (above bottom panel) and charge identification efficiency (bottom panel), with (WS) and without (WOS) event selection.

well in the side and peripheral regions by identifying the partially contained high energy events that are poorly reconstructed, but at low energies (0.2 - 1.5 GeV) the partially-contained events are completely removed. Figure 4.13 shows the residual distribution of muon energy for the partially contained events that are lost during event selection in side and peripheral regions.

In Fig. 4.13, the energy resolutions are within 5% of the events that are selected, but are lost for the optimal selection. Similarly a lot of better reconstructed events are lost to various event selection criteria applied. Hence in the oscillation analysis discussed in next chapter, we also study the effect of event selection on the parameter determination.

Region	Events	Selection	Percentage of events left in the reconstructed sample (%) E_μ^{true} bin (GeV)																		
			0.2 to 1	1 to 1.5	1.5 to 2	2 to 2.5	2.5 to 3	3 to 3.5	3.5 to 4	4 to 5	5 to 6	6 to 7	7 to 11	11 to 12.5	12.5 to 15	15 to 20	20 to 25	25 to 32	32 to 41	41 to 50	Average
CR	all	CS	74	75	76	79	80	81	84	85	84	86	86	85	84	83	80	76	73	68	77
		CS + HS	72	72	70	71	69	70	72	70	68	68	66	65	62	62	61	54	55	47	70
		CS + HS + ZS	68	68	66	67	66	67	69	67	65	65	63	63	60	60	59	53	54	45	67
		CS + HS + ZS + NS	68	68	66	67	66	67	69	67	65	65	63	63	60	60	59	53	54	45	67
		CS + HS + ZS + NS + OS	54	59	58	60	59	59	61	60	57	58	57	56	52	53	52	45	43	32	57
PR	FC	CS	70	70	70	72	74	75	76	75	79	77	76	78	75	60	60	51	46	45	71
		CS + HS	69	67	65	65	65	64	65	63	63	62	59	57	54	42	40	38	35	28	66
		CS + HS + ZS	67	67	65	65	65	64	64	63	63	61	59	57	53	42	40	38	35	27	65
		CS + HS + ZS + NS	67	67	65	65	65	64	64	63	63	61	59	57	53	42	40	38	35	27	65
		CS + HS + ZS + NS + OS	64	64	62	62	62	61	61	60	60	57	56	55	50	39	34	33	29	20	62
	PC	CS	72	73	74	79	82	85	84	85	85	87	86	85	85	85	83	79	78	70	79
		CS + HS	71	72	71	73	77	76	76	75	75	74	73	71	73	69	68	61	55	53	72
		CS + HS + ZS	59	54	55	59	66	66	67	67	68	68	69	68	71	66	66	59	55	51	62
		CS + HS + ZS + NS	0	3	10	20	28	32	35	40	44	47	51	53	57	56	56	50	48	43	25
		CS + HS + ZS + NS + OS	0	3	10	19	28	31	34	39	43	46	48	50	53	52	51	46	39	28	24
SR	FC	CS	68	72	74	74	76	76	73	84	84	73	80	73	72	71	63	41	54	76	72
		CS + HS	68	69	69	67	67	65	61	72	69	57	59	62	54	54	50	22	23	43	67
		CS + HS + ZS	66	68	69	67	67	65	61	72	69	57	59	62	52	54	50	22	23	43	66
		CS + HS + ZS + NS	66	68	69	67	67	65	61	72	69	57	59	62	52	54	50	22	23	43	66
		CS + HS + ZS + NS + OS	62	64	66	64	63	63	58	68	65	56	55	62	44	51	37	11	23	29	63
	PC	CS	71	73	74	82	83	89	83	84	84	87	89	88	85	88	79	80	79	60	78
		CS + HS	70	71	68	77	78	77	75	76	70	73	75	69	68	71	68	66	66	43	72
		CS + HS + ZS	62	61	56	66	69	71	69	69	63	67	72	65	66	67	68	66	64	43	64
		CS + HS + ZS + NS	0	3	16	29	35	39	40	48	43	48	54	55	56	58	54	60	55	33	25
		CS + HS + ZS + NS + OS	0	3	15	28	34	37	38	46	43	46	53	53	56	56	50	54	47	27	24

Table 4.3: The region wise percentage of the reconstructed sample after each selection criterion, shown in different bins of true muon energy.

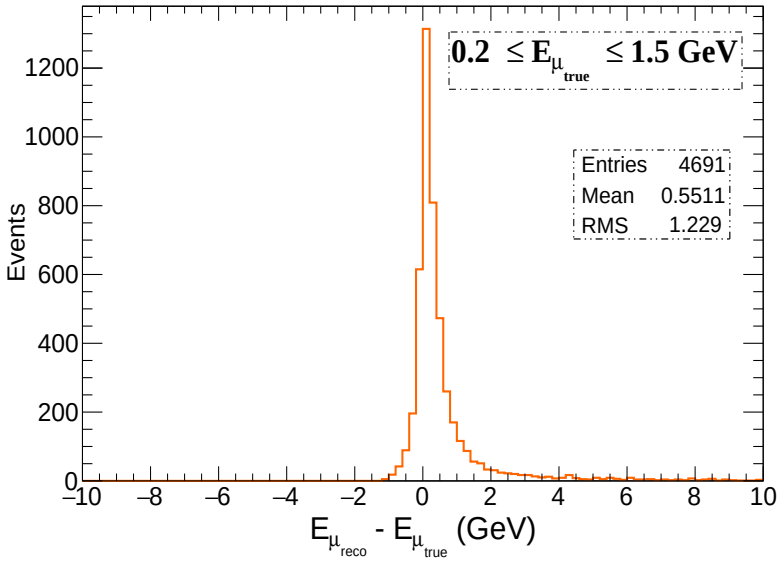

Figure 4.13: Residual distribution of muon energy for the low energy partially-contained events that are lost to event selection.

4.6 Summary

The ability of the ICAL to measure the oscillation parameters, and observe the MH, depends on the extent of ICAL to identify and reconstruct the neutrino events at different energies and directions. Hence a CC ν_μ data for an exposure of 50 kton $\times$ 100 years is simulated to study the response of ICAL in the neutrino energy range 0.2 - 50 GeV. An overall reconstruction of 41%, with a 81% charge identification efficiency is observed.

Various event selection criteria are applied to improve the response of ICAL. The charge identification efficiency increases by $\sim$ 8%, whereas the energy and angular resolutions show a relative improvement of 23% and 19% respectively, but almost 47% of the reconstructed events are lost in the process. Hence the event selection improves the quality of the events, while the quantity of the events reduces considerably.

The reach of ICAL in measuring the oscillation parameters depends on the oscillation sensitivity and the exposure time (event statistics) of ICAL. The qualitative and quantitative effect of the event selection on the oscillation sensitivity, within the framework of low event statistics is studied and discussed in the following chapters.

CHAPTER 5

Oscillation analysis

One of the main goals of the ICAL is to precisely determine the atmospheric neutrino oscillation parameters $\sin^2\theta_{23}$ and Δm^2_{32}, and measure the MH of neutrinos. The present chapter describes the reach of the ICAL in measuring these parameters within the framework of low event statistics. The idealized case, where the NUANCE data is folded with detector efficiencies and smeared by the resolution functions obtained from GEANT-based studies of single muons with fixed direction and energy, has been presented previously [173]. The analysis presented here uses a realistic approach, where an event-by-event reconstruction is performed by simulating each event in a GEANT-based detector environment as described in Chapter 3.

The first step in the analysis procedure is event generation, where a CC ν_μ sample is generated for an exposure of 50 kton $\times$ 1000 years. The generated events are reconstructed event-by-event and the event selection criteria are applied as described in Chapter 4 to remove badly reconstructed events. The selected events are binned after applying event-by-event oscillations, and are used in the χ^2 analysis to determine the oscillation parameters. Each of these procedures is described in detail in the following sections.

5.1 Event generation

The analysis presented in this chapter mainly focuses on the reach of ICAL in measuring the oscillation parameters and the effect of fluctuations that arise from the low event statistics. To impart fluctuations, a NUANCE data file with CC ν_μ events are generated for an exposure of 50 kton$\times$1000 years, where the sub-samples corresponding to five years of data are used as the experimentally simulated sample (pseudo-data set) and the remaining 995 years of data are used to construct the

probability distribution functions (PDFs) that are used in the χ^2 fit. Hence the five-year experimental sample is completely uncorrelated with respect to the PDFs that are used to fit the data.

In the previous studies [173–175] the data were analyzed for an exposure of five or 10 years, but was scaled down from a 1000 year sample. The main purpose of scaling was to reduce the statistical fluctuations arising from the low event statistics. Hence the experimental data were unfluctuated, and as the same sample was used to construct the PDF, the experimental data were also correlated and the reconstructed central value was always practically the same for both. The present analysis will mainly focus on the effects of low event statistics by studying the χ^2 fits to the data samples with and without fluctuations.

The muon events in the ICAL includes the contribution from atmospheric ν_μ and ν_e flux, hence they are generated and reconstructed before applying the oscillations. The general analysis procedure to determine the oscillation parameters with and without fluctuations, is shown using a flowchart in Fig. 5.1. The event-by-event oscillation and the relative flux of oscillated ν_μ and ν_e events are discussed in the next section.

5.2 Applying oscillations

The determination of neutrino oscillation parameters to a high accuracy requires a precise calculation of oscillation probabilities. Numerically, the oscillation probabilities may be computed to a required precision, but the non-uniform Earth matter poses a problem analytically. In the analysis, the oscillations probabilities are calculated very precisely by numerically evolving the neutrino flavor eigenstates [65] using the equation,

$$i\frac{d}{dt}\left[\nu_\alpha\right] = \frac{1}{2E}\left(UM^2U^\dagger + \mathcal{A}\right)\left[\nu_\alpha\right], \tag{5.1}$$

where $[\nu_\alpha]$ denotes the vector of flavor eigenstates, ν_α, with $\alpha = e, \mu, \tau$, and U is the PMNS mixing matrix given by Eq. (1.22). Here, M^2 is the mass-squared matrix with the diagonal piece proportional to m_1^2 removed: $M^2 = \mathrm{diag}(0, \Delta m^2_{21}, \Delta m^2_{31})$,

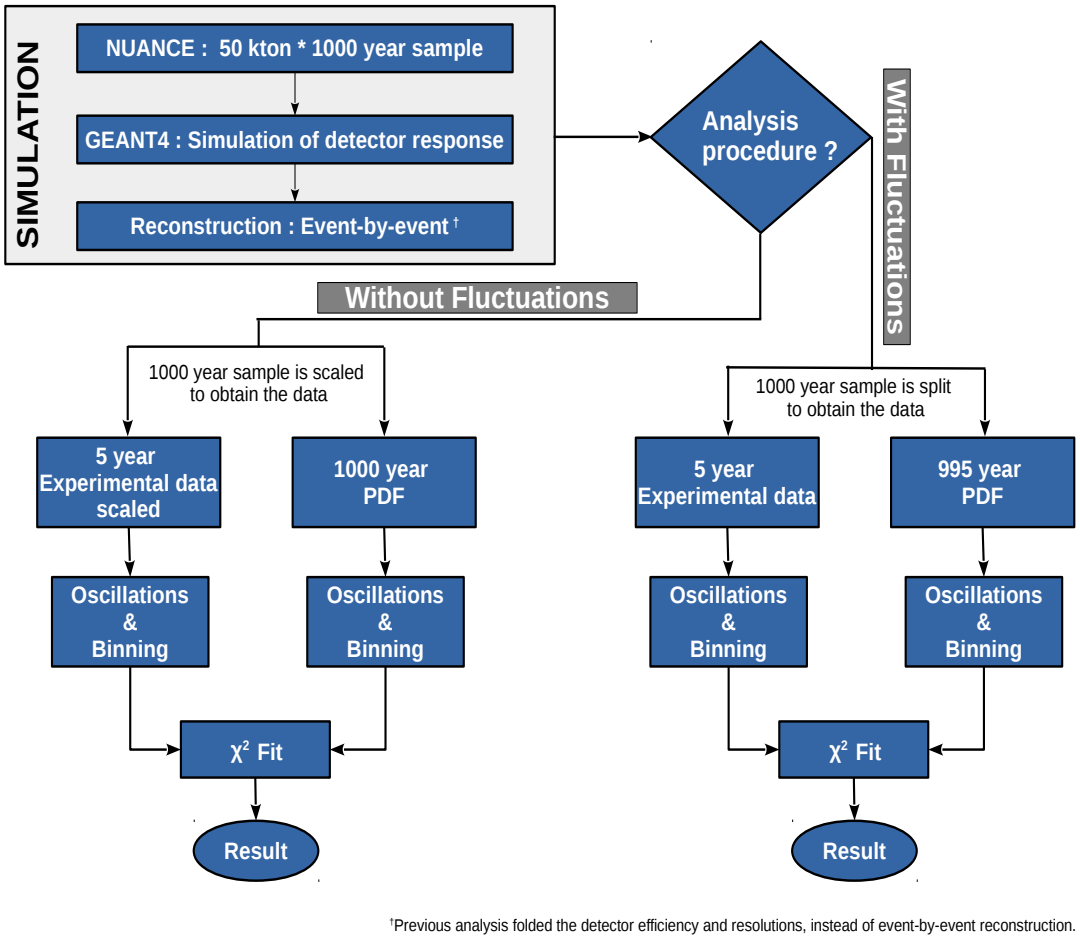

Figure 5.1: Flow chart showing the two different analysis procedures, with and without fluctuations.

and $\mathcal{A}$ is the diagonal matrix, $\mathrm{diag}(A, 0, 0)$, with matter term A given by

$$\begin{aligned} A = & \pm 2\sqrt{2} G_F n_e E \\ = & \pm 7.63 \times 10^{-5}\ \rho E, \end{aligned} \tag{5.2}$$

where the sign is positive for ν and negative for $\bar{\nu}$. Here, E is the neutrino energy in GeV, G_F is the Fermi coupling constant, and n_e is the electron number density, which is related to the matter density ρ in gcm^{-3}. The difference in sign of A for ν and $\bar{\nu}$ leads to differing oscillation probabilities, which in turn are sensitive to the sign of Δm^2_{32}.

The precise calculation of oscillation probabilities depends on the accurate interpretation of the density profile of the Earth. The Earth matter density is not uniform, but it increases progressively as it reaches the center of the Earth. The Preliminary Reference Earth Model (PREM) [66], an average Earth model,

provides the density profile of Earth that is used to calculate the oscillation probabilities [65]. It identifies nine principal regions based on the discontinuities in the Earth's density. The nine concentric shells in Fig. 5.2a shows the schematic representation of those regions (assuming spherical symmetry).

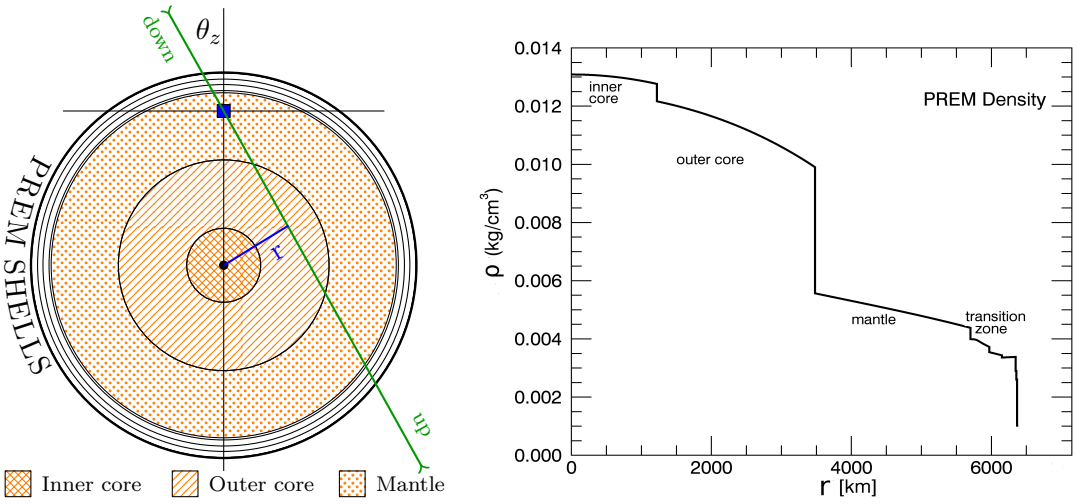

Figure 5.2: (a) Concentric shells showing the schematic of principal regions identified by PREM profile. (b) The variation of radial density of the Earth as given by PREM [176].

Figure 5.2b shows the variation of the Earth's density profile with the distance r (in km) from the center of the Earth, where the density changes abruptly at core-mantle and inner-outer core transitions. Note that the average Earth model does not reflect the actual structure of the Earth in the first few tens of kilometers, as the lateral heterogeneity is very large. Also the absolute values of the densities themselves are not well established, which is known to affect the oscillation probabilities [65]. However, the present analysis only uses the absolute values of the density obtained from the PREM profile, and any uncertainties pertaining to the PREM profile are beyond the scope of this thesis. Inversely in neutrino tomography, the neutrino oscillation physics can be used to probe the internal structure of the Earth [177–179] giving a better understanding of the Earth's density.

The ICAL has an advantage because it can differentiate between ν and $\bar{\nu}$ events and observe the matter effects separately. The muon signal in the ICAL will have contributions from the component of the ν_e flux (Φ_{ν_e}) that has oscillated to ν_μ and the component from ν_μ flux (Φ_{ν_μ}) that has survived.[1] Hence the total number of

[1]The atmospheric ν_τ flux (Φ_{ν_τ}) is estimated to be about 10^6 times lower than Φ_{ν_μ} and

events appearing in the detector for an exposure time T is obtained from

$$\frac{d^2N}{dE_\nu \; d\cos\theta_z} = T \times N_D \times \sigma_{\nu_\mu} \left[P_{\mu\mu} \frac{d^2\Phi_{\nu_\mu}}{dE_\nu \; d\cos\theta_z} + P_{e\mu} \frac{d^2\Phi_{\nu_e}}{dE_\nu \; d\cos\theta_z} \right], \tag{5.3}$$

where N_D is the number of targets in the detector. Here $P_{\mu\mu}$ and $P_{e\mu}$ are the survival ($\nu_\mu \to \nu_\mu$) and transition ($\nu_e \to \nu_\mu$) probabilities for the ν_μ and ν_e channel, respectively.

5.2.1 ν_μ channel

The muon neutrinos are the most abundant component of the atmospheric neutrino in comparison to other neutrino flavors. The ν_μ flux is twice that of ν_e flux, and increases with increasing neutrino energy. A five year pseudo-data set containing CC ν_μ information is generated and reconstructed before applying oscillations, where the effect of event selection is also studied by applying the event selection criterion. The ν_μ survival probabilities are calculated including the Earth matter effects, and the oscillations are applied via the accept or reject method. Here, the true values of the oscillation parameters are used assuming NH, from Ref. [180]; see Table 5.1.

Parameter	Input Value
$\sin^2\theta_{23}$	0.5
$\sin^2\theta_{12}$	0.304
$\sin^2\theta_{13}$	0.0219
Δm^2_{21} (eV^2)	7.53×10^{-5}
Δm^2_{32} (eV^2)	2.32×10^{-3}
δ_{CP}	0

Table 5.1: Assumed values of oscillation parameters [180] used to construct the pseudo-data, where δ_{cp} is assumed to be zero.

Accept or reject method

The accept or reject method decides whether a ν or $\bar{\nu}$ has not oscillated, which is referred to as 'survived', or has oscillated into other neutrino flavors. Initially, the ν_μ survival probability $P_{\mu\mu}$ is calculated for each ν or $\bar{\nu}$ with a given energy and

Φ_{ν_e} [97].

direction. To decide whether an unoscillated ν_μ survives oscillations to be detected as ν_μ, a uniform random number r is generated between 0 and 1. If $P_{\mu\mu} > r$, the event is accepted and is considered to have survived the oscillations. Otherwise, it is considered to have oscillated into another flavor and is rejected. Figures 5.3(a) and 5.3(b) show the zenith angle distribution of muons before and after applying the oscillations for $\bar{\nu}_\mu$ and ν_μ events respectively. They also compare the zenith angle distributions with (WS) and without (WOS) event selection.

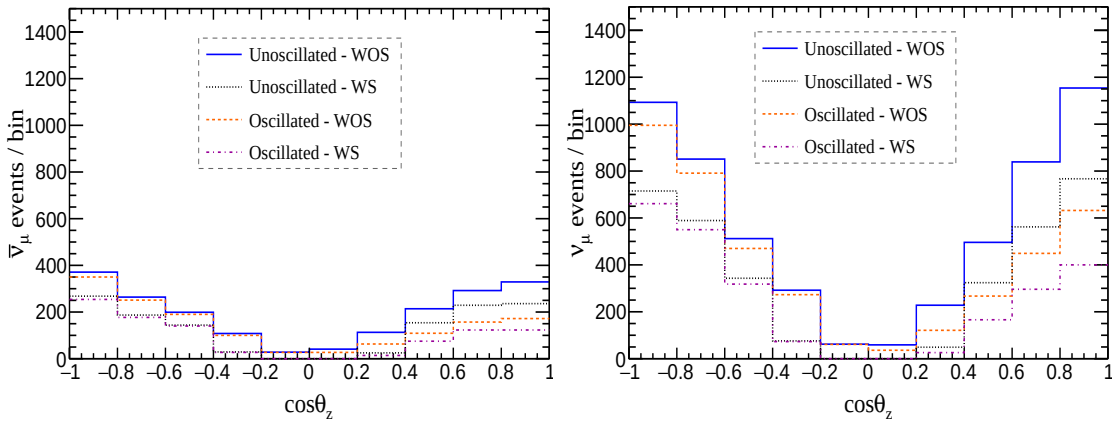

(a) (b)

Figure 5.3: $\cos\theta_z$ distributions with and without oscillations for (a) μ^+ obtained from $\bar{\nu}_\mu$ events. (b) μ^- obtained from ν_μ events. The distributions are also compared with (WS) and without (WOS) selection criterion.

The upward going neutrinos ($\cos\theta_z > 0$) would travel a larger distance compared to downward going neutrinos ($\cos\theta_z < 0$) with a larger probability to oscillate into another flavor, which is evident from the reduction of events in the bins $\cos\theta_z > 0$. Almost 70% of events survive the oscillations. Table 5.2 quotes the total number of ν_μ events which survive the oscillations for a 50 kton × 5 years exposure of Φ_{ν_μ} flux.

Procedure	WOS	WS
Unoscillated	8314 ± 91	5210 ± 72
Oscillated	6103 ± 78	3802 ± 61

Table 5.2: Number of CC ν_μ events, before and after oscillation for a 50 kton × 5 years exposure of Φ_{ν_μ} flux, is shown with (WS) and without (WOS) applying selection criterion.

In Fig. 5.3 the oscillation signatures are different in $\bar{\nu}_\mu$ and ν_μ events, where it depends on the sign of Δm^2_{32}. This difference is solely due to the matter effects,

as we have assumed no CP violation. (It has been clearly established that CC μ events in the ICAL are insensitive to $\delta_{\rm cp}$ [101].) Hence, in the process of binning, the ν_μ events are separated from $\bar{\nu}_\mu$ events to have a maximum sensitivity to the MH.

5.2.2 ν_e channel

The $\nu_e \to \nu_\mu$ transition probability is negligible in comparison to $\nu_\mu \to \nu_\mu$ survival probability. The Figure 5.5 shows the comparison of oscillation probabilities $P_{e\mu}$ and $P_{\mu\mu}$ at different neutrino energies, where $P_{e\mu}$ are relatively smaller at all length scales except when it satisfies the matter resonance condition (the peak at $\log(L/E_\nu) \approx 3.4$ in Fig. 5.4b; see Sec. 1.3.2 for details). Hence the fraction of muon events coming from the ν_e channel will be negligible at ICAL, despite the fact that the atmospheric ν_e flux is almost half that of the atmospheric ν_μ flux.

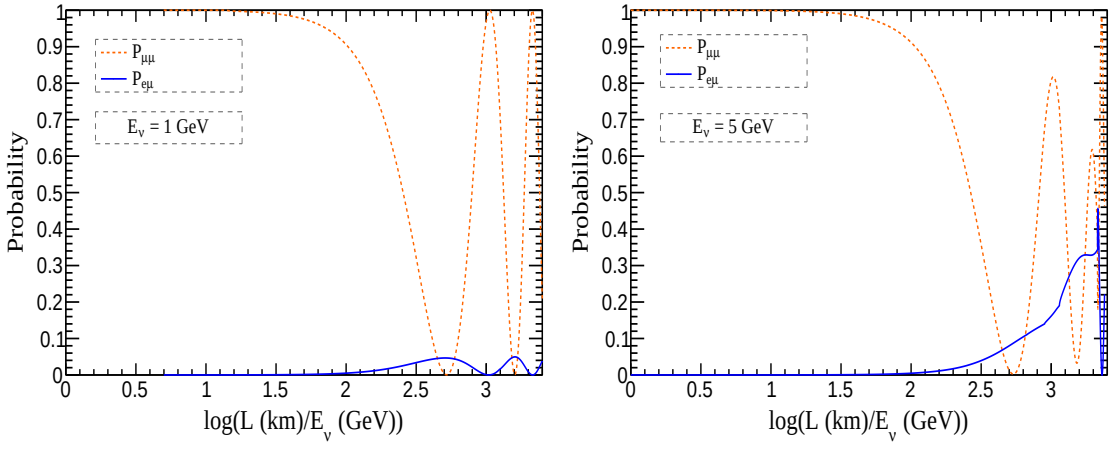

(a) (b)

Figure 5.4: Comparison of oscillation probabilities $P_{e\mu}$ and $P_{\mu\mu}$ at different neutrino energies (a) 1 GeV, and (b) 5 GeV.

The fraction of oscillated ν_e events, *i.e.* the ratio of the number of ν_μ like events coming from the ν_e flux to the total ν_μ like event in the ICAL, is given by,

$$\text{Fraction of } \nu_e = \frac{N_{\nu_e \to \nu_\mu}}{N_{\nu_e \to \nu_\mu} + N_{\nu_\mu \to \nu_\mu}}. \tag{5.4}$$

Figure 5.5 shows the fraction of $\bar{\nu}_e$ and ν_e in the detector for an exposure of

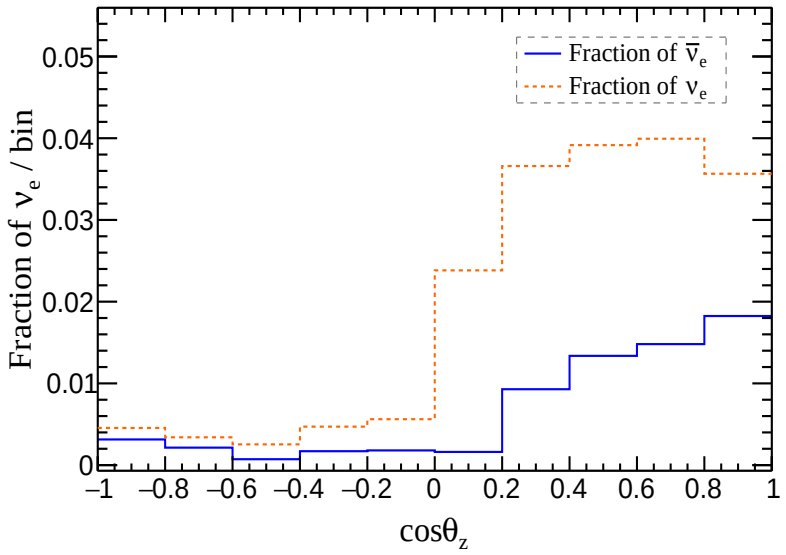

Figure 5.5: Fraction of $\bar{\nu}_e$ in $\bar{\nu}_\mu$, and ν_e in ν_μ sample (50 kton $\times$ 100 years).

50 kton $\times$ 100 years,[2] where it is observed to account for 0.7% and 2% of the total sample respectively. Hence in the present analysis, the contribution from the ν_e channel is neglected. However, the ν_e channel is known to marginally dilute the sensitivity of oscillation parameters, which will be discussed later.

5.3 Binning scheme

The reconstructed muon information from the ν_μ channel are used for binning. During reconstruction, the positive and negative charged particles are conventionally tagged with positive and negative momentum respectively. Hence the muons with negative reconstructed momentum are identified as μ^- from a neutrino event, and the ones with positive momentum are identified as μ^+ from an anti-neutrino event. The information on the reconstructed muons with negative and positive charges are binned separately in $Q_\mu E_\mu$ and $\cos\theta_z$ bins after applying oscillations, where $Q_\mu = \pm 1$ for $\mu^\pm$. Hence the events with negative $Q_\mu E_\mu$ indicate those identified as ν_μ, and the ones with positive $Q_\mu E_\mu$ is identified as $\bar{\nu}_\mu$ events.

Figure 5.6(a) shows the uniform binning in $\cos\theta_z$ from -1 to 1, whereas Fig. 5.6(b) shows the variable binning in $Q_\mu E_\mu$ from -50 GeV to 50 GeV, with and without event selection. As the atmospheric neutrino flux falls rapidly at higher energies, wider bins were chosen to ensure adequate statistics in those energy

[2]The sample size is increased to an exposure of 50 kton $\times$ 100 years to have good statistics.

regions. Table 5.3 summarizes the binning scheme that is used in the current analysis.

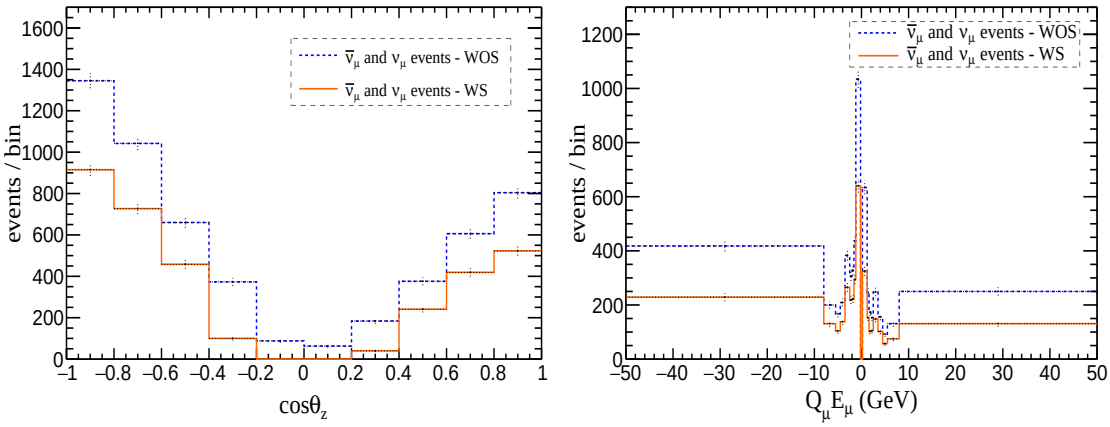

Figure 5.6: (a) Binning in $\cos\theta_z$, and (b) binning in E_μ of five year oscillated pseudo-data. The solid (orange) line and the dashed (blue) line shows the binning with (WS) and without (WOS) event selection cuts.

Observable	Range	Bin width	Bins	Total bins
E_μ (GeV)	[-1.2, -0.2], [0.2, 1.2]	1.0	2	18
	[-2, -1.2], [1.2, 2]	0.4	4	
	[-2.5, -2], [2, 2.5]	0.5	2	
	[-5.5, -2.5], [2.5, 5.5]	1.0	6	
	[-8, -5.5], [5.5, 8]	2.5	2	
	[-50, -8], [8, 50]	42	2	
$\cos\theta_z$	[-1, 1]	0.2	10	10

Table 5.3: The binning scheme for the reconstructed observables $\cos\theta_z$ and E_μ .

The use of finer binning is known to marginally improve the precision in both $\sin^2\theta_{23}$ and $|\Delta m^2_{32}|$, where it has been studied previously [173] for energies less than 11 GeV. Increasing the range of energies beyond 11 GeV is also known to improve the result [174], as the lower part of the L/E spectrum contains more events that are sensitive to oscillations. Also, by increasing the number of high energy bins, the overall precision can be improved. However, it is not feasible due to the limited statistics available within the frame work of low event statistics. The optimization of bin widths at higher energies will be presented in a later section, where the fluctuations are removed to observe the effect of different binning. However, the current analysis will use the binning shown in Table 5.3, to focus on the effects of fluctuations arising from the low event statistics.[3]

[3]The binning shown in Table 5.3 is obtained from the requirement of fit stability, where the

5.4 Constructing the PDF

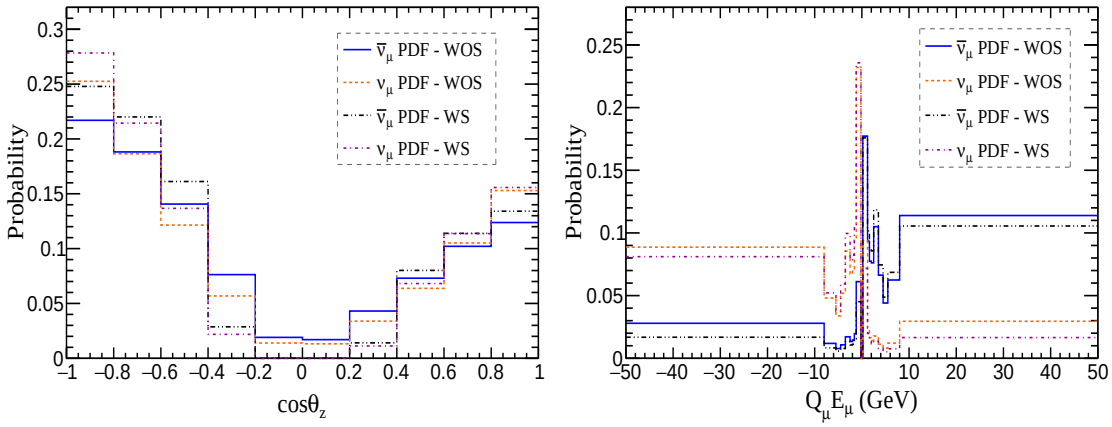

(a) (b)

Figure 5.7: PDF for $\bar{\nu}_\mu$ and ν_μ are shown for (a) binning in $\cos\theta_z$, and (b) binning in E_μ. The $\bar{\nu}_\mu$ (ν_μ) entries for $q_\mu E_\mu < 0$ (> 0) indicate the charge misidentified content. The effect of the event selection is also shown by the distributions with (WS) and without (WOS) event selection criterion.

The probability distribution functions (PDFs) are used to fit the pseudo-data in the chi-square analysis, where separate PDFs are generated for ν_μ and $\bar{\nu}_\mu$ by binning the reconstructed muon information as a function of $\cos\theta_z$ and $Q_\mu E_\mu$. Figures 5.7(a) and 5.7(b) shows the $\bar{\nu}_\mu$ and ν_μ PDFs that are properly normalized for the χ^2 analysis. In the present analysis, two cases exist where the PDFs are created in two different methods.

1. With fluctuations: this is the most realistic case where the data have fluctuations arising from low event statistics. Here the experimental data is split from a larger sample, and the remainder of the sample is used for the construction of the PDF. Hence the PDFs are uncorrelated with respect to the experimental sample.

2. Without fluctuations: this is the ideal case where the fluctuations in the data are removed by scaling a large sample of data. Here the PDFs are generated from the same sample. Hence they are correlated with the experimental data used for the analysis.

fluctuated data sets where subjected to the chi-square fit, and the present binning was chose on the basis of better convergence of the fit.

5.5 The χ^2 analysis and systematics

The χ^2 method is used to fit the pseudodata and determine the atmospheric neutrino oscillation parameters $\sin^2\theta_{23}$ and Δm^2_{32}. The basic ingredients of the χ^2 test include, the theoretical and experimental values of n observables, their uncorrelated errors, and the correlated errors due to k independent sources of systematics. In general, the idea of a χ^2 function is to measure the difference in the theoretical and experimental values in the units of total (theoretical and experimental) uncertainities. In the present analysis, the systematic uncertainties are incorporated via the pull approach [181], which is analytically equivalent to the conventional covariance approach for small uncertainties, and is computationally much faster. After binning the oscillated events, the five year pseudodata set is fit by defining the following χ^2 [173, 182]:

$$\chi^2 = \min_{\{\xi_k\}} \sum_{i=1}^{n_{\cos\theta_z}} \sum_{j=1}^{n_{E_\mu}} 2\left[\left(N_{ij}^{\rm pdf} - N_{ij}^{\rm data}\right) - N_{ij}^{\rm data}\ln\left(\frac{N_{ij}^{\rm pdf}}{N_{ij}^{\rm data}}\right)\right] + \sum_{k=1}^{2}\xi_k^2, \tag{5.5}$$

where, $N_{ij}^{\rm data}$ are the number of events observed and $N_{ij}^{\rm pdf}$ are the number of events that are expected in a given $(\cos\theta_z^i, E_\mu^j)$ bin, while $n_{\cos\theta_z}$ and n_{E_μ} are the total number of $\cos\theta_z$ and E_μ bins respectively, meaning there are $n_{\cos\theta_z} \times n_{E_\mu}$ observables in the fit. Here, $N_{ij}^{\rm data}$ is measured for the true values of oscillation parameters, summarized in Table 5.1, whereas $N_{ij}^{\rm pdf}$ is obtained by combining $\bar{\nu}_\mu$ and ν_μ PDFs as:

$$N_{ij}^{\rm pdf} = R\left[fT_{ij}^{\bar{\nu}} + (1-f)T_{ij}^{\nu}\right]\left[1 + \sum_{k=1}^{2}\pi_{ij}^k\xi_k\right]. \tag{5.6}$$

Here $T_{ij}^{\bar{\nu}}$ and T_{ij}^{ν} are the normalized $\bar{\nu}$ and ν PDFs respectively, with R being the normalization factor in the fit which scales the PDF to the data entries. Also, the free parameter f describes the relative fraction of $\bar{\nu}_\mu$ and ν_μ in the sample. The variables π_{ij}^k and ξ_k are used to incorporate systematic uncertainties, and their definitions are described in Sec. 5.5.1.

5.5.1 Systematics uncertainties

The pull approach parametrizes the systematic uncertainties via a set of variables $\{\xi_k\}$ called pulls, which are then treated on the same basis as the parameters of the fit. The effect of each independent k^{th} source of systematic uncertainty are embeded through a shift of the difference $N_{ij}^{\text{pdf}} - N_{ij}^{\text{data}}$ by an amount $-\pi_{ij}^{k}\xi_k$ in each ij^{th} bin,[4] where the coupling π_{ij}^{k} is the correlated uncertainity related to k^{th} source of systematic. The χ^2 function in Eq. 5.5 can be identified as a sum of two parts [182]:

$$\chi^2(\vec{\zeta},\vec{\xi}) = \chi^2_{\text{data}}(\vec{\zeta},\vec{\xi}) + \chi^2_{\text{pull}}(\vec{\xi}), \tag{5.7}$$

where $\vec{\zeta}$ denotes the parameters of the model,[5] with $\vec{\xi}$ being the systematic pulls. The χ^2_{data} determines the usual difference in the experimental values from the predicted values, whereas the quadratic terms of ξ_k in χ^2_{pull} is added as a proper penalty to account for the deviation of systematic inputs from its nominal value. The value $\xi_k = 0$ corresponds to the expected value, and the variation, $\xi_k = \pm 1$ corresponds to a one standard deviation for the k^{th} source of systematics.

Absolute normalization

The uncertainty in the primary cosmic ray flux and the hadronic models leads to an uncertainty in the atmospheric neutrino flux calculation, which is estimated to be $\sim 20\%$ below 100 GeV [183]. The uncertainty in absolute normalization is estimated to be $\sim 25\%$, where an uncertainty of 15% for the total crossection is added in quadrature with the uncertainity in the flux [184]. Hence, in the previous analysis performed at ICAL, an overall 20% uncertainty in flux normalization was used along with a 10% uncertainty in crossection and 5% on total number of events as the systematics uncertainties [101].[6] However, in the current analysis, R is a free parameter that is used in the fit which fixes the absolute flux normalization, and it is noted to improve the uncertainty in flux normalization.

[4] The negetive sign preceding $\pi_{ij}^{k}\xi_k$ is conventional.

[5] In the present analysis, the fit parameters include $\sin^2\theta_{23}$, Δm^2_{32}, f and R.

[6] Note that the Honda flux at Kamioka site was used for the oscillation analysis at ICAL previously, and the same is used here in the present analysis so as to compare with the previous results.

Antineutrino/neutrino ratio

The uncertainty in π^+/π^- ratio from hadronic calculations results in a systematic uncertainty in the $\bar{\nu}_\mu/\nu_\mu$ ratio, which is estimated to be $\sim 5\%$ [183].[7] The free parameter f in the fit fixes this relative flux normalization.

Energy tilt uncertainty

As discussed in Sec. 1.4.2, the neutrino flux energy spectrum obeys the power function $E_\nu^{-\gamma}$. The uncertainty in the spectral index of the neutrino flux $E_\nu^{\gamma\pm\delta}$ introduces a systematic uncertainty in the energy distribution, which is estimated to be 5% from the primary cosmic ray spectrum [184].

The pull ξ_{tilt} parametrizes the systematic uncertainty in the energy distribution. A standard procedure given in Ref [182] is used to calculate the energy tilt error, *i.e.*, the possible deviation of the energy distribution of the atmospheric fluxes from the power law, by defining

$$\Phi_\delta(E) = \Phi_0(E)(\frac{E}{E_0})^\delta \approx \Phi_0(E)\left[1 + \delta \ln \frac{E}{E_0}\right], \tag{5.8}$$

where $\Phi_0(E)$ is the expected number of events calculated for each $(ij)^{th}$ bin. The quantity $\Phi_\delta(E)$ is computed from Eq. 5.8, where δ is the 1σ tilt error and $E_0 =$ 2 Gev. Note that the fluxes are calculated by neglecting the oscillations, and the coupling π_{ij}^{tilt} is measured from the relative change in the flux.

Zenith angle uncertainty

The uncertainty in the zenith angle induces an error in the up-down asymmetry of the events, and is estimated to be $\sim 5\%$ [182]. The pull ξ_{zenith} parametrizes the systematic uncertainty in the zenith angle distribution, where the coupling in each bin is calculated in proportion to the zenith angle value of that particular bin, *i.e.*, $\pi_{ij}^{\text{zenith}} = 5\% \langle\cos\theta\rangle_{ij}$.[8]

[7] Similarly a 5% systematic uncertainty is estimated for $\bar{\nu}_e/\nu_e$ ratio, but the present analysis only focuses on ν_μ like events.

[8] The average value of $\cos\theta$ in the ij-th bin, *i.e.*, $\langle\cos\theta\rangle_{ij}$, is the central value of the ij^{th} bin.

Hence, a total of two bin-dependent pulls [ξ_{tilt}, ξ_{zenith}] are used to apply the systematics in the present analysis.

5.6 Parameter deduction and selection effects

The χ^2 function in Eq. (5.5) is used to fit the data with and without event selection, and their effects are studied on the sensitivities to neutrino oscillation parameters $\sin^2\theta_{23}$ and Δm^2_{32}. The maximum realistic case, where the data are fluctuated with the usage of low event statistics, and the ideal case, where the effects of fluctuations are negated, are both fit separately to determine the parameters $\sin^2\theta_{23}$ and Δm^2_{32}.

5.6.1 Fit without fluctuations (WOF)

The pseudo-data binned without the fluctuations is fit to determine the parameter $\sin^2\theta_{23}$, marginalizing over Δm^2_{32},[9] for an input value of $\sin^2\theta_{23} = 0.5$ (single parameter fit). Figure 5.8a shows the comparison of $\Delta\chi^2$ with (WS) and without (WOS) event selection as a function of $\sin^2\theta_{23}$. The asymmetrical curve in $\sin^2\theta_{23}$ signifies the breakdown of octant degeneracy, which stems from the leading term $\sin^2 2\theta_{23}$ in the oscillation probability, via the enhanced matter effects due to the relatively large value of θ_{13}.

The observed precision of the parameters are relatively worse after the event selection, as is evident from Figure 5.8. The precision in the parameter determination is defined as

$$\text{precision} = \frac{P_{\text{max}} - P_{\text{min}}}{P_{\text{max}} + P_{\text{min}}}, \tag{5.9}$$

where P_{min} and P_{max} are the minimum and maximum values of the concerned parameter determined at the given C.L.

In Fig. 5.8a, the fit without event selection (WOS) converges to $0.49^{+0.15}_{-0.10}$ in $\sin^2\theta_{23}$ with a 45% precision at 3σ (22.7% at 1σ), whereas the fit with the event selection (WS) converges to $0.50^{+0.14}_{-0.10}$ with a precision of 48% at 3σ (23.4% at

[9] The parameters f and R are the free parameters, hence they are always marginalized in the fit.

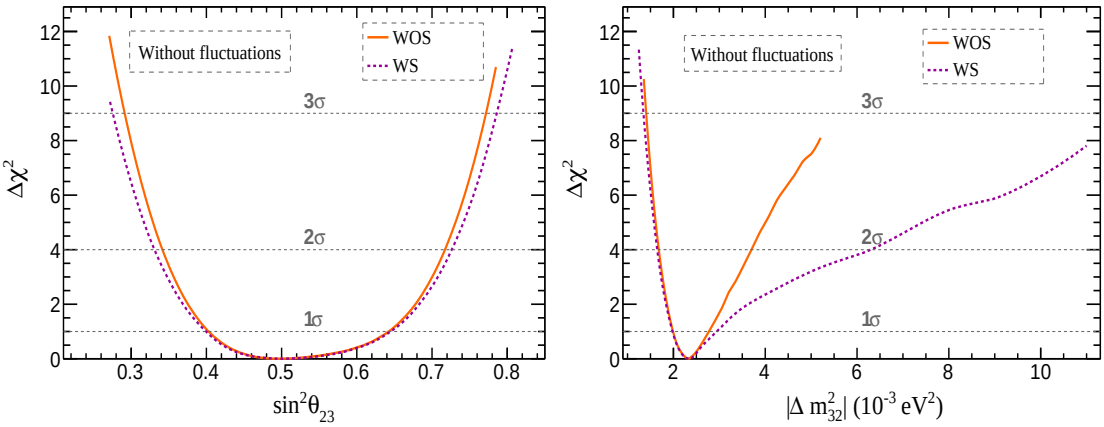

Figure 5.8: $\Delta\chi^2$ as a function of (a)$\sin^2\theta_{23}$, for an input value of $\sin^2\theta_{23}(\text{true}) = 0.5$ and (b) Δm^2_{32}, for an input value of $\Delta m^2_{32}(\text{true}) = 2.32 \times 10^{-3}$ eV^2. The solid (orange) and dashed (magenta) line shows the fit without (WOS) and with (WS) the event selection.

1σ). Therefore, the precision in $\sin^2\theta_{23}$ is only marginally worse after the event selection, whereas the precision in the parameter Δm^2_{32} gets relatively worse.

The Figure 5.8b shows the comparison of $\Delta\chi^2$ with (WS) and without (WOS) event selection as a function of Δm^2_{32}, for an input value of $\Delta m^2_{32} = 2.32\times10^{-3}$ eV^2. The fit without event selection converges to $(2.32^{+0.43}_{-0.32}) \times 10^{-3}$ eV^2 in Δm^2_{32} with a 59.4% precision at 3σ (16.4% at 1σ), whereas the fit with event selection converges to $(2.33^{+0.61}_{-0.36}) \times 10^{-3}$ eV^2 with a precision of 79% at 3σ (19.7% at 1σ). Hence, the precision in Δm^2_{32} is observed to deteriorate by 33% at 3σ.

The parameters $\sin^2\theta_{23}$ and Δm^2_{32} are correlated, and a separate fit (double parameter fit) is performed to obtain the correlated precision reach for the five-year experimental data without fluctuations. An input value of $\sin^2\theta_{23} = 0.5$ and $\Delta m^2_{32} = 2.32 \times 10^{-3}$ eV^2 is used to generate the experimental data set. The parameters in the fit are marginalized as given in Table 5.5, where the relative and absolute scale parameters f and R are always marginalized over the given ranges. The parameters $\sin^2\theta_{13}$ and Δm^2_{21} are kept constant in the fit without any prior constraints, as they have very minimal or negligible effect when marginalized. More details are given in Appendix A.

The two parameter fit converges close to the input value with and without event selection for the unfluctuated data set, see Table 5.5. The fit without event selection converges at $0.49^{+0.15}_{-0.10}$ in $\sin^2\theta_{23}$ and $(2.32^{+0.43}_{-0.32})\times10^{-3}$ eV^2 in Δm^2_{32}, where

Parameter	Marginalization range
$\sin^2\theta_{23}$ [a]	[0,1]
Δm^2_{32} (eV^2) [b]	[0.0005,0.005]
f	[0,1]
R	Unconstrained
$\sin^2\theta_{13}$	Not marginalized
$\sin^2\theta_{12}$	Not marginalized
Δm^2_{21} (eV^2)	Not marginalized
δ_{cp}	Not marginalized

Table 5.4: Marginalization of the parameters as used in the fit

[a]Marginalized when the data is fit to determine Δm^2_{32}
[b]Marginalized when the data is fit to determine $\sin^2\theta_{23}$

as the fit with event selection converges to $0.50^{+0.14}_{-0.10}$ in $\sin^2\theta_{23}$ and $(2.32^{+0.61}_{-0.35}) \times 10^{-3}$ eV^2 in Δm^2_{32} with a larger coverage area. Figure 5.9 compares the precision reach in $\sin^2\theta_{23} - \Delta m^2_{32}$ plane at 99% CL, obtained from the fit to five year pseudo-data set with (WS) and without (WOS) the event selection.

Parameter	Best-fit value WOS	Best-fit value WS
$\sin^2\theta_{23}$	$0.49^{+0.15}_{-0.10}$	$0.50^{+0.14}_{-0.10}$
Δm^2_{32} (eV^2)	$(2.32^{+0.43}_{-0.32}) \times 10^{-3}$	$(2.32^{+0.61}_{-0.35}) \times 10^{-3}$
f	0.26 ± 0.01	0.27 ± 0.01
R	5766 ± 78	3365 ± 60

Table 5.5: Best fit values of the parameters obtained from the fit to five year unfluctuated pseudo-data set for the input values $\sin^2\theta_{23} = 0.5$ and $\Delta m^2_{32} = 2.32 \times 10^{-3}$ eV^2.

The relatively worse precision achieved after the event selection can be attributed to the reduction in the sample size. Note that the sample size was reduced by 42% after selection, which is evident from the absolute normalizations R obtained from both the fits (Table 5.5). The event selection leads to a larger statistical uncertainty in the five year sample, resulting in a worse precision in determining the parameters $\sin^2\theta_{23}$ and Δm^2_{32}. Also it is evident that a fair number of good events are also lost to the selection.

5.6.2 Fit with fluctuations (WF)

The fluctuated experimental-data set corresponding to five years is fit to determine $\sin^2\theta_{23}$, marginalizing over $|\Delta m^2_{32}|$, for an input value of $\sin^2\theta_{23} = 0.5$. Figure

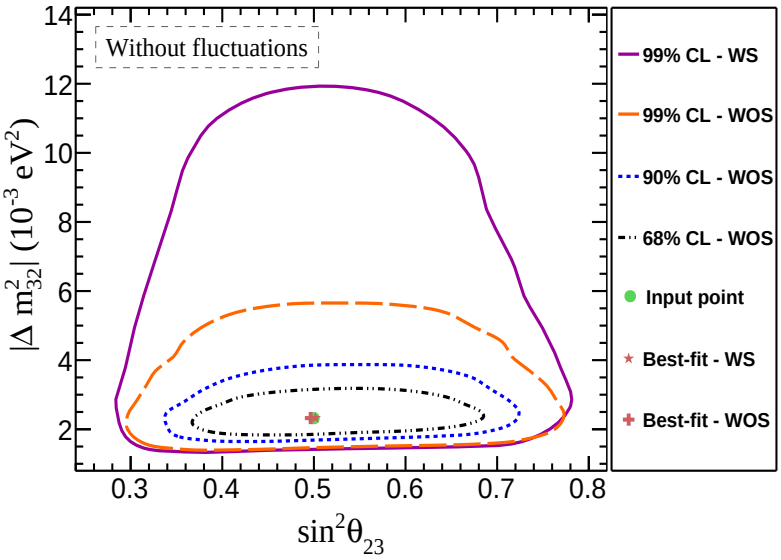

Figure 5.9: Confidence levels obtained in $\sin^2\theta_{23} - \Delta m^2_{32}$ plane from the fit to five year pseudo-data. The broken (black), dotted (blue) and the dashed (orange) line shows the coverage area with 68%, 90% and 99% CL respectively without (WOS) event selection, whereas the solid (magenta) line shows the coverage area with 99% CL with (WS) event selection.

5.10(a) shows the values of $\Delta\chi^2$ as a function of $\sin^2\theta_{23}$, obtained from the fit to data-sets with (WS) and without (WOS) event selection.[10] Unlike the unfluctuated fit, the fluctuated fit converges to a value far away from the input value, where it is quantified by defining the significance of the fit. The significance measures how far the observed value (best fit value) is away from the parameters true value (input value) in the units of $\Delta\chi^2$, *i.e.*,

$$\text{significance} = \sqrt{\Delta\chi^2_{\text{input}} - \Delta\chi^2_{\text{min}}}\ , \tag{5.10}$$

where $\Delta\chi^2_{\text{input}}$ and $\Delta\chi^2_{\text{min}}$ are the $\Delta\chi^2$ values at the true and observed values of the parameter respectively.

The one parameter fit to the fluctuated data converges to a value of $0.58^{+0.06}_{-0.09}$ in $\sin^2\theta_{23}$ without the event selection (WOS), where it is within 1σ of the input value with a significance of 0.86. Note that the fit after event selection converges to $0.67^{+0.06}_{-0.07}$, which is within 2σ of the input value, and shows relatively larger uncertainty at 2 and 3σ range. The observed precision in $\sin^2\theta_{23}$ at 3σ is about 39.2% before applying the event selection, and as expected it deteriorates to 41.9%

[10] Note that the fits with event selection is observed to give a worse result in parameter precision for the unfluctuated data set, but its also worth looking at those effects in the fluctuated data-sets.

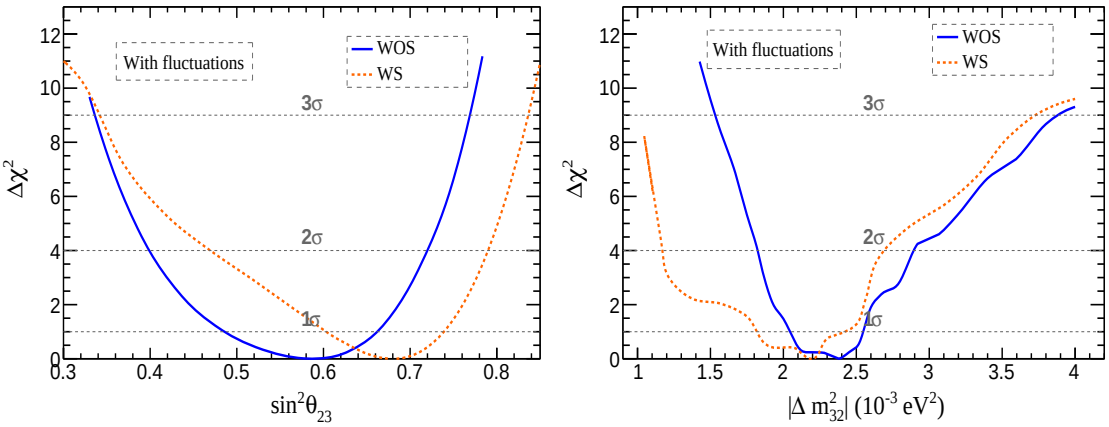

Figure 5.10: $\Delta\chi^2$ as a function of (a) $\sin^2\theta_{23}$, for an input value of $\sin^2\theta_{23}(\text{true}) = 0.5$ and (b) Δm^2_{32}, for an input value of $\Delta m^2_{32}(\text{true}) = 2.32 \times 10^{-3}$ eV^2. The solid (blue) and dashed (orange) line shows the fit without (WOS) and with (WS) event selection.

after applying the selection. Note the improvement in precision by $\sim$ 33% at 1σ for the fluctuated data set, which is mere fluctuations in the outcome of the precision measurement (for this particular fluctuated data-set) in comparison to the unfluctuated data set.

The fluctuated data-set is also fit to determine $|\Delta m^2_{32}|$, marginalizing over $\sin^2\theta_{23}$, for an input value of $\Delta m^2_{32} = 2.32 \times 10^{-3}$ eV^2. A similar behavior is observed in Δm^2_{32}, where Fig. 5.10(b) shows the comparison of $\Delta\chi^2$ with and without event selection as a function of $|\Delta m^2_{32}|$. The fit without event selection converges to a value of $(2.38^{+0.11}_{-0.39}) \times 10^{-3}$ eV^2, where it is within 1σ of the input value with a significance of 0.51. Note that the fit with event selection converges to $(2.18^{+0.23}_{-0.37}) \times 10^{-3}$ eV^2 (within 1σ of the input value), and shows a relatively larger uncertainty at 2 and 3σ range.

The observed $|\Delta m^2_{32}|$ precision for the fit without event selection is 43.4% at 3σ (10.8% at 1σ), whereas after event selection it deteriorates to 57.9% at 3σ (13.9% at 1σ) as expected. Note that the multiple local minimas in $\Delta\chi^2$ function (Fig. 5.10(b)) arises from the statistical uncertainty on the PDF, and a fit to the PDFs constructed from larger MC samples is observed to reduce these local minimas. The details are presented in Appendix B.

The correlated precision reach for the fluctuated data set is obtained from the two parameter fit, where the marginalization of the parameters is performed as

Parameter	Best-fit value WOS	Best-fit value WS
$\sin^2\theta_{23}$	$0.58^{+0.06}_{-0.09}$	$0.67^{+0.06}_{-0.07}$
Δm^2_{32} (eV^2)	$(2.38^{+0.11}_{-0.39}) \times 10^{-3}$	$(2.18^{+0.23}_{-0.37}) \times 10^{-3}$
f	0.26 ± 0.01	0.27 ± 0.01
R	5901 ± 79	3628 ± 62

Table 5.6: Best fit values of the parameters from the fit to five year experimental-data without (WOS) and with (WOS) event selection, for the input values $\sin^2\theta_{23} = 0.5$ and $\Delta m^2_{32} = 2.32 \times 10^{-3}$ eV^2

in Table. 5.5. The parameters in the fit are observed to converge far away from the input value. The fit without event selection converges at $0.58^{+0.06}_{-0.09}$ in $\sin^2\theta_{23}$ and $(2.38^{+0.11}_{-0.39}) \times 10^{-3}$ eV^2 in Δm^2_{32} within a significance of 1σ from the input value, whereas the fit with event selection converges to $0.67^{+0.06}_{-0.07}$ in $\sin^2\theta_{23}$ and $(2.18^{+0.23}_{-0.37}) \times 10^{-3}$ eV^2 in Δm^2_{32} with a significance of 2σ. The best-fit values and the 1σ asymmetrical errors of the parameters are summarized in Table 5.6.

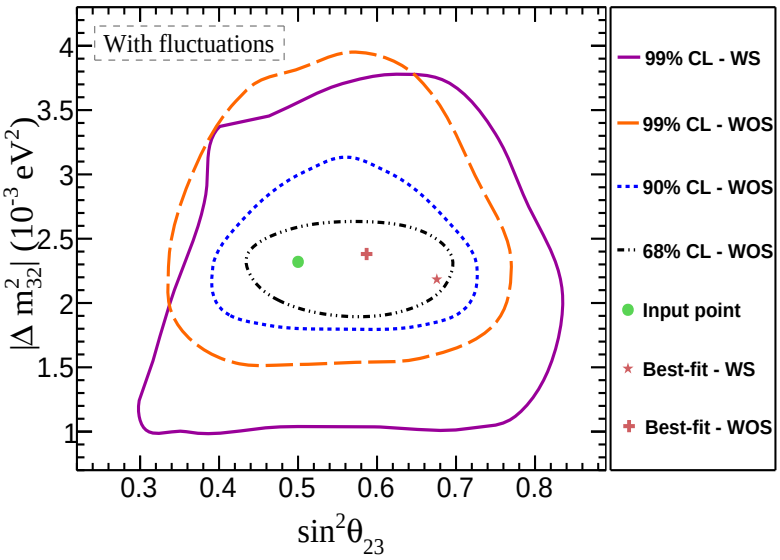

Figure 5.11: Confidence levels obtained from the fit to five year experimental-data in $\sin^2\theta_{23} - \Delta m^2_{32}$ plane within the framework of low event statistics (fluctuated). The broken (black), dotted (blue) and the dashed (orange) line shows the coverage area with 68%, 90% and 99% CL respectively without (WOS) event selection, whereas the solid (magenta) line shows the coverage area with 99% CL with (WS) event selection.

Figure 5.11 compares the precision reach in $\sin^2\theta_{23} - \Delta m^2_{32}$ plane at 99% CL, obtained from the fit to five year fluctuated pseudo-data set with (WS) and without (WOS) the event selection. The fit with event selection shows larger coverage area as expected. The fit was repeated for few other fluctuated data sets, where all observed larger precision for the fit with event selection. Hence in the further

studies, the event selection is ignored and all the events that are reconstructed are taken in to account.

5.7 Effect of fluctuations

The process of scaling nullifies the effect of fluctuations arising from the low event statistics, and the resultant best-fit parameter values are always close to the input values. Hence the parameter sensitivities obtained from the unfluctuated data can be understood as a median sensitivity when averaged over a large number of randomly generated samples. This section explores the possible deviations of the parameter sensitivity and the best fit values that the ICAL can measure with the realistic data.

In order to see the effect of fluctuations, an ensemble of 60 mutually independent fluctuated sets are generated for an exposure of five years. Each set is individually fit to determine $\sin^2\theta_{23}$ and Δm^2_{32}, where both separate (one parameter) and simultaneous (two parameter) fits are performed as mentioned in Sec. 5.6.[11] Figures 5.12a and 5.12b show the one parameter fit to $\sin^2\theta_{23}$ and Δm^2_{32} respectively, and compares the effect of fluctuations in determining them. Note that only three fits (among 60) with fluctuations (WF:1, WF: 2 and WF: 3) are represented from the three independent fluctuated data sets for the comparison.

The parameter uncertainty and hence the precision changes with each fluctuated set, where few are observed to be better, and few to be worse than the precision obtained from the fit to unfluctuated data-set. Note that the asymmetrical uncertainty in $\sin^2\theta_{23}$ has a better precision in the lower octant for the unfluctuated set, whereas the fluctuated data-sets observe fluctuations in the octant sensitivity as well. The effect of fluctuations on the confidence levels obtained in $\sin^2\theta_{23} - \Delta m^2_{32}$ plane is shown in Fig. 5.13 at 99% CL.

The fluctuations in the data induce fluctuations in the resultant best-fit point and the coverage area obtained from the fit. The significance of the convergence also changes along with the resultant of each independent fluctuated pseudo-data

[11] Note that the event selection process is ignored to achieve, and compare, the best possible parameter sensitivities.

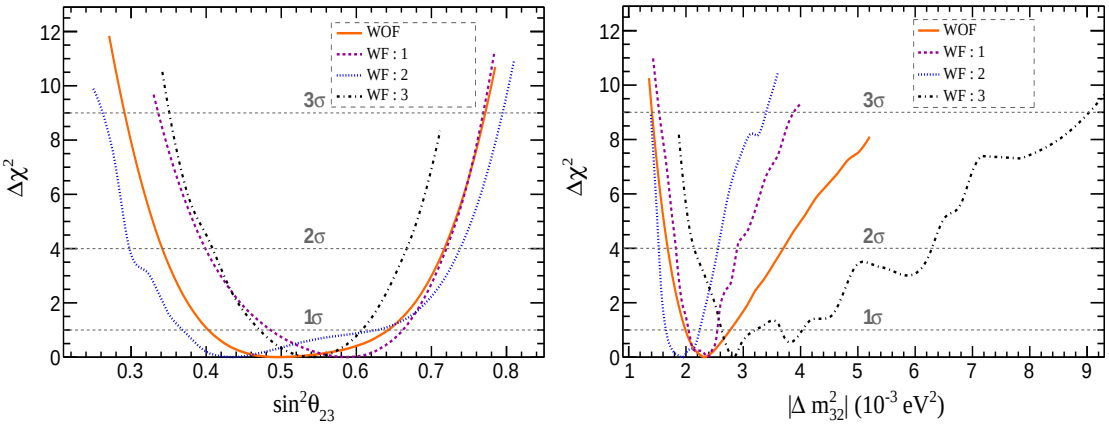

(a) (b)

Figure 5.12: Single parameter fits showing the effect of fluctuations on $\Delta\chi^2$ as a function of (a) $\sin^2\theta_{23}$, for an input value of $\sin^2\theta_{23}(\text{true}) = 0.5$ and (b) Δm^2_{32}, for an input value of $\Delta m^2_{32}(\text{true}) = 2.32 \times 10^{-3}$ eV^2 . The fit to data without (WOF) fluctuations is shown by solid (orange) curve, where it is compared to the fit to three other independent fluctuated pseudo-data sets [WF: 1 (dashed, blue), WF: 2 (dotted, black) and WF: 3 (broken magenta)].

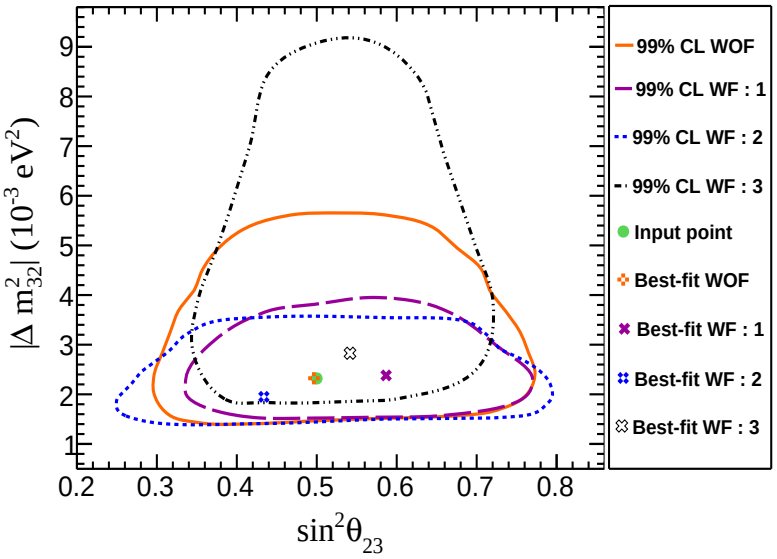

Figure 5.13: Comparison of precision reach in $\sin^2\theta_{23} - \Delta m^2_{32}$ plane obtained from the fit to five year pseudo-data with (WF) and without (WOS) fluctuation. The solid (orange) line shows the coverage area with 99% CL without fluctuations and is compared to the fit to three other independent fluctuated pseudo-data sets [WF: 1 (dashed, magenta), WF: 2 (dotted, blue) and WF: 3 (broken, black)]. The green dot signifies the input (true) value.

set. Any bias in the experimental setup or the analysis procedure can be identified from the significance measured from an ensemble of experiments. Therefore, the significance is measured from an ensemble of 60 experiments by performing separate (single parameter) and simultaneous (double parameter) fits to $\sin^2\theta_{23}$ and Δm^2_{32}.

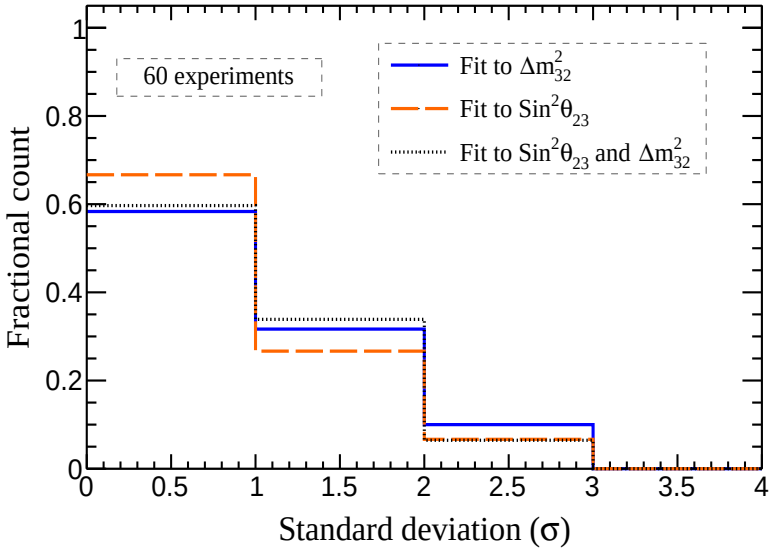

Figure 5.14: The significance of convergence obtained from the fit to 60 independent fluctuated data sets. The significance obtained from the single parameter fit to $\sin^2\theta_{23}$ and Δm^2_{32} is represented by the solid (blue) and broken (orange) lines respectively, whereas the dotted (black) line represents the significance obtained for the simultaneous (double parameter) fit to $\sin^2\theta_{23}$ and Δm^2_{32}.

Figure 5.14 shows the significance of convergence in terms of standard deviation σ. Almost 68% of the times, the fit to $\sin^2\theta_{23}$ converges within 1σ of the input value $\sin^2\theta_{23} = 0.5$. A similar trend is observed in the fit to Δm^2_{32}, where 59% of times it converges within 1σ of the input value $\Delta m^2_{32} = 2.32 \times 10^{-3}$ eV^2. The simultaneous fit to $\sin^2\theta_{23}$ and Δm^2_{32} is also observed to show a similar behaviour in significance. About 95% of the fits converge within 2σ and the rest ($\sim$ 5%) lie outside 2σ. This evidently shows the Gaussian nature of the fit, and confirms that there are no biases in the experiment or analysis procedure. Secondly, it also shows the range of best-fit values that is feasible for a five year run of ICAL.

Averaging

Fluctuations arising from the low event statistics lead to fluctuations in the coverage that is measured from the simultaneous fit to $\sin^2\theta_{23}$ and Δm^2_{32} (Fig. 5.13). In order to obtain an average 99% CL coverage from an ensemble of 50 experiments, the asymmetrical widths $\pm\delta_m$ and $\pm\delta_\theta$ corresponding to the 99% CL are calculated for each set, where they are measured from the best-fit point of that particular set as shown in Fig. 5.15a.

The asymmetrical width $+\delta_m$ measured from different sets is observed to have

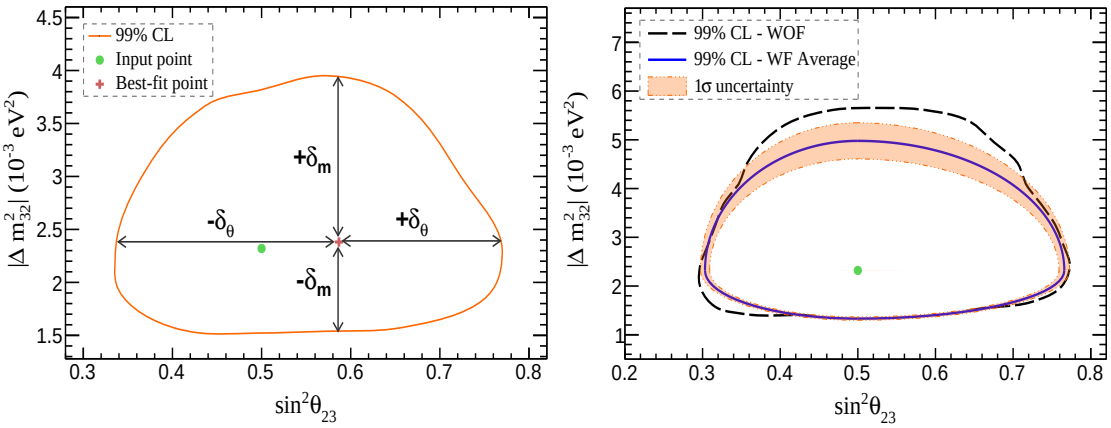

(a) (b)

Figure 5.15: (a) Graphical representation of the asymmetrical widths $\pm\delta_m$ and $\pm\delta_\theta$ calculated at 99% CL (b) Comparison of the average coverage area calculated in $\sin^2\theta_{23} - \Delta m^2_{32}$ plane with the precision reach measured for the unfluctuated data-set at 99% CL. The solid (blue) and dashed (black) line shows the average coverage area and the unfluctuated precision reach respectively. The 1σ uncertainty in the average coverage is shown by the orange band, whereas the dot (green) signifies the input point.

larger variance ($\sim$ 11 times) than the $-\delta_m$ measurements, whereas the widths $\pm\delta_\theta$ is found to have negligible variation. Figure 5.15b shows the average coverage area with 99% CL in the $\sin^2\theta_{23} - \Delta m^2_{32}$ plane, obtained by averaging the asymmetrical widths from simultaneous fit to 50 different pseudo-data sets. The orange band signifies the 1σ uncertainty in calculating the average of the asymmetrical widths. Note that the precision reach for the fit without fluctuations is within 1σ of the average coverage area calculated.

5.8 Mass hierarchy determination

One of the main aims of ICAL is to measure the MH, by separately observing the matter effects in neutrino and antineutrino oscillations. In order to measure the mass hierarchy, a five year pseudodata set is generated and oscillations are applied via the accept or reject method assuming NH (IH). Then the data are fit to true NH (IH) and false IH (NH) PDFs, where the parameters in the fit are marginalized as given in Table 5.5. The $\Delta\chi^2$ resolution to identify and differentiate the correct hierarchy from the wrong hierarchy is defined as:

$$\Delta\chi^2_{\text{MH}} = \chi^2_{\text{false}} - \chi^2_{\text{true}} \ , \tag{5.11}$$

where χ^2_{false} and χ^2_{true} are the minimum χ^2 values obtained from the false and true fits respectively.

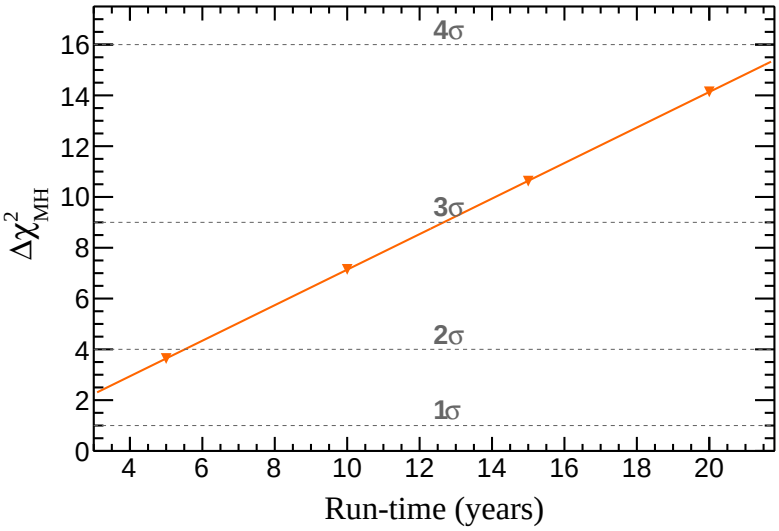

Figure 5.16: $\Delta\chi^2_{\text{MH}}$ as a function of the detector run time in years of data taking.

Figure. 5.16 shows the $\Delta\chi^2_{\text{MH}}$ resolution as a function of the detector run-time, where the fluctuations within the experimental-data are minimized by scaling the data sample. A five year run of 50 kton ICAL rules out the wrong hierarchy with a significance greater than 1σ ($\Delta\chi^2_{\text{MH}} \approx 3.5$), whereas by 10 years of operation the significance improves beyond 2σ ($\Delta\chi^2_{\text{MH}} \approx 7.1$). Around 13 years exposure of the detector, gives a 3σ significance to rule out the wrong MH.

5.8.1 Effect of fluctuations on MH

Fluctuations in the data can lead to fluctuations in the MH determination. In order to see the effect, a five-year fluctuated data set is fit with true and false MH, where the Fig. 5.17(a) shows the variation in $\Delta\chi^2$ from true and false fits as a function of $\sin^2\theta_{23}$. A resolution of $\Delta\chi^2_{\text{MH}} = 7.2$ rules out the wrong hierarchy with a significance greater than 2σ for this particular set (a mere fluctuation), which is about double the resolution obtained from an unfluctuated set for the same exposure time.

Hence, the procedure was repeated for 60 independent five-year fluctuated data sets to see the range of possible values in $\Delta\chi^2_{\text{MH}}$ arising from the fluctuations. The Figure 5.17(b) shows the $\Delta\chi^2_{\text{MH}}$ distribution obtained from the fit to 60 independent fluctuated data sets. A large variation in $\Delta\chi^2_{\text{MH}}$ is observed due

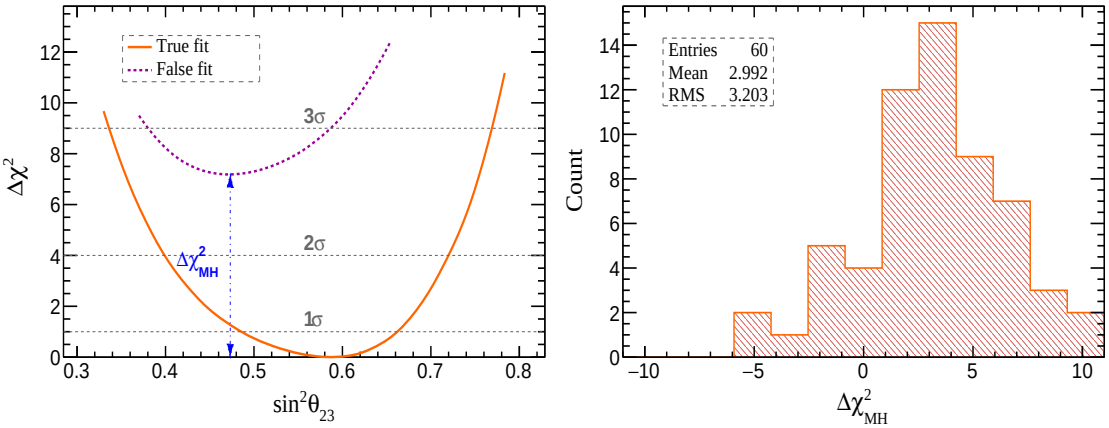

(a) (b)

Figure 5.17: (a) Comparison of $\Delta\chi^2$ variation from true and false fit as a function of $\sin^2\theta_{23}$ and (b) Distribution of $\Delta\chi^2_{\text{MH}}$ resolutions obtained from the fit to sixty independent fluctuated data sets.

to the fluctuation in the data, where the negative and positive values signifies the identification of the wrong and correct MH respectively. The mean resolution of $\Delta\chi^2_{\text{MH}} = 2.9$ rules out the wrong hierarchy with a significance of $\approx 1.7\sigma$ for a five year run of 50 kton ICAL detector. Note that the fit without fluctuations (in Fig. 5.17a) gave a value $\Delta\chi^2_{\text{MH}} \approx 3.5$ which is compatible with the observed mean value.

5.9 Optimizing the binning scheme

The observed events in the detector are binned in the reconstructed variables $\cos\theta_z$ and $Q_\mu E_\mu$, where the number and size of the bins used in the fit affects the precision that is achieved.[12] This section focuses on the bin optimization by ignoring the fluctuations within the data. Hence the data are generated and scaled to five years to remove the fluctuations, and fit using different binning schemes. Table 5.7 lists the five different binning schemes (B1, B2, B3, B4 and B5) used to optimize the fit.

The binning scheme B1 is the default binning used in the analysis, where the events from 0.2 - 50 GeV are binned in 18 energy bins of variable width and 10

[12]Note that the default binning scheme used in the analysis was based on finding stability for the low statistics fits, where larger bins were used in the higher energies because of the low event statistics.

Binning	Observable	Range	Bin width	Bins	Total bins
B1	E_μ (GeV)	[-1.2, -0.2], [0.2, 1.2]	1.0	2	18
		[-2, -1.2], [1.2, 2]	0.4	4	
		[-2.5, -2], [2, 2.5]	0.5	2	
		[-5.5, -2.5], [2.5, 5.5]	1.0	6	
		[-8, -5.5], [5.5, 8]	2.5	2	
		[-50, -8], [8, 50]	42	2	
	$\cos\theta_z$	[-1, 1]	0.2	10	10
B2	E_μ (GeV)	[-1.2, -0.2], [0.2, 1.2]	1.0	2	22
		[-2, -1.2], [1.2, 2]	0.4	4	
		[-2.5, -2], [2, 2.5]	0.5	2	
		[-5.5, -2.5], [2.5, 5.5]	1.0	6	
		[-8, -5.5], [5.5, 8]	2.5	2	
		[-15, -8], [8, 15]	7	2	
		[-25, -15], [15, 25]	10	2	
		[-50, -25], [25, 50]	25	2	
	$\cos\theta_z$	[-1, 1]	0.2	10	10
B3	E_μ (GeV)	[-1.2, -0.2], [0.2, 1.2]	1.0	2	22
		[-2, -1.2], [1.2, 2]	0.4	4	
		[-2.5, -2], [2, 2.5]	0.5	2	
		[-5.5, -2.5], [2.5, 5.5]	1.0	6	
		[-8, -5.5], [5.5, 8]	2.5	2	
		[-15, -8], [8, 15]	7	2	
		[-25, -15], [15, 25]	10	2	
		[-50, -25], [25, 50]	25	2	
	$\cos\theta_z$	[-1, -0.4]	0.05	12	21
		[-0.4, 0]	0.1	4	
		[0, 1]	0.2	5	
B4	E_μ (GeV)	[-1, -0.2], [0.2, 1]	0.8	2	30
		[-4, -1], [1, 4]	0.5	12	
		[-7, -4], [4, 7]	1	6	
		[-11, -7], [7, 11]	4.0	2	
		[-12.5, -11], [11, 12.5]	1.5	2	
		[-15, -12.5], [12.5, 15]	2.5	2	
		[-25, -15], [15, 25]	5	4	
	$\cos\theta_z$	[-1, -0.4]	0.05	12	21
		[-0.4, 0]	0.1	4	
		[0, 1]	0.2	5	
B5	E_μ (GeV)	[-1, -0.2], [0.2, 1]	0.8	2	30
		[-4, -1], [1, 4]	0.5	12	
		[-7, -4], [4, 7]	1	6	
		[-11, -7], [7, 11]	4.0	2	
	$\cos\theta_z$	[-1, -0.4]	0.05	12	21
		[-0.4, 0]	0.1	4	
		[0, 1]	0.2	5	

Table 5.7: The binning scheme for the reconstructed observables $\cos\theta_z$ and E_μ

.

$\cos\theta_z$ bins of uniform bin width. The binning scheme B2 increases the number of energy bins by using finer bins at higher energy, while the number of $\cos\theta_z$ bins are kept same as B1. The binning scheme B3 keeps the binning in energy same as B2, but uses a finer binning in $\cos\theta_z$ for the down going events. Previous studies have used the binning B4 [174] and B5 [101], where the binning configuration is same as B3, but have only considered the events with energies less than 25 GeV and 11 GeV respectively.

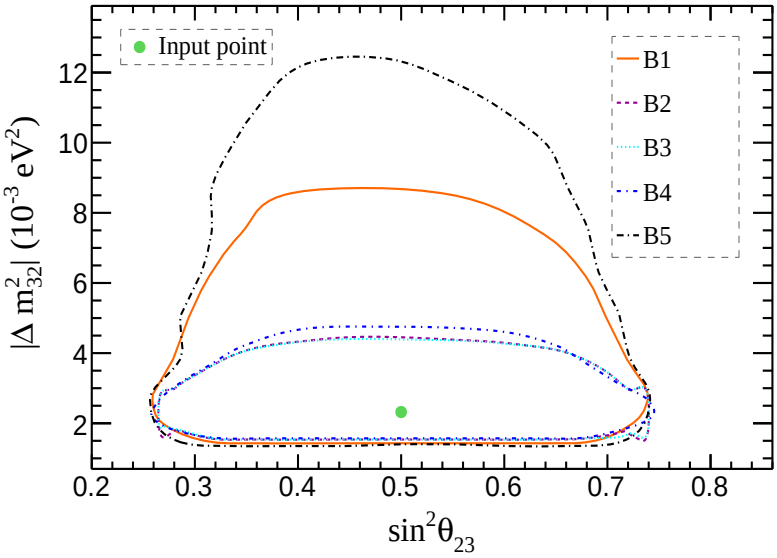

Figure 5.18: Comparison of precision reach obtained from the fit to five year pseudodata in the $\sin^2\theta_{23} - |\Delta m^2_{32}|$ plane for different binning schemes. The input (true) point is given by the green dot.

Figure 5.18 shows the confidence levels obtained in the $\sin^2\theta_{23} - |\Delta m^2_{32}|$ plane for different binning schemes.[13] Increasing the bins in the high energy region improves the precision in $|\Delta m^2_{32}|$, but the precision in $\sin^2\theta_{23}$ remains the same. Also, increasing the number of bins in $\cos\theta_z$ does not affect the precision in $\sin^2\theta_{23}$ and $|\Delta m^2_{32}|$. Hence, the binning scheme B2 and B3 performs equally and better than the rest of the configurations as they have finer binning in $Q_\mu E_\mu$. The binning B4 performs better than B1 and B2 due to finer energy bins, but lacks information on the events greater than 25 GeV. Hence they are marginally worse in Δm^2_{32} in comparison to B2 and B3.

[13]Note that both ν_μ and ν_e fluxes are used, and vacuum oscillations are applied to optimize the binning scheme to reduce the computational time. Hence we also have a notable difference in coverage area obtained for the binning scheme B1 in Fig. 5.18 and 5.15b.

5.9.1 Effect of electron flux

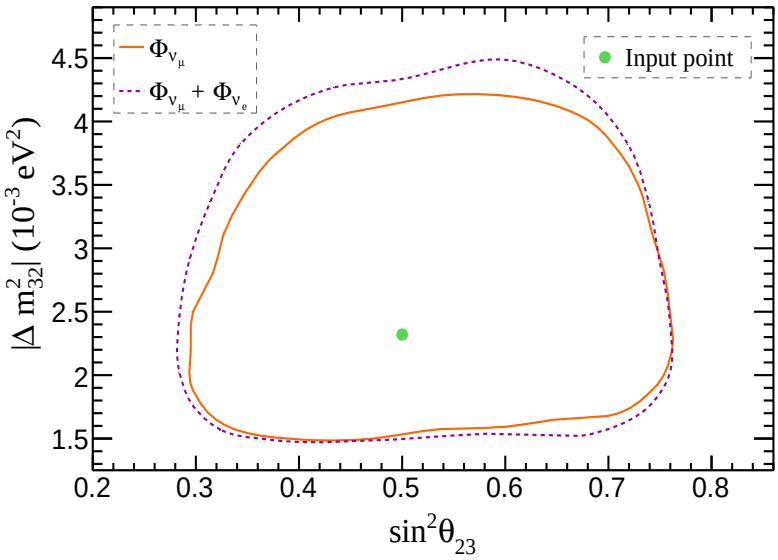

Figure 5.19: Comparison of confidence levels obtained in $\sin^2\theta_{23} - |\Delta m^2_{32}|$ plane with and without the electron flux (Φ_e). The solid (orange) and the dashed (purple) line shows the coverage area with and without Φ_e respectively. The input (true) point is given by the green dot.

The optimized binning B2 is used to see the effect of addition of electron neutrino flux Φ_{ν_e} to the fit along with the muon neutrino Φ_{ν_μ} flux. Note that the electron flux is almost half of the muon flux (discussed in Secs. 1.4.2 & 5.2.2), but the transition probabilities $P(\nu_e \rightarrow \nu_\mu)$ are negligible. The unfluctuated data samples worth five years are generated for Φ_{ν_μ} and Φ_{ν_e}, where the matter oscillation are applied using the accept or reject method. The χ^2 test is performed with and without the electron neutrino flux as discussed in Sec. 5.5.

Figure 5.19 compares the confidence levels obtained with and without the electron neutrino flux Φ_{ν_e} in the $\sin^2\theta_{23} - |\Delta m^2_{32}|$ plane at 99% CL. Only a marginal difference in the precision is noted, where the addition of electron neutrino flux marginally dilutes the sensitivity to oscillation parameters.

5.9.2 Effect of event-by-event reconstruction

Previous studies [101,174] have measured a better precision in $\sin^2\theta_{23}$ and $|\Delta m^2_{32}|$, where the NUANCE data were smeared using the resolution functions and folded the detector efficiencies obtained from the GEANT4-based simulation studies on

single muons with fixed energy and direction [173]. In contrast, the current analysis uses a realistic approach of event-by-event reconstruction, where the tails of the resolution functions which were approximated in the previous studies have been included. Hence the previous method is unrealistic in nature, whereas the current method incorporates a realistic analysis procedure. In order to compare the two methods, a similar binning scheme B4, and a five-year experimental data comprising both muon and electron neutrino fluxes are used.[14]

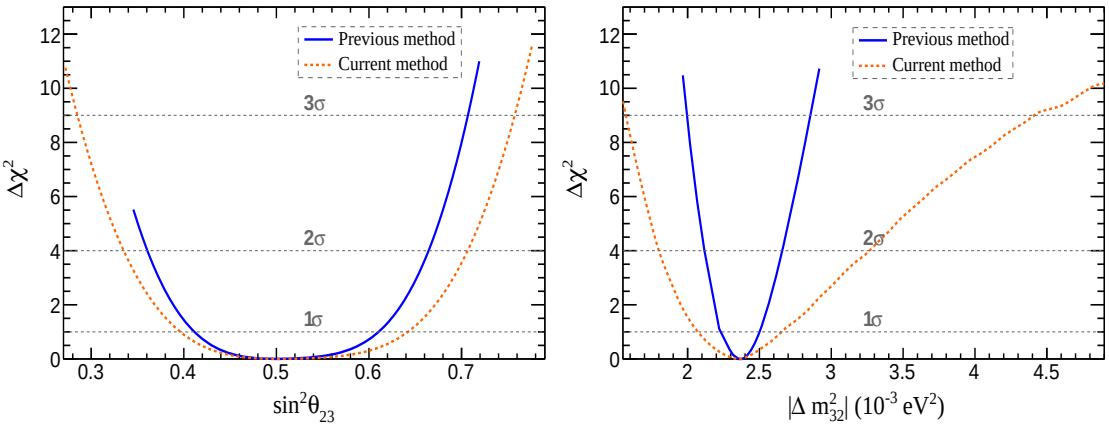

(a) (b)

Figure 5.20: $\Delta\chi^2$ as a function of (a)$\sin^2\theta_{23}$, for an input value of $\sin^2\theta_{23}(\text{true}) = 0.5$ and (b) Δm^2_{32}, for an input value of $\Delta m^2_{32}(\text{true}) = 2.32 \times 10^{-3}$ eV^2. The solid (blue) and dashed (orange) line shows the fit obtained from the previous and current methods respectively.

The data are fit to $\sin^2\theta_{23}$ and $|\Delta m^2_{32}|$ separately by marginalizing over $|\Delta m^2_{32}|$ and $\sin^2\theta_{23}$ respectively. The $\Delta\chi^2$ function obtained from the previous [174] and the current analysis methods are compared in Figure 5.20. The previous method yields a 1σ precision of 19.4% in $\sin^2\theta_{23}$, whereas it deteriorates to 23.8% for the current method (see Fig 5.20(a)). A similar behavior is observed in the fit to parameter $|\Delta m^2_{32}|$, where the precision deteriorates from 5.9% at 1σ in the previous method to 12.9% at 1σ for the current method (see Fig 5.20(b)). The drop in precision is more predominant in $|\Delta m^2_{32}|$ and is more evident with a 30% difference in precision at 3σ. This noted difference in precision can be solely attributed to the realistic approach used in the current analysis method via the event-by-event reconstruction.

[14]Note that the same binning scheme B4 is used in the previous analysis along with both the fluxes [174].

5.10 Summary

The main aim of the ICAL is to precisely determine the atmospheric neutrino oscillation parameters $\sin^2\theta_{23}$ and Δm^2_{32}, and measure the mass hierarchy (MH) of the neutrinos. A 50 kton $\times$ 1000 years data sample is generated and an event-by event reconstruction is performed to include the tails of the resolution functions which were approximated by the previous studies. The precision was observed to deteriorate with realistic reconstruction process, where a 4.4% and 7% difference in precision at 1σ is observed in $\sin^2\theta_{23}$ and Δm^2_{32} respectively.

The effect of event selection on the parameter sensitivities is also studied, where the precision was observed to deteriorate due to the reduction of reconstructed events by 42%. A difference in precision of 3% and 19.6% was observed in $\sin^2\theta_{23}$ and Δm^2_{32} respectively.

The fluctuations arising from the low event statistics are incorporated, and its effect on the parameter sensitivities and the mass hierarchy are studied by examining an ensemble of 60 experiments. The average parameter sensitivities obtained are observed to be largely consistent with the results obtained without the fluctuations. The fluctuations in the data lead to fluctuations in the mass hierarchy determination, where a 15% probability of identifying wrong mass hierarchy is observed. A mean resolution of $\Delta\chi^2_{MH} = 2.9$ rules out the wrong hierarchy with a significance of $\approx 1.7\sigma$ for the five-year run of 50 kton ICAL. Also a 3σ differentiation of correct mass hierarchy can be obtained at ICAL within a 13 to 14 years of operation.

The analysis presented in this chapter has only used muon information from CC ν_μ events, whereas the ICAL can also measure the hadron energy via proper calibration of hits. Hence, the result presented in this chapter are bound to improve with the addition of hadron information. A combined analysis including all the CC ν_μ and ν_e events along with the hadrons are discussed in the following chapter.

CHAPTER 6

Enhancing the oscillation sensitivity with hadrons

The ICAL is primarily designed to measure the muon momentum, where the neutrino and anti-neutrino events are distinguished by identifying the charge on the muon using a strong magnetic field ($\sim$ 1.5 T). However, the hadrons produced along with the muons leave signals in the form of shower that can also be measured by the detector. The calibration of hadron hits to energy [170], and the subsequent inclusion of hadron information in the oscillation studies is observed to improve the parameter sensitivities [175]. The subsequent sections describe the inclusion of hadron hits as an observable in the fit, and discuss its effect on the parameter sensitivities.

6.1 Hadron hits (Orighits)

The track finding algorithm separates the muon hits from the hadron hits (termed orighits), where the muons produce an average of one or two hits per layer and the rest are assumed to come from hadrons. Further, the information on the hadron hits are directly used in the fit after oscillation without any energy calibration. Figure 6.1 shows the simulated hadron hit distribution, obtained from a five year exposure to the 50 kton ICAL detector.

6.2 Binning and the χ^2 analysis

A simulated data sample of CC ν_μ and ν_e events are generated for an exposure of 50 kton $\times$ 1000 years using NUANCE [165] event generator, which is further

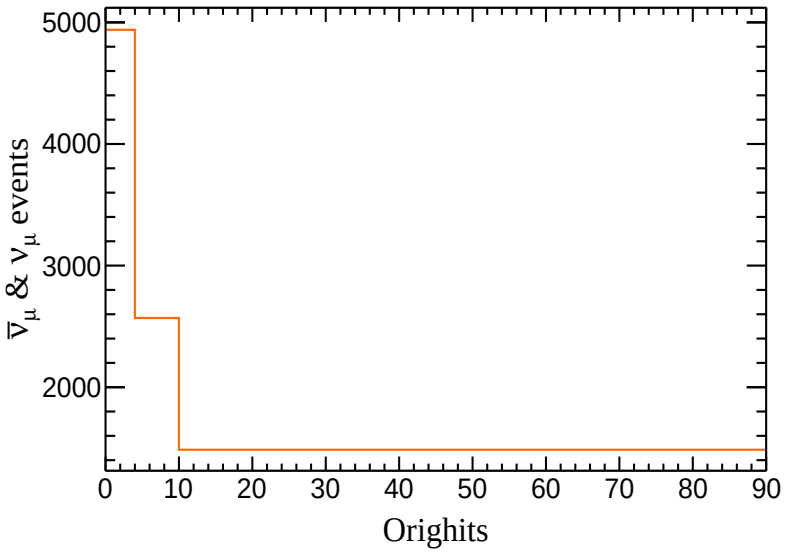

Figure 6.1: Distribution of hadron hits (orighits) in the detector for an exposure of 50 kton × 5 years.

simulated in a GEANT4 [166] based detector environment and reconstructed as discussed in Chapter 3. The data are scaled to an exposure of five years to reduce the fluctuations, and oscillations are applied using the accept or reject method as mentioned in Sec 5.2.1. Note that both ν_μ and ν_e fluxes are used in the oscillation analysis.

Binning

The hadron hits (orighits) in each event are binned along with the muon energy ($Q_\mu E_\mu$) and direction ($\cos\theta_z$) in a three dimensional fit, where Q_μ is the reconstructed charge of the muon tagged as $+1$ (-1) for the μ^+ (μ^-) from a $\bar{\nu}_\mu$ (ν_μ) event. A total of 22 bins with variable bin size in E_μ, 10 uniform bins in $\cos\theta_z$, and seven bins in Orighits are chose as shown in Table 6.1.

The χ^2 analysis

After binning, the five year unfluctuated data are fit to PDF[1] by defining the χ^2:

$$\chi^2 = \min_{\{\xi_k\}} \sum_{h=1}^{n_{\cos\theta_z}} \sum_{i=1}^{n_{E_\mu}} \sum_{j=1}^{n_{\text{Orighits}}} 2\left[\left(N_{hij}^{\text{pdf}} - N_{hij}^{\text{data}}\right) - N_{hij}^{\text{data}} \ln\left(\frac{N_{hij}^{\text{pdf}}}{N_{hij}^{\text{data}}}\right)\right] + \sum_{k=1}^{2} \xi_k^2, \quad (6.1)$$

[1] A 995 years worth data is used to construct the PDF.

Observable	Range	Bin width	Bins	Total bins
E_μ (GeV)	[-1.2, -0.2], [0.2, 1.2]	1.0	2	22
	[-2, -1.2], [1.2, 2]	0.4	4	
	[-2.5, -2], [2, 2.5]	0.5	2	
	[-5.5, -2.5], [2.5, 5.5]	1.0	6	
	[-8, -5.5], [5.5, 8]	2.5	2	
	[-15, -8], [8, 15]	7	2	
	[-25, -15], [15, 25]	10	2	
	[-50, -25], [25, 50]	25	2	
$\cos\theta_z$	[-1, 1]	0.2	10	10
Orighits	[0, 4]	4	1	7
	[4, 10]	3	2	
	[10, 40]	10	3	
	[40, 90]	50	1	

Table 6.1: The binning scheme for the reconstructed observables $\cos\theta_z$, E_μ and orighits

.

where,

$$N_{hij}^{\text{pdf}} = R\left[fT_{hij}^{\bar{\nu}} + (1-f)T_{hij}^{\nu}\right]\left[1 + \sum_{k=1}^{2}\pi_{hij}^{k}\xi_k\right], \tag{6.2}$$

where, N_{hij}^{data} are the number of events observed and N_{hij}^{pdf} are the number of events that are expected in a given $(\cos\theta_z^h, E_\mu^i, \text{Orighits}^j)$ bin, while $n_{\cos\theta_z}$, n_{E_μ} and n_{Orighits} are the total number of $\cos\theta_z$, E_μ and Orighits bins respectively, meaning there are $n_{\cos\theta_z} \times n_{E_\mu} \times n_{\text{Orighits}}$ observables in the fit. Here, N_{hij}^{data} is measured for the true values of oscillation parameters, summarized in Table 5.1, whereas N_{hij}^{pdf} is obtained by combining $\bar{\nu}_\mu$ and ν_μ PDFs as in Eq. 6.2, where $T_{hij}^{\bar{\nu}}$ and T_{hij}^{ν} are the normalized $\bar{\nu}$ and ν PDFs respectively, with R being the normalization factor in the fit which scales the PDF to the data entries. Here, the free parameter f describes the relative fraction of $\bar{\nu}_\mu$ and ν_μ in the sample.

The systematic uncertainties are parametrized by a set of variables $\{\xi_k\}$ called pulls, as described in Sec. 5.5.1.

6.3 Parameter determination

The five year unfluctuated data set is fit to determine $\sin^2\theta_{23}$ and $|\Delta m^2_{32}|$ separately by marginalizing over $|\Delta m^2_{32}|$ and $\sin^2\theta_{23}$ respectively. The $\Delta\chi^2$ function

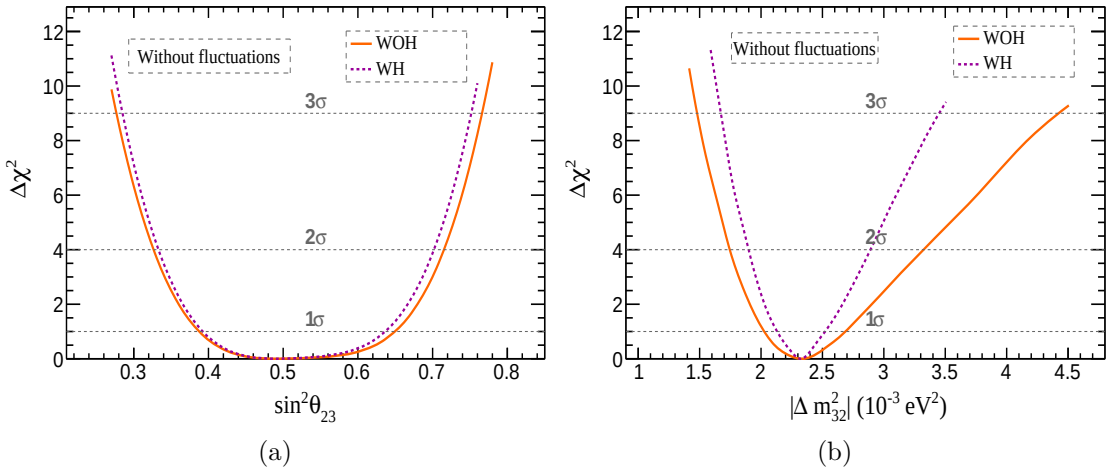

Figure 6.2: Comparison of $\Delta\chi^2$ with (WH) and without (WOH) hadron hits, as a function of (a)$\sin^2\theta_{23}$, for an input value of $\sin^2\theta_{23}(\text{true}) = 0.5$ and (b) Δm^2_{32}, for an input value of $\Delta m^2_{32}(\text{true}) = 2.32 \times 10^{-3}$ eV^2. The solid (orange) and dashed (purple) line shows the fit for WOH and WH respectively.

obtained from the fit with (WH) and without (WOH) hadron hits are compared in Fig. 6.2. The fit without hadrons yields a 1σ precision of 25%, whereas it marginally improves to 24% for the fit with hadron hits (Fig. 6.2a). A better behavior is observed in the fit to parameter $|\Delta m^2_{32}|$, where the precision improves from 14% at 1σ in the fit without hadrons to 8% at 1σ for the fit with hadrons (Fig. 6.2b). The increase in precision is more predominant in $|\Delta m^2_{32}|$ and is more evident with a 16% difference in precision at 3σ.

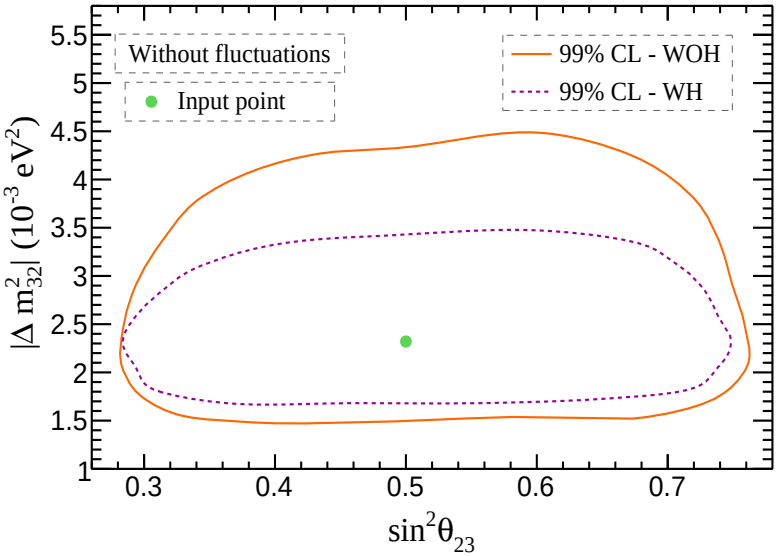

Figure 6.3: Comparison of confidence levels obtained in $\sin^2\theta_{23} - |\Delta m^2_{32}|$ plane with (WH) and without (WOH) the hadron hits. The solid (orange) and the dashed (purple) line shows the coverage area for WOH and WH respectively. The input (true) point is given by the green dot.

Figure 6.3 compares the precision reach in the $\sin^2\theta_{23} - \Delta m^2_{32}$ plane at 99% CL, obtained from the fit to five year unfluctuated pseudo-data set with and without the hadron hits. The fit with the hadron hits show smaller coverage area as expected from the one-parameter fit. Hence, the sensitivity of ICAL in measuring the oscillation parameters, especially $|\Delta m^2_{32}|$, improves with the addition of hadron hits information in the fit.

6.4 Summary

The ICAL is primarily designed to observe the secondary muons in the neutrino interaction, and the precision for the oscillation parameters that can be obtained for the muon only analysis is discussed in the previous chapters. The current chapter discuss the inclusion of hadron hits in the χ^2 fit, that are observed along with the muon tracks in the ICAL, and its impact on the parameter sensitivities.

The precision in $\sin^2\theta_{23}$ only shows a marginal improvement of 1% at 1σ with the addition of hadron hits, where as the precision in $|\Delta m^2_{32}|$ shows a significant improvement of 6% at 1σ. The ideal case in the previous method obtained a precision of 12% at 1σ in $\sin^2\theta_{23}$, and 2.9% in Δm^2_{32} with the addition of hadrons.

CHAPTER 7

Summary and future scope

Neutrino oscillation experiments have proved conclusively that neutrinos have mass, and it requires an extension of the SM or theories beyond the SM to explain how neutrinos acquire mass. Open questions about the octant of θ_{23}, MH, and the value of Dirac CP phase δ in the three-flavor oscillation sector are yet to be answered. Many neutrino experiments with varying neutrino sources are planned, and many are still operational, in a bid to precisely measure the parameter space of neutrino oscillations. The ICAL detector at INO is proposed to detect atmospheric neutrinos, with an aim to observe the MH and measure the oscillation parameters $\sin^2\theta_{23}$ and Δm^2_{32}. The work presented in this thesis describes a realistic method that can be used on the ICAL CC ν_μ data, and study its reach for a five year run of ICAL.

7.1 Summary

The proposed ICAL is a huge 50 kton detector of alternating iron and glass RPC layers with a modular structure of size 48.4 m (length in x) $\times$16 m (breadth in y) $\times$14.5 m (height in z), specifically designed to achieve a statistically significant number of neutrino interactions in a reasonable time. The ability of the magnetised ICAL to distinguish and observe the earth matter effects separately in ν and $\bar{\nu}$, helps to identify the MH of neutrinos. The work presented in this thesis analyzes a simulated set of CC ν_μ sample to study the sensitivity of ICAL. The neutrino events generated using NUANCE [165] is simulated in a virtual ICAL detector using a GEANT4 [166] detector simulation package, and the observables are obtained after the event-by-event reconstruction of the muons that are obtained along with the hadrons in the CC ν_μ interaction.

The oscillations are applied via the accept or reject method, and the events

are binned in muon reconstructed variables $\cos\theta_z$ and E_μ to study the parameter sensitivities. The systematic uncertainty due to the absolute normalization and the relative ν_μ and $\bar{\nu}_\mu$ flux normalizations are excluded, and instead fit to data by introducing free parameters within the fit. Further, by incorporating a realistic analysis procedure, the effect of event-by-event reconstruction, the effect of event selection, and the fluctuations arising from the low event statistics are studied for the first time in INO.

Use of event-by-event reconstruction

The work presented in the thesis uses event-by-event reconstruction, a realistic reconstruction process, where the tails of resolution functions which were approximated by single Gaussian and Vavilov functions in the previous such studies [101, 173, 175] have been included. In the previous studies, a lookup table for the detector efficiencies and resolutions was generated by studying single muons of fixed energy and direction. Later, the pseudodata were folded with these efficiencies and smeared using the resolutions within the lookup table. Hence, the parametrization of the resolution and efficiency that was used in the previous methods do not reflect the tails of these distributions.

The energy and angular resolution of muons, and the charge ID efficiency was observed to deteriorate with event-by-event reconstruction. Hence, the precision in parameter sensitivities was also observed to deteriorate in comparison to the previous method (see Sec. 5.9.2). The precision in $\sin^2\theta_{23}$ deteriorates from 19.4% in the previous method to 23.8% at 1σ, whereas in $|\Delta m^2_{32}|$ it deteriorates from 5.9% to 12.9% at 1σ.

Effect of event selection

The lookup tables used in previous method [101, 173, 175], containing the muon resolution and effciencies, were obtained after the event selection process as in Ref. [171]. The event selection removes the reconstructed events that are adversely affected by non-uniform magnetic field and support structures within the detector. Hence, the process of event selection is applied after the event-by-event

reconstruction, and its effect on the parameter sensitivities are studied for the first time.

After applying the event selection, the angular and energy resolution improves along with the charge ID efficiency, but the reconstruction efficiency deteriorates as 40% of the reconstructed events are lost to the event selection. As a result, the precision in the parameters $\sin^2\theta_{23}$ and $|\Delta m^2_{32}|$ were observed to deteriorate (see Sec. 5.6.1). The precision in $\sin^2\theta_{23}$ marginally deteriorates from 45% at 3σ to 48% after the event selection, whereas in $|\Delta m^2_{32}|$ it deteriorates from 59.4% to 79% at 3σ. Hence the study shows that, all the reconstructed muon events must be included in the fit to get best possible constraints on the oscillation parameters.

Low event statistics

Low event statistics is a common feature among neutrino experiments. Previous methods [101,173,175] used very large sample sizes, and scaled them to negate the effect of low event statistics. Hence, very little has been learned in the case of INO about the implication of fluctuations in the data and its affect on the parameter sensitivities.

An ensemble of 60 independent fluctuated pseudo-data sets are used to study the effect of low event statistics on the precision measurements of the oscillation parameters. The constraints on the parameters $\sin^2\theta_{23}$ and Δm^2_{32} are studied with and without fluctuations, where a reasonable agreement is observed between the unfluctuated and the average fluctuated precision reach obtained in the $\sin^2\theta_{23} - \Delta m^2_{32}$ plane (see Sec. 5.7). Also, a mean resolution of $\Delta\chi^2_{\rm MH} = 2.9$ from an ensemble of 60 experiments, rules out the wrong hierarchy with a significance od $\approx 1.7\sigma$. A 15% probability of identifying wrong MH is also observed as a result of fluctuations in the data. Hence, the study shows the range of possible outcomes that can be obtained for a five year run of the ICAL experiment.

The sensitivity of ICAL in measuring the oscillation parameters, were observed to improve with the addition of hadron information. The precision in $\sin^2\theta_{23}$ marginally improves from 25% at 1σ to 24% after including the hadron hits, whereas the fit to $|\Delta m^2_{32}|$ shows a better improvement in precision from 14%

at 1σ to 8% after adding the hadron information (see Sec. 6.3).

7.2 Future scope

The CP phase δ is insensitive to ν_μ events, as the survival probabilities ($P_{\mu\mu}$ in case of ν_μ) have weak dependence on the CP phase, and secondly the transitional probabilities $P_{e\mu}$ is very small. Hence, only ν_e flux can have the sensitivity to the CP phase due to larger ν_μ flux contributing to the ν_e events in the detector, provided the backgrounds (trackless CC ν_μ, and neutral-current (NC)) are completely separated. Studies are underway to find a method that can effectively separate the ν_e signal from the background. Also, a clear separation of NC events could help in effectively studying the sterile neutrino oscillations.

Separation of CC ν_μ events from CC ν_e and NC is quite robust for $E_\mu \gtrsim 1$GeV and has been discussed elsewhere [101]. Separation of low energy CC ν_μ events from CC ν_e and NC events, and the separation of NC events from CC ν_e is an ongoing effort of the INO-ICAL collaboration. A combined analysis including all the CC and NC events will give the maximum sensitivity that the ICAL can attain, and is likely to improve the results presented in this thesis.

In future, ICAL can be used to study physics scenarios like CPT violation, magnetic monopoles, dark matter etc, and could lead us to a better understanding of nature around us.

APPENDIX A

Effects of marginalization

The probability distribution function (PDF) is fit to the pseudo-data, where the the oscillation parameters are varied to determine the best-fit values of $\sin^2\theta_{23}$ and Δm^2_{32}. The other parameters in the PDF (mixing angles and the mass-square differences) are well determined from the global fits [51], Table 1.3, within certain uncertainty. Hence an additional constraint is added on each of these parameters (mainly $\sin^2 2\theta_{13}$ and Δm^2_{21}) using priors within the χ^2 definition, *i.e.,*

$$\chi^2_{\text{total}} = \chi^2_{\text{data}} + \chi^2_{\text{prior}} \tag{A.1}$$

here χ^2_{data} is the general measure of the difference in theoretical and experimental values given by the Eq. 5.5, and χ^2_{prior} is the sum of priors on $\sin^2 2\theta_{13}$ and Δm^2_{21} defined as:

$$\chi^2_{\text{prior}} = \left(\frac{\sin^2 2\theta_{13} - (\sin^2 2\theta_{13})_{\text{true}}}{\sigma(\sin^2 2\theta_{13})}\right) + \left(\frac{\Delta m^2_{21} - (\Delta m^2_{21})_{\text{true}}}{\sigma(\Delta m^2_{21})}\right) \tag{A.2}$$

where $\sigma(\sin^2 2\theta_{13})$ and $\sigma(\Delta m^2_{21})$ are the 1σ uncertainty in $\sin^2 2\theta_{13}$ and Δm^2_{21} respectively.

Parameter	Marginalization range
$\sin^2\theta_{23}$ [a]	[0,1]
Δm^2_{32} (eV^2) [b]	[0.0005,0.005]
f	[0,1]
R	Unconstrained
$\sin^2\theta_{13}$	Unconstrained
$\sin^2\theta_{12}$	Not marginalized
Δm^2_{21} (eV^2)	Unconstrained
δ_{cp}	Not marginalized

Table A.1: Marginalization of the parameters as used in the fit with priors

[a] Marginalized when the data is fit to determine Δm^2_{32}
[b] Marginalized when the data is fit to determine $\sin^2\theta_{23}$

During the fit the oscillation parameters are marginalized over the ranges given in the Table A.1. The parameters $\sin^2\theta_{13}$ and Δm^2_{21} are varied freely with a prior constrain of 6% and 2% respectively, whereas the parameters $\sin^2\theta_{12}$ and δ_{cp} are not marginalized. The relative normalization f, and the absolute normalization R, are the free parameter in the fit which are always left unconstrained.

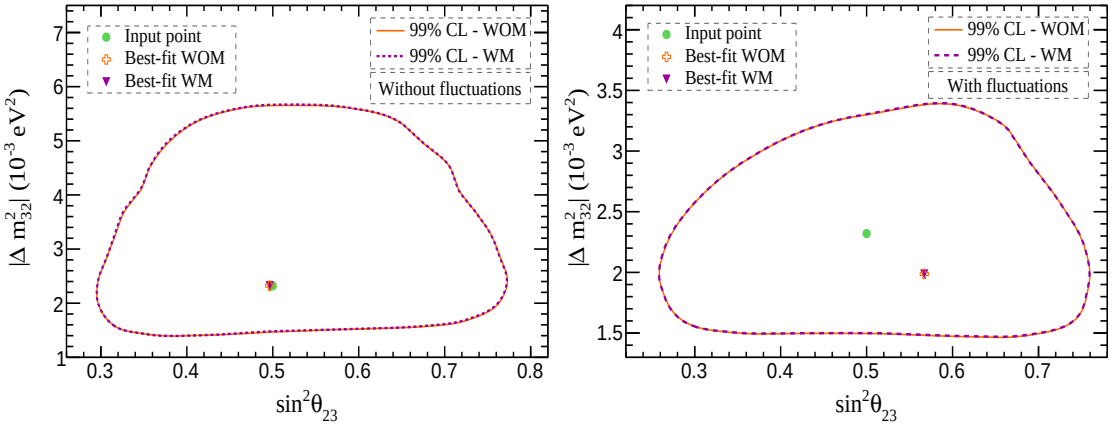

(a) (b)

Figure A.1: The comparison of precision reach obtained from the fit with (WM) and without (WOM) marginalization, on the five year pseudo-data (a) without fluctuations (WOS) and (b) with fluctuations. Note that the scales in the x and y axis are different in both plots.

The effect of marginalizing $\sin^2\theta_{13}$ and Δm^2_{21} are shown in Fig. A.1, where a negligible change in confidence intervals is observed. The Figure A.1a shows the correlated confidence level in $\sin^2\theta_{23}$ and Δm^2_{32} plane for a five year data-set without fluctuations, whereas the Figure A.1b shows the same for a fluctuated data set.[1] The comparison of precision with (WM) and without (WOM) the marginalization shows very little or negligible change. Evidently, the parameters $\sin^2\theta_{13}$ and Δm^2_{21} are well determined from the fit, and hence are not marginalized in the further analysis presented in the thesis.

[1]Few other fluctuated sets were also studied, but were observed not to make any difference in the precision with marginalization of $\sin^2\theta_{13}$ and Δm^2_{21}.

APPENDIX B

Fluctuations in PDF

The fluctuations in the theory (PDF) effects the parameter sensitivity and determination. Hence it is important to reduce the fluctuations in the theory. The PDFs with varying statistics are generated for an exposure ranging from 95 to 995 years, where they are fit to the same fluctuated data set worth five years. The oscillations are applied via accept or reject method before performing the χ^2 fit.[1] The Figure B.1 compares the fit to different PDFs sizes.[2]

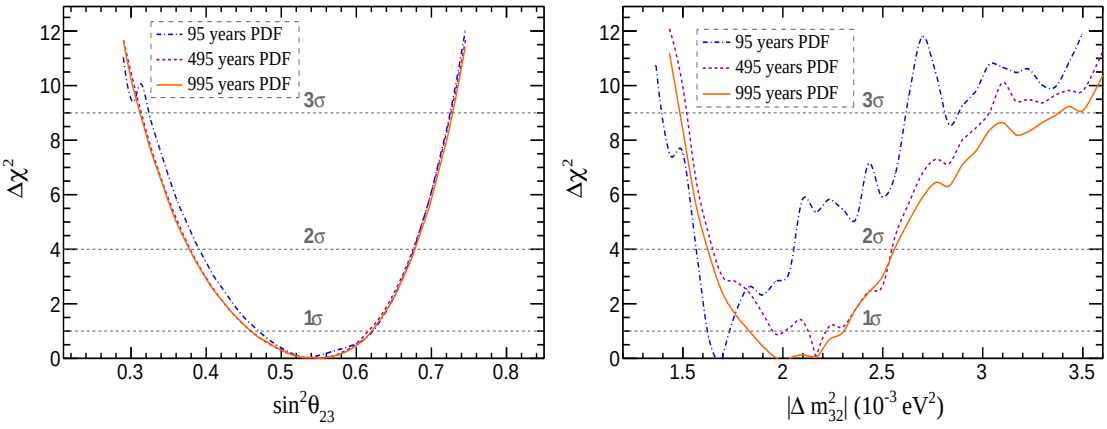

(a) (b)

Figure B.1: Comparison of $\Delta\chi^2$ from different fits using different PDF sizes, as a function of (a) $\sin^2\theta_{23}$, for an input value of $\sin^2\theta_{23}$(true)=0.5 and (b) Δm^2_{23}, for an input value of Δm^2_{23}(true)= 0.00232 eV^2.

The fit to $\sin^2\theta_{23}$ is shown in Fig. B.1a, where the data is fit to different PDFs of varying sizes, marginalizing over $|\Delta m^2_{32}|$, for an input value of $\sin^2\theta_{23} = 0.5$. The precision in $\sin^2\theta_{23}$ almost remains constant for all the different fits with varying PDF sizes, and is observed to be unaffected by the statistical fluctuation in theory (PDF).

[1]Note that three flavor oscillations are applied to save the computational time, where the time required to compute the matter effects is larger than the vacuum oscillations.

[2]Note that only three sample sizes worth, 95 years, 495 years, and 995 years are used to represent in the Fig. B.1.

The fluctuations in the theory largely affects the parameter Δm^2_{32}, whereas Fig. B.1b compares the fit to the parameter $|\Delta m^2_{32}|$ for various PDF sizes, marginalizing over $\sin^2\theta_{23}$, for an input value of $\Delta m^2_{32} = 2.32 \times 10^{-3}$ eV^2. The multiple local minimas in the fit to $|\Delta m^2_{32}|$, is observed to reduce with the reduction in the theoretical fluctuations (increasing PDF statistics). The precision in $|\Delta m^2_{32}|$ varies with the fluctuations in the PDF, and is observed to attain a stable value with the increase in PDF statistics. Hence, a PDF size of 1000 year exposure is chose to minimize the resultant fluctuations. Note that the computation time increases with increase in PDF size, and the choice of PDF worth 1000 years is reasonable as the precision is observed to reach an asymptotic value.

BIBLIOGRAPHY

[1] ATLAS Collaboration, G. Aad *et al.*, *Observation of a new particle in the search for the Standard Model Higgs boson with the ATLAS detector at the LHC*, *Physics Letters B* **716** (2012) 1 – 29. [Cited page: 1.]

[2] CMS Collaboration, S. Chatrchyan *et al.*, *Observation of a new boson at a mass of 125 GeV with the CMS experiment at the LHC*, *Physics Letters B* **716** (2012) 30 – 61. [Cited page: 1.]

[3] Planck Collaboration, P. A. R. Ade *et al.*, *Planck 2015 results - XIII. Cosmological parameters*, *A&A* **594** (2016) A13. [Cited pages: 1 and 3.]

[4] SNO Collaboration, B. Aharmim *et al.*, *Low-energy-threshold analysis of the Phase I and Phase II data sets of the Sudbury Neutrino Observatory*, *Phys. Rev. C* **81** (May, 2010) 055504. [Cited pages: 1 and 3.]

[5] The Super-Kamiokande Collaboration, R. Wendell *et al.*, *Atmospheric neutrino oscillation analysis with subleading effects in Super-Kamiokande I, II, and III*, *Phys. Rev. D* **81** (May, 2010) 092004. [Cited pages: 1 and 3.]

[6] The KamLAND Collaboration, S. Abe *et al.*, *Precision Measurement of Neutrino Oscillation Parameters with KamLAND*, *Phys. Rev. Lett.* **100** (Jun, 2008) 221803. [Cited pages: 1, 3, and 25.]

[7] K2K Collaboration, M. H. Ahn *et al.*, *Measurement of neutrino oscillation by the K2K experiment*, *Phys. Rev. D* **74** (Oct, 2006) 072003. [Cited pages: 1, 3, and 26.]

[8] T2K Collaboration, K. Abe *et al.*, *First muon-neutrino disappearance study with an off-axis beam*, *Phys. Rev. D* **85** (Feb, 2012) 031103. [Cited pages: 1 and 27.]

[9] Double Chooz Collaboration, Y. Abe *et al.*, *Indication of Reactor $\overline{\nu}_e$ Disappearance in the Double Chooz Experiment*, *Phys. Rev. Lett.* **108** (Mar, 2012) 131801. [Cited pages: 1, 3, and 26.]

[10] The MINOS Collaboration, P. Adamson *et al.*, *Measurements of atmospheric neutrinos and antineutrinos in the MINOS far detector*, *Phys. Rev. D* **86** (Sep, 2012) 052007. [Cited pages: 1 and 3.]

[11] RENO Collaboration, J. K. Ahn *et al.*, *Observation of Reactor Electron Antineutrinos Disappearance in the RENO Experiment*, *Phys. Rev. Lett.* **108** (May, 2012) 191802. [Cited pages: 1, 3, and 26.]

[12] Daya Bay Collaboration, F. P. An *et al.*, *Observation of Electron-Antineutrino Disappearance at Daya Bay*, *Phys. Rev. Lett.* **108** (Apr, 2012) 171803. [Cited pages: 1, 3, and 26.]

[13] LSND Collaboration, A. Aguilar *et al.*, *Evidence for neutrino oscillations from the observation of $\overline{\nu}_e$ appearance in a $\overline{\nu}_\mu$ beam*, *Phys. Rev. D* **64** (Nov, 2001) 112007. [Cited pages: 1, 3, and 26.]

[14] MiniBooNE Collaboration, A. A. Aguilar-Arevalo *et al.*, *Event Excess in the MiniBooNE Search for $\overline{\nu}_\mu \to \overline{\nu}_e$ Oscillations*, *Phys. Rev. Lett.* **105** (Oct, 2010) 181801. [Cited pages: 1, 3, and 26.]

[15] MiniBooNE Collaboration, A. A. Aguilar-Arevalo *et al.*, *Improved Search for $\overline{\nu}_\mu \to \overline{\nu}_e$ Oscillations in the MiniBooNE Experiment*, *Phys. Rev. Lett.* **110** (Apr, 2013) 161801. [Cited pages: 1, 3, and 26.]

[16] Th. A. Mueller, *et al.*, *Improved predictions of reactor antineutrino spectra*, *Phys. Rev. C* **83** (May, 2011) 054615. [Cited page: 1.]

[17] M. Fukugita and T. Yanagida, *Barygenesis without grand unification*, *Physics Letters B* **174** (1986) 45 – 47. [Cited page: 1.]

[18] V. A. Kuzmin, V. A. Rubakov, and M. E. Shaposhnikov, *On the Anomalous Electroweak Baryon Number Nonconservation in the Early Universe*, *Phys. Lett.* **B155** (1985) 36. [Cited page: 1.]

[19] Kevork N. Abazajian, *Sterile neutrinos in cosmology*, *Physics Reports* **711-712** (2017) 1 – 28. [Cited page: 1.]

[20] S.M. Bilenky, *Neutrino. History of a unique particle*, *The European Physical Journal H* **38** (Apr, 2013) 345–404. [Cited page: 2.]

[21] J. Chadwick, *Possible Existence of a Neutron*, *Nature* **129** (1932) 312. [Cited page: 2.]

[22] E. Fermi, *Versuch einer Theorie der β-Strahlen. I*, *Zeitschrift für Physik* **88** (Mar, 1934) 161–177. [Cited page: 2.]

[23] B. Pontecorvo. Chalk River Laboratory Report PD-205, 1946. [Cited pages: 2 and 7.]

[24] F. Reines and C. L. Cowan, *The Neutrino*, *Nature* **178** (Sept., 1956) 446–449. [Cited page: 2.]

[25] T. D. Lee and C. N. Yang, *Question of Parity Conservation in Weak Interactions*, *Phys. Rev.* **104** (Oct, 1956) 254–258. [Cited page: 2.]

[26] C. S. Wu, *et al.*, *Experimental Test of Parity Conservation in Beta Decay*, *Phys. Rev.* **105** (Feb, 1957) 1413–1415. [Cited page: 2.]

[27] Richard L. Garwin, Leon M. Lederman, and Marcel Weinrich, *Observations of the Failure of Conservation of Parity and Charge Conjugation in Meson Decays: the Magnetic Moment of the Free Muon*, *Phys. Rev.* **105** (Feb, 1957) 1415–1417. [Cited page: 2.]

[28] M. Goldhaber, L. Grodzins, and A. W. Sunyar, *Helicity of Neutrinos*, *Phys. Rev.* **109** (Feb, 1958) 1015–1017. [Cited page: 2.]

[29] R. P. Feynman and M. Gell-Mann, *Theory of the Fermi Interaction*, *Phys. Rev.* **109** (Jan, 1958) 193–198. [Cited page: 2.]

[30] E. C. G. Sudarshan and R. E. Marshak, *Chirality Invariance and the Universal Fermi Interaction*, *Phys. Rev.* **109** (Mar, 1958) 1860–1862. [Cited page: 2.]

[31] G. Danby, *et al.*, *Observation of High-Energy Neutrino Reactions and the Existence of Two Kinds of Neutrinos*, *Phys. Rev. Lett.* **9** (Jul, 1962) 36–44. [Cited page: 3.]

[32] Steven Weinberg, *A Model of Leptons*, *Phys. Rev. Lett.* **19** (Nov, 1967) 1264–1266. [Cited page: 3.]

[33] A. Salam and J.C. Ward, *Electromagnetic and weak interactions*, *Physics Letters* **13** (1964) 168 – 171. [Cited page: 3.]

[34] Sheldon L. Glashow, *Partial-symmetries of weak interactions*, *Nuclear Physics* **22** (1961) 579 – 588. [Cited page: 3.]

[35] M. L. Perl *et al.*, *Evidence for Anomalous Lepton Production in $e^+ - e^-$ Annihilation*, *Phys. Rev. Lett.* **35** (Dec, 1975) 1489–1492. [Cited page: 3.]

[36] F.J. Hasert *et al.*, *Search for elastic muon-neutrino electron scattering*, *Physics Letters B* **46** (1973) 121 – 124. [Cited page: 3.]

[37] UA1 Collaboration, G. Arnison *et al.*, *Experimental observation of isolated large transverse energy electrons with associated missing energy at s=540 GeV*, *Physics Letters B* **122** (1983) 103 – 116. [Cited page: 3.]

[38] UA2 Collaboration, P. Bagnaia *et al.*, *Evidence for $Z^0 \to e^+e^-$ at the CERN pp collider*, *Physics Letters B* **129** (1983) 130 – 140. [Cited page: 3.]

[39] Mark II Collaboration, G. S. Abrams *et al.*, *Measurements of Z-boson resonance parameters in e^+e^- annihilation*, *Phys. Rev. Lett.* **63** (Nov, 1989) 2173–2176. [Cited page: 3.]

[40] DELPHI Collaboration, P. Abreu *et al.*, *Determination of Z^0 resonance parameters and couplings from its hadronic and leptonic decays*, *Nuclear Physics B* **367** (1991) 511 – 574. [Cited page: 3.]

[41] ALEPH Collaboration, D. Decamp *et al.*, *Improved measurements of electroweak parameters from Z decays into fermion pairs*, *Zeitschrift für Physik C Particles and Fields* **53** (Mar, 1992) 1–20. [Cited page: 3.]

[42] LEP, DELPHI, OPAL, ALEPH, L3, G. Alexander *et al.*, *Electroweak parameters of the Z^0 resonance and the Standard Model: the LEP Collaborations*, *Phys. Lett.* **B276** (1992) 247–253. [Cited page: 3.]

[43] DONUT Collaboration, K. Kodama *et al.*, *Observation of tau neutrino interactions*, *Physics Letters B* **504** (2001) 218 – 224. [Cited page: 3.]

[44] K. Abe, *et al.*, *The {T2K} experiment*, *Nucl. Instrum. Methods A* **659** (2011) 106 – 135. [Cited page: 3.]

[45] Daya Bay Collaboration and MINOS Collaboration, P. Adamson *et al.*, *Limits on Active to Sterile Neutrino Oscillations from Disappearance Searches in the MINOS, Daya Bay, and Bugey-3 Experiments*, *Phys. Rev. Lett.* **117** (Oct, 2016) 151801. [Cited pages: 3 and 26.]

[46] E. Majorana, *Teoria simmetrica dellâĂŹelettrone e del positrone*, *Nuovo Cimento* **5** (1937) 171. [Cited page: 3.]

[47] S. M. Bilenky and S. T. Petcov, *Massive neutrinos and neutrino oscillations*, *Rev. Mod. Phys.* **59** (Jul, 1987) 671–754. [Cited page: 3.]

[48] Nathalie Palanque-Delabrouille *et al.*, *Neutrino masses and cosmology with Lyman-alpha forest power spectrum*, *Journal of Cosmology and Astroparticle Physics* **2015** (2015) 011. [Cited page: 4.]

[49] Ziro Maki, Masami Nakagawa, and Shoichi Sakata, *Remarks on the Unified Model of Elementary Particles*, *Progress of Theoretical Physics* **28** (1962) 870–880. [Cited pages: 4, 8, and 12.]

[50] KamLAND-Zen Collaboration, A. Gando *et al.*, *Limit on Neutrinoless $\beta\beta$ Decay of ^{136}Xe from the First Phase of KamLAND-Zen and Comparison with the Positive Claim in ^{76}Ge*, *Phys. Rev. Lett.* **110** (Feb, 2013) 062502. [Cited page: 4.]

[51] Particle Data Group, C. Patrignani *et al.*, *Review of Particle Physics*, *Chin. Phys.* **C40** (2016) 100001. [Cited pages: 4, 13, 20, 21, 28, and 108.]

[52] Carlo Giunti and Chung W. Kim, *Fundamentals of Neutrino Physics and Astrophysics*. Oxford University Press, 2007. [Cited pages: 5, 8, 21, and 25.]

[53] J. A. Formaggio and G. P. Zeller, *From eV to EeV: Neutrino cross sections across energy scales*, *Rev. Mod. Phys.* **84** (Sep, 2012) 1307–1341. [Cited pages: 5 and 6.]

[54] Raymond Davis, Don S. Harmer, and Kenneth C. Hoffman, *Search for Neutrinos from the Sun*, *Phys. Rev. Lett.* **20** (May, 1968) 1205–1209. [Cited pages: 7, 18, and 19.]

[55] John N. Bahcall, Neta A. Bahcall, and Giora Shaviv, *Present Status of the Theoretical Predictions for the ^{37}Cl Solar-Neutrino Experiment*, *Phys. Rev. Lett.* **20** (May, 1968) 1209–1212. [Cited page: 7.]

[56] B. Pontecorvo, *Mesonium and anti-mesonium*, *Sov. Phys. JETP* **6** (1957) 429. [Cited page: 8.]

[57] M. Gell-Mann and A. Pais, *Behavior of Neutral Particles under Charge Conjugation*, *Phys. Rev.* **97** (Mar, 1955) 1387–1389. [Cited page: 8.]

[58] Rabindra N Mohapatra and Palash B Pal, *Massive Neutrinos in Physics and Astrophysics*. World Scientific, 2012. [Cited page: 10.]

[59] S. M. Bilenky and S. T. Petcov, *Massive neutrinos and neutrino oscillations*, *Rev. Mod. Phys.* **59** (Jul, 1987) 671–754. [Cited page: 12.]

[60] S Adrián-Martínez *et al.*, *Letter of intent for KM3NeT 2.0*, *Journal of Physics G: Nuclear and Particle Physics* **43** (jun, 2016) 084001. [Cited page: 12.]

[61] KamLAND Collaboration, A. Gando *et al.*, *Reactor on-off antineutrino measurement with KamLAND*, *Phys. Rev. D* **88** (Aug, 2013) 033001. [Cited page: 12.]

[62] Raj Gandhi, *et al.*, *Large Matter Effects in $\nu_\mu \to \nu_\tau$ Oscillations*, *Phys. Rev. Lett.* **94** (Feb, 2005) 051801. [Cited pages: 13 and 14.]

[63] L. Wolfenstein, *Neutrino oscillations in matter*, *Phys. Rev. D* **17** (May, 1978) 2369–2374. [Cited page: 13.]

[64] S. P. Mikheev and A. Yu. Smirnov, *Resonance Amplification of Oscillations in Matter and Spectroscopy of Solar Neutrinos*, *Sov. J. Nucl. Phys.* **42** (1985) 913–917. [Cited pages: 13 and 15.]

[65] D. Indumathi, M. V. N. Murthy, G. Rajasekaran, and Nita Sinha, *Neutrino oscillation probabilities: Sensitivity to parameters*, *Phys. Rev. D* **74** (Sep, 2006) 053004. [Cited pages: 15, 70, and 72.]

[66] Adam M. Dziewonski and Don L. Anderson, *Preliminary reference Earth model*, *Physics of the Earth and Planetary Interiors* **25** (1981) 297 – 356. [Cited pages: 15 and 71.]

[67] V.S. Beresinsky and G.T. Zatsepin, *Cosmic rays at ultra high energies (neutrino?)*, *Physics Letters B* **28** (1969) 423 – 424. [Cited page: 17.]

[68] P. Padovani, *et al.*, *Active galactic nuclei: what's in a name?*, *The Astronomy and Astrophysics Review* **25** (Aug, 2017) 2. [Cited page: 17.]

[69] Brent Follin, Lloyd Knox, Marius Millea, and Zhen Pan, *First Detection of the Acoustic Oscillation Phase Shift Expected from the Cosmic Neutrino Background*, *Phys. Rev. Lett.* **115** (Aug, 2015) 091301. [Cited page: 17.]

[70] U.F. Katz and Ch. Spiering, *High-energy neutrino astrophysics: Status and perspectives*, *Progress in Particle and Nuclear Physics* **67** (2012) 651 – 704. [Cited page: 17.]

[71] IceCube Collaboration, M. G. Aartsen *et al.*, *Constraints on Ultrahigh-Energy Cosmic-Ray Sources from a Search for Neutrinos above 10 PeV with IceCube*, *Phys. Rev. Lett.* **117** (Dec, 2016) 241101. [Cited page: 18.]

[72] ARA Collaboration, P. Allison *et al.*, *Performance of two Askaryan Radio Array stations and first results in the search for ultrahigh energy neutrinos*, *Phys. Rev. D* **93** (Apr, 2016) 082003. [Cited page: 18.]

[73] ARIANNA Collaboration, S.W. Barwick *et al.*, *A first search for cosmogenic neutrinos with the ARIANNA Hexagonal Radio Array*, *Astroparticle Physics* **70** (2015) 12 – 26. [Cited page: 18.]

[74] Kamiokande Collaboration, K. Hirata *et al.*, *Observation of a neutrino burst from the supernova SN1987A*, *Phys. Rev. Lett.* **58** (Apr, 1987) 1490–1493. [Cited page: 18.]

[75] R. M. Bionta *et al.*, *Observation of a neutrino burst in coincidence with supernova 1987A in the Large Magellanic Cloud*, *Phys. Rev. Lett.* **58** (Apr, 1987) 1494–1496. [Cited page: 18.]

[76] M. Aglietta *et al.*, *On the Event Observed in the Mont Blanc Underground Neutrino Observatory during the Occurrence of Supernova 1987 a*, *EPL (Europhysics Letters)* **3** (1987) 1315. [Cited page: 18.]

[77] Carlos Pena-Garay and Aldo Serenelli, *Solar neutrinos and the solar composition problem*, arXiv:0811.2424. [Cited pages: 18 and 19.]

[78] T.A. Kirsten, *GALLEX solar neutrino results*, *Progress in Particle and Nuclear Physics* **40** (1998) 85 – 99. [Cited page: 19.]

[79] W. Hampel *et al.*, *GALLEX solar neutrino observations: results for GALLEX IV*, *Physics Letters B* **447** (1999) 127 – 133. [Cited page: 19.]

[80] M. Altmann *et al.*, *Complete results for five years of GNO solar neutrino observations*, *Physics Letters B* **616** (2005) 174 – 190. [Cited page: 19.]

[81] SAGE Collaboration, J. N. Abdurashitov *et al.*, *Measurement of the solar neutrino capture rate with gallium metal. III. Results for the 2002–2007 data-taking period*, *Phys. Rev. C* **80** (Jul, 2009) 015807. [Cited page: 19.]

[82] Borexino Collaboration, G. Bellini *et al.*, *Precision Measurement of the* ^{7}Be *Solar Neutrino Interaction Rate in Borexino*, *Phys. Rev. Lett.* **107** (Sep, 2011) 141302. [Cited page: 19.]

[83] Borexino Collaboration, G. Bellini *et al.*, *First Evidence of pep Solar Neutrinos by Direct Detection in Borexino*, *Phys. Rev. Lett.* **108** (Feb, 2012) 051302. [Cited page: 19.]

[84] Borexino Collaboration, G. Bellini *et al.*, *Neutrinos from the primary proton-proton fusion process in the Sun*, *Nature* **512** (2014) 383–386. [Cited page: 19.]

[85] Borexino Collaboration, G. Bellini *et al.*, *Measurement of the solar* ^{8}B *neutrino rate with a liquid scintillator target and 3 MeV energy threshold in the Borexino detector*, *Phys. Rev. D* **82** (Aug, 2010) 033006. [Cited page: 19.]

[86] Borexino Collaboration, G. Bellini *et al.*, *Final results of Borexino Phase-I on low-energy solar neutrino spectroscopy*, *Phys. Rev. D* **89** (Jun, 2014) 112007. [Cited page: 19.]

[87] Kamiokande Collaboration, K. S. Hirata *et al.*, *Observation of* ^{8}B *solar neutrinos in the Kamiokande-II detector*, *Phys. Rev. Lett.* **63** (Jul, 1989) 16–19. [Cited page: 20.]

[88] Kamiokande Collaboration, Y. Fukuda *et al.*, *Solar Neutrino Data Covering Solar Cycle 22*, *Phys. Rev. Lett.* **77** (Aug, 1996) 1683–1686. [Cited page: 20.]

[89] Super-Kamiokande Collaboration, Y. Fukuda *et al.*, *Measurements of the Solar Neutrino Flux from Super-Kamiokande's First 300 Days*, *Phys. Rev. Lett.* **81** (Aug, 1998) 1158–1162. [Cited page: 20.]

[90] Super-Kamiokande Collaboration, J. Hosaka *et al.*, *Solar neutrino measurements in Super-Kamiokande-I*, *Phys. Rev. D* **73** (Jun, 2006) 112001. [Cited page: 20.]

[91] Super-Kamiokande Collaboration, J. P. Cravens *et al.*, *Solar neutrino measurements in Super-Kamiokande-II*, *Phys. Rev. D* **78** (Aug, 2008) 032002. [Cited page: 20.]

[92] Super-Kamiokande Collaboration, K. Abe *et al.*, *Solar neutrino results in Super-Kamiokande-III*, *Phys. Rev. D* **83** (Mar, 2011) 052010. [Cited page: 20.]

[93] SNO Collaboration, Q. R. Ahmad *et al.*, *Measurement of the Rate of* $\nu_e + d \to p + p + e^-$ *Interactions Produced by* ^8B *Solar Neutrinos at the Sudbury Neutrino Observatory*, *Phys. Rev. Lett.* **87** (Jul, 2001) 071301. [Cited page: 20.]

[94] SNO Collaboration, Q. R. Ahmad *et al.*, *Direct Evidence for Neutrino Flavor Transformation from Neutral-Current Interactions in the Sudbury Neutrino Observatory*, *Phys. Rev. Lett.* **89** (Jun, 2002) 011301. [Cited page: 20.]

[95] SNO Collaboration, B. Aharmim and otehrs, *Electron energy spectra, fluxes, and day-night asymmetries of* ^8B *solar neutrinos from measurements with NaCl dissolved in the heavy-water detector at the Sudbury Neutrino Observatory*, *Phys. Rev. C* **72** (Nov, 2005) 055502. [Cited page: 20.]

[96] SNO Collaboration, B. Aharmim *et al.*, *Independent Measurement of the Total Active* ^{8}B *Solar Neutrino Flux Using an Array of* ^{3}He *Proportional Counters at the Sudbury Neutrino Observatory*, *Phys. Rev. Lett.* **101** (Sep, 2008) 111301. [Cited page: 20.]

[97] L. Pasquali and M. H. Reno, *Tau neutrino fluxes from atmospheric charm*, *Phys. Rev. D* **59** (Mar, 1999) 093003. [Cited pages: 21 and 73.]

[98] M. Honda, T. Kajita, K. Kasahara, and S. Midorikawa, *Improvement of low energy atmospheric neutrino flux calculation using the JAM nuclear interaction model*, *Phys. Rev. D* **83** (Jun, 2011) 123001. [Cited pages: 22, 40, and 41.]

[99] G. D. Barr, *et al.*, *Three-dimensional calculation of atmospheric neutrinos*, *Phys. Rev. D* **70** (Jul, 2004) 023006. [Cited page: 22.]

[100] G. Battistoni, A. Ferrari, T. Montaruli, and P.R. Sala, *The FLUKA atmospheric neutrino flux calculation*, *Astroparticle Physics* **19** (2003) 269 – 290. [Cited page: 22.]

[101] INO, A. Kumar *et al.*, *Invited review: Physics potential of the ICAL detector at the India-based Neutrino Observatory (INO)*, *Pramana* **88** (2017) 79. [Cited pages: 23, 29, 30, 32, 33, 34, 38, 39, 75, 80, 95, 96, 105, 106, and 107.]

[102] C.V. Achar *et al.*, *Detection of muons produced by cosmic ray neutrinos deep underground*, *Physics Letters* **18** (1965) 196 – 199. [Cited page: 24.]

[103] F. Reines *et al.*, *Evidence for High-Energy Cosmic-Ray Neutrino Interactions*, *Phys. Rev. Lett.* **15** (Aug, 1965) 429–433. [Cited page: 24.]

[104] Kamiokande Collaboration, K.S. Hirata *et al.*, *Experimental study of the atmospheric neutrino flux*, *Physics Letters B* **205** (1988) 416 – 420. [Cited page: 24.]

[105] Kamiokande Collaboration, K.S. Hirata *et al.*, *Observation of a small atmospheric ν_μ/ν_e ratio in Kamiokande*, *Physics Letters B* **280** (1992) 146 – 152. [Cited page: 24.]

[106] Kamiokande Collaboration, Y. Fukuda *et al.*, *Atmospheric ν_μ/ν_e ratio in the multi-GeV energy range*, *Physics Letters B* **335** (1994) 237 – 245. [Cited page: 24.]

[107] M. Aglietta *et al.*, *Experimental Study of Atmospheric Neutrino Flux in the NUSEX Experiment*, *EPL (Europhysics Letters)* **8** (1989) 611. [Cited page: 24.]

[108] K. Daum *et al.*, *Determination of the atmospheric neutrino spectra with the Fréjus detector*, *Zeitschrift für Physik C Particles and Fields* **66** (Sep, 1995) 417–428. [Cited page: 24.]

[109] D. Casper *et al.*, *Measurement of atmospheric neutrino composition with the IMB-3 detector*, *Phys. Rev. Lett.* **66** (May, 1991) 2561–2564. [Cited page: 24.]

[110] R. Becker-Szendy *et al.*, *Electron and muon-neutrino content of the atmospheric flux*, *Phys. Rev. D* **46** (Nov, 1992) 3720–3724. [Cited page: 24.]

[111] Super-Kamiokande Collaboration, Y. Fukuda *et al.*, *Evidence for Oscillation of Atmospheric Neutrinos*, *Phys. Rev. Lett.* **81** (Aug, 1998) 1562–1567. [Cited page: 24.]

[112] W.W.M. Allison *et al.*, *Measurement of the atmospheric neutrino flavour composition in Soudan 2*, *Physics Letters B* **391** (1997) 491 – 500. [Cited page: 24.]

[113] M Ambrosio *et al.*, *Measurement of the atmospheric neutrino-induced upgoing muon flux using MACRO*, *Physics Letters B* **434** (1998) 451 – 457. [Cited page: 24.]

[114] M. Ageron *et al.*, *ANTARES: The first undersea neutrino telescope*, *Nuclear Instruments and Methods in Physics Research Section A: Accelerators, Spectrometers, Detectors and Associated Equipment* **656** (2011) 11 – 38. [Cited page: 24.]

[115] R. Abbasi *et al.*, *The design and performance of IceCube DeepCore*, *Astroparticle Physics* **35** (2012) 615 – 624. [Cited page: 24.]

[116] H. Kwon *et al.*, *Search for neutrino oscillations at a fission reactor*, *Phys. Rev. D* **24** (Sep, 1981) 1097–1111. [Cited page: 25.]

[117] B. Achkar *et al.*, *Search for neutrino oscillations at 15, 40 and 95 meters from a nuclear power reactor at Bugey*, *Nuclear Physics B* **434** (1995) 503 – 532. [Cited pages: 25 and 26.]

[118] Z. D. Greenwood *et al.*, *Results of a two-position reactor neutrino-oscillation experiment*, *Phys. Rev. D* **53** (Jun, 1996) 6054–6064. [Cited page: 25.]

[119] M Apollonio *et al.*, *Initial results from the CHOOZ long baseline reactor neutrino oscillation experiment*, *Physics Letters B* **420** (1998) 397 – 404. [Cited page: 25.]

[120] M. Apollonio *et al.*, *Search for neutrino oscillations on a long base-line at the CHOOZ nuclear power station*, *The European Physical Journal C - Particles and Fields* **27** (Apr, 2003) 331–374. [Cited page: 25.]

[121] F. Boehm *et al.*, *Search for Neutrino Oscillations at the Palo Verde Nuclear Reactors*, *Phys. Rev. Lett.* **84** (Apr, 2000) 3764–3767. [Cited page: 25.]

[122] F. Boehm *et al.*, *Results from the Palo Verde neutrino oscillation experiment*, *Phys. Rev. D* **62** (Sep, 2000) 072002. [Cited page: 25.]

[123] KamLAND Collaboration, Michal Patrick and Decowski, *Measurement of anti-neutrino spectral distortion by KamLAND*, *International Journal of Modern Physics A* **20** (2005) 3051–3054. [Cited page: 25.]

[124] KamLAND Collaboration, A. Gando *et al.*, *Constraints on θ_{13} from a three-flavor oscillation analysis of reactor antineutrinos at KamLAND*, *Phys. Rev. D* **83** (Mar, 2011) 052002. [Cited page: 25.]

[125] MINOS Collaboration, P. Adamson *et al.*, *Search for Sterile Neutrinos Mixing with Muon Neutrinos in MINOS*, *Phys. Rev. Lett.* **117** (Oct, 2016) 151803. [Cited page: 26.]

[126] Daya Bay Collaboration, F. P. An *et al.*, *Improved Search for a Light Sterile Neutrino with the Full Configuration of the Daya Bay Experiment*, *Phys. Rev. Lett.* **117** (Oct, 2016) 151802. [Cited page: 26.]

[127] MINOS Collaboration, D. G. Michael *et al.*, *Observation of Muon Neutrino Disappearance with the MINOS Detectors in the NuMI Neutrino Beam*, *Phys. Rev. Lett.* **97** (Nov, 2006) 191801. [Cited page: 27.]

[128] MINOS Collaboration, P. Adamson *et al.*, *Measurement of the Neutrino Mass Splitting and Flavor Mixing by MINOS*, *Phys. Rev. Lett.* **106** (May, 2011) 181801. [Cited page: 27.]

[129] MINOS Collaboration, P. Adamson *et al.*, *Electron Neutrino and Antineutrino Appearance in the Full MINOS Data Sample*, *Phys. Rev. Lett.* **110** (Apr, 2013) 171801. [Cited page: 27.]

[130] T2K Collaboration, K. Abe *et al.*, *Measurement of Neutrino Oscillation Parameters from Muon Neutrino Disappearance with an Off-Axis Beam*, *Phys. Rev. Lett.* **111** (Nov, 2013) 211803. [Cited page: 27.]

[131] T2K Collaboration, K. Abe *et al.*, *Observation of Electron Neutrino Appearance in a Muon Neutrino Beam*, *Phys. Rev. Lett.* **112** (Feb, 2014) 061802. [Cited page: 27.]

[132] NOvA Collaboration, P. Adamson *et al.*, *First measurement of muon-neutrino disappearance in NOvA*, *Phys. Rev. D* **93** (Mar, 2016) 051104. [Cited page: 27.]

[133] NOvA Collaboration, P. Adamson *et al.*, *First Measurement of Electron Neutrino Appearance in NOvA*, *Phys. Rev. Lett.* **116** (Apr, 2016) 151806. [Cited page: 27.]

[134] OPERA Collaboration, N. Agafonova *et al.*, *Observation of a first ν_τ candidate event in the OPERA experiment in the CNGS beam*, *Physics Letters B* **691** (2010) 138 – 145. [Cited page: 27.]

[135] OPERA Collaboration, N Agafonova *et al.*, *Search for $\nu_\mu \to \nu_\tau$ oscillation with the OPERA experiment in the CNGS beam*, *New Journal of Physics* **14** (2012) 033017. [Cited page: 27.]

[136] F. Capozzi, *et al.*, *Neutrino masses and mixings: Status of known and unknown 3ν parameters*, *Nuclear Physics B* **908** (2016) 218 – 234. [Cited page: 27.]

[137] Super-Kamiokande Collaboration, K. Abe *et al.*, *Atmospheric neutrino oscillation analysis with external constraints in Super-Kamiokande I-IV*, arXiv:1710.09126. [Cited page: 27.]

[138] T2K Collaboration, K. Abe *et al.*, *Combined Analysis of Neutrino and Antineutrino Oscillations at T2K*, *Phys. Rev. Lett.* **118** (Apr, 2017) 151801. [Cited page: 27.]

[139] MINOS Collaboration, P. Adamson *et al.*, *Combined Analysis of ν_μ Disappearance and $\nu_\mu \to \nu_e$ Appearance in MINOS Using Accelerator and Atmospheric Neutrinos*, *Phys. Rev. Lett.* **112** (May, 2014) 191801. [Cited page: 27.]

[140] NOvA Collaboration, P. Adamson *et al.*, *Measurement of the Neutrino Mixing Angle θ_{23} in NOvA*, *Phys. Rev. Lett.* **118** (Apr, 2017) 151802. [Cited page: 27.]

[141] Ivan Esteban, *et al.*, *Global analysis of three-flavour neutrino oscillations: synergies and tensions in the determination of θ_{23}, $\delta_{\rm CP}$, and the mass ordering*, *Journal of High Energy Physics* **2019** (Jan, 2019) 106. [Cited pages: 27 and 28.]

[142] DUNE Collaboration, R. Acciarri *et al.*, *Long-Baseline Neutrino Facility (LBNF) and Deep Underground Neutrino Experiment (DUNE)*, arXiv:1601.05471. [Cited page: 29.]

[143] Hyper-K Collaboration, K. Abe *et al.*, *Letter of Intent: The Hyper-Kamiokande Experiment — Detector Design and Physics Potential —*, arXiv:1109.3262. [Cited page: 29.]

[144] IceCube PINGU Collaboration, M. G. Aartsen *et al.*, *Letter of Intent: The Precision IceCube Next Generation Upgrade (PINGU)*, arXiv:1401.2046. [Cited page: 29.]

[145] KM3NeT Collaboration, Ulrich F. Katz, *The ORCA Option for KM3NeT*, in *Proceedings of the 15th International Workshop on Neutrino Telescopes (Neutel 2013): Venice, March 11-15, 2013*, 2014. arXiv:1402.1022. [Cited page: 29.]

[146] INO, M. Sajjad Athar *et al.*, *India-based Neutrino Observatory: Project Report. Volume I.*, http://www.ino.tifr.res.in/ino/OpenReports/INOReport.pdf, 2006. [Cited pages: 30 and 31.]

[147] Naba K. Mondal, *India-based Neutrino Observatory*, *Pramana* **79** (Nov, 2012) 1003–1020. [Cited pages: 30 and 31.]

[148] V.M. Datar *et al.*, *Development of glass resistive plate chambers for INO experiment*, *Nuclear Instruments and Methods in Physics Research Section A: Accelerators, Spectrometers, Detectors and Associated Equipment* **602** (2009) 744 – 748. [Cited pages: 32 and 36.]

[149] S. P. Behera, M. S. Bhatia, V. M. Datar, and A. K. Mohanty, *Simulation Studies for Electromagnetic Design of INO ICAL Magnet and Its Response to Muons*, *IEEE Transactions on Magnetics* **51** (Feb, 2015) 1–9. [Cited pages: 33 and 34.]

[150] Kolahal Bhattacharya, Arnab K. Pal, Gobinda Majumder, and Naba K. Mondal, *Error propagation of the track model and track fitting strategy for the Iron CALorimeter detector in India-based neutrino observatory*, *Computer Physics Communications* **185** (2014) 3259 – 3268. [Cited pages: 33 and 47.]

[151] Anita Behere *et al.*, *INO prototype detector and data acquisition system*, *Nuclear Instruments and Methods in Physics Research Section A: Accelerators, Spectrometers, Detectors and Associated Equipment* **602** (2009) 784 – 787. [Cited page: 34.]

[152] R. Santonico and R. Cardarelli, *Development of resistive plate counters*, *Nuclear Instruments and Methods in Physics Research* **187** (1981) 377 – 380. [Cited page: 34.]

[153] Jingbo Wang *et al.*, *Development of high-rate MRPCs for high resolution time-of-flight systems*, *Nuclear Instruments and Methods in Physics Research Section A: Accelerators, Spectrometers, Detectors and Associated Equipment* **713** (2013) 40 – 51. [Cited page: 34.]

[154] Satyanarayana Bheesette, *Design and Characterisation Studies of Resistive Plate Chambers*. PhD thesis, Indian Inst. Tech., Mumbai, 2009. [Cited pages: 35, 36, and 37.]

[155] W. R. Leo, *Techniques for Nuclear and Particle Physics Experiments: A How to Approach*. Berlin, Germany: Springer (1987) 368 p, 1987. [Cited pages: 35 and 36.]

[156] P Camarri, R Cardarelli, A.Di Ciaccio, and R Santonico, *Streamer suppression with SF6 in RPCs operated in avalanche mode*, *Nuclear Instruments and Methods in Physics Research Section A: Accelerators, Spectrometers, Detectors and Associated Equipment* **414** (1998) 317 – 324. [Cited page: 36.]

[157] M. Bhuyan *et al.*, *VME-based data acquisition system for the India-based Neutrino Observatory prototype detector*, *Nuclear Instruments and Methods in Physics Research Section A: Accelerators, Spectrometers, Detectors and Associated Equipment* **661** (2012) S73 – S76. [Cited page: 38.]

[158] S. Dasgupta, *et al.*, *Development of trigger scheme for the ICAL detector of India-based Neutrino Observatory*, *Nuclear Instruments and Methods in Physics Research Section A: Accelerators, Spectrometers, Detectors and Associated Equipment* **678** (2012) 105 – 113. [Cited page: 38.]

[159] Mattias Blennow and Thomas Schwetz, *Identifying the neutrino mass ordering with INO and NOvA*, *Journal of High Energy Physics* **2012** (Aug, 2012) 58. [Cited page: 38.]

[160] Jaydip Singh, Srishti Nagu, and Jyotsna Singh, *Analysis of Ultra-High-Energy Muons at INO-ICAL Using Pair-Meter Technique*, in *Advanced Detectors for Nuclear, High Energy and Astroparticle Physics* (Saikat Biswas, Supriya Das, and Sanjay Kumar Ghosh, eds.), (Singapore), pp. 137–145, Springer Singapore, 2018. [Cited pages: 38 and 39.]

[161] Animesh Chatterjee, Raj Gandhi, and Jyotsna Singh, *Probing Lorentz and CPT violation in a magnetized iron detector using atmospheric neutrinos*, *Journal of High Energy Physics* **2014** (Jun, 2014) 45. [Cited pages: 38 and 39.]

[162] Sandhya Choubey, *et al.*, *Sensitivity to neutrino decay with atmospheric neutrinos at the INO-ICAL detector*, *Phys. Rev. D* **97** (Feb, 2018) 033005. [Cited page: 39.]

[163] Sandhya Choubey, Anushree Ghosh, Tommy Ohlsson, and Deepak Tiwari, *Neutrino physics with non-standard interactions at INO*, *Journal of High Energy Physics* **2015** (Dec, 2015) 1–22. [Cited page: 39.]

[164] N. DASH, V. M. DATAR, and G. MAJUMDER, *Sensitivity for detection of decay of dark matter particle using ICAL at INO*, *Pramana* **86** (Apr, 2016) 927–937. [Cited page: 39.]

[165] D. Casper, *The nuance neutrino physics simulation, and the future*, *Nuclear Physics B - Proceedings Supplements* **112** (2002) 161 – 170. [Cited pages: 40, 99, and 104.]

[166] S. Agostinelli *et al.*, *GEANT4 - a simulation toolkit*, *Nucl. Instrum. Methods A* **506** (2003) 250 – 303. [Cited pages: 40, 42, 43, 100, and 104.]

[167] Kolahal Bhattacharya, *Event Reconstruction for ICAL Detector and Neutrino Mass Hierarchy Sensitivity Analysis at India-based Neutrino Observatory (INO)*. PhD thesis, Tata Institute of Fundamental Research, Mumbai, 2015. [Cited pages: 44, 45, and 48.]

[168] John Stuart Marshall, *A study of muon neutrino disappearance with the MINOS detectors and the NuMI neutrino beam*. PhD thesis, Cambridge U., 2008. 10.2172/935002. [Cited page: 45.]

[169] R. Fruhwirth, *Application of Kalman filtering to track and vertex fitting*, *Nucl. Instrum. Meth.* **A262** (1987) 444–450. [Cited page: 47.]

[170] M M Devi, *et al.*, *Hadron energy response of the Iron Calorimeter detector at the India-based Neutrino Observatory*, *Journal of Instrumentation* **8** (2013) P11003. [Cited pages: 50 and 99.]

[171] R. Kanishka, *et al.*, *Simulations Study of Muon Response in the Peripheral Regions of the Iron Calorimeter Detector at the India-based Neutrino Observatory*, *JINST* **10** (2015) P03011, arXiv:1503.03369. [Cited pages: 55, 58, and 105.]

[172] A Chatterjee, *et al.*, *A simulations study of the muon response of the Iron Calorimeter detector at the India-based Neutrino Observatory*, *Journal of Instrumentation* **9** (2014) P07001. [Cited page: 58.]

[173] Tarak Thakore, Anushree Ghosh, Sandhya Choubey, and Amol Dighe, *The reach of INO for atmospheric neutrino oscillation parameters*, *Journal of High Energy Physics* **2013** (2013) 58. [Cited pages: 69, 70, 77, 79, 97, 105, and 106.]

[174] Lakshmi S. Mohan and D. Indumathi, *Pinning down neutrino oscillation parameters in the 2–3 sector with a magnetised atmospheric neutrino detector: a new study*, *The European Physical Journal C* **77** (Jan, 2017) 54. [Cited pages: 70, 77, 95, 96, and 97.]

[175] Moon Moon Devi, Tarak Thakore, Sanjib Kumar Agarwalla, and Amol Dighe, *Enhancing sensitivity to neutrino parameters at INO combining muon and hadron information*, *Journal of High Energy Physics* **2014** (2014) 189. [Cited pages: 70, 99, 105, and 106.]

[176] G. PrÃľzeau, *Dense Dark Matter Hairs Spreading Out from Earth, Jupiter, and Other Compact Bodies*, *The Astrophysical Journal* **814** (2015) 122. [Cited page: 72.]

[177] Walter Winter, *Atmospheric neutrino oscillations for Earth tomography*, *Nuclear Physics B* **908** (2016) 250 – 267. [Cited page: 72.]

[178] Walter Winter, *Probing the absolute density of the Earth's core using a vertical neutrino beam*, *Phys. Rev. D* **72** (Aug, 2005) 037302. [Cited page: 72.]

[179] KM3NeT, Simon Bourret, JoÃčo A B Coelho, VÃľronique Van Elewyck, and KM3NeT collaboration, *Neutrino oscillation tomography of the Earth with KM3NeT-ORCA*, *Journal of Physics: Conference Series* **888** (2017) 012114. [Cited page: 72.]

[180] Particle Data Group, K. A. Olive *et al.*, *Review of Particle Physics*, *Chin. Phys.* **C38** (2014) 090001. [Cited page: 73.]

[181] G. L. Fogli, *et al.*, *Getting the most from the statistical analysis of solar neutrino oscillations*, *Phys. Rev. D* **66** (Sep, 2002) 053010. [Cited page: 79.]

[182] M. C. Gonzalez-Garcia and Michele Maltoni, *Atmospheric neutrino oscillations and new physics*, *Phys. Rev. D* **70** (Aug, 2004) 033010. [Cited pages: 79, 80, and 81.]

[183] Ishitsuka Masaki, *L/E analysis of the atmospheric neutrino data from Super-Kamiokande*. PhD thesis, 2004. [Cited pages: 80 and 81.]

[184] Kameda Jun, *Detailed studies of neutrino oscillations with atmospheric neutrinos of wide energy range from* 100 MeV *to* 1000 GeV *in Super-Kamiokande*. PhD thesis, 2002. [Cited pages: 80 and 81.]

LIST OF PAPERS BASED ON THESIS

---

1. Study of neutrino oscillation parameters at the INO-ICAL detector using event-by-event reconstruction
   K. R. Rebin, J. Libby, D. Indumathi, S. M. Lakshmi
   The European Physical Journal C., **79**, 295 (2019)

2. Effect of event-by-event reconstruction and low event statistics on neutrino oscillation parameters at INO-ICAL detector
   K. R. Rebin, J. Libby, D. Indumathi
   [Manuscript to be submitted for a proceeding of XXIII DAE-BRNS High Energy Physics Symposium 2018.]

CONFERENCES/SCHOOLS ATTENDED

1. Presented a talk on *Study of neutrino oscillation parameters at the INO-ICAL detector using event-by-event reconstruction* at the **DAE-BRNS Symposium on High Energy Physics** (December 10 - 14, 2018), held at IIT Madras, Chennai.

2. Presented a poster titled *Study of neutrino oscillation parameters at the INO-ICAL detector using event-by-event reconstruction* at the **National Symposium on Particles, Detectors and Instrumentation**, TIFR, Mumbai, India, October 2017.

3. Presented a poster titled *Study of neutrino oscillation parameters at the INO-ICAL detector* at the **Third Asia-Europe-Pacific School of High-Energy Physics**, Beijing, China, October 2016.

4. Participated in the **National Symposium on Particles, Detectors and Instrumentation**, IICHEP, Madurai, India, March 2015.

5. Participated in the **IXth SERC School on Experimental High Energy Physics** at IIT Madras during December 2-21 (2013).

6. Participated in **SERC Preparatory School in Theoretical High Energy Physics**, Tezpur University, Assam, India, 2013